EPFL

Numerical Study of the Attosecond Free-Electron Laser Pulse Generation in the Soft X-ray Regime at the SwissFEL

Longdi ZHU

École
polytechnique
fédérale
de Lausanne

2024

Abstract

Isolated attosecond (10^{-18} s) pulses from an X-ray free-electron laser are in high demand for attosecond science, which enables the probing of electron dynamics by X-ray nonlinear spectroscopy and single-particle imaging.

The aim of this thesis is to simulate attosecond pulse trains at the Athos beamline of the SwissFEL facility. The research project investigates the possibility of generating the shortest pulse duration by incorporating several advanced configurations at Athos, namely the modular undulator, the magnetic chicane after each module, and the transverse gradient undulator configuration. The simulation results confirm the effectiveness of these configurations in reducing the pulse duration. For a radiation wavelength of 1 nm (1240 eV), the slicing method, which is basically an energy chirp-based taper on a modular undulator, is able to produce a pulse train with an average duration of 200 attoseconds. The mode-locking method, realised by delay control through magnetic chicanes after each module, further reduced the average pulse duration to less than 100 attoseconds, exceeding the cooperation length limit. In addition, we explored the possibility of applying a linear taper within the module by incorporating a rotated transverse gradient undulator for each module. For the 1 nm radiation wavelength, a slight linear taper within the undulator module can reduce the pulse duration to 85 attoseconds. For the 4 nm (310 eV) wavelength, the slippage effect is so strong that the pulse duration first decreases and then increases within the undulator module. To solve this problem, we have proposed using a strong undulator taper within the module. A 16 % difference taper range combined with the mode-locking method can generate a pulse train with an average duration of 110 attoseconds to the end of the module. It is important to note that the results presented in this work are primarily used to demonstrate the method's validity. Experimental results in the SwissFEL machine can differ significantly from the simulation due to many other effects.

In addition to the simulation and presentation of simulation results, the thesis has briefly included the FEL theory and used the theory to analyse the simulation results, which makes the result more understanable and plausible. During the discussion of the slicing method, we presented the bunching evolution in the slicing method and suggested that the superradiance dynamics can be used to explain many simulation results in this chapter. In the chapter with TGU, we suggest that the reason for generating such short pulses is mainly because the large taper provides a large spectrum, which is beneficial for generating short pulses when doing

mode-locking.

Résumé

Les impulsions attosecondes isolées (10^{-18} s) d'un laser à rayons X à électrons libres sont très demandées pour la science attoseconde, qui permet de sonder la dynamique des électrons par spectroscopie non linéaire à rayons X et l'imagerie de particules uniques.

L'objectif de cette thèse est de simuler des trains d'impulsions attosecondes sur la ligne de faisceau Athos du SwissFEL. Le projet de recherche étudie la possibilité de générer la durée d'impulsion la plus courte en incorporant plusieurs configurations avancées à Athos, à savoir l'onduleur modulaire, la chicane magnétique après chaque module, et la configuration de l'onduleur à gradient transverse. Les résultats de la simulation confirment l'efficacité de ces configurations pour réduire la durée de l'impulsion. Pour une longueur d'onde de rayonnement de 1 nm (1240 eV), la méthode de découpage en tranches, qui est essentiellement un cône basé sur un chirp d'énergie sur un onduleur modulaire, est capable de produire un train d'impulsions d'une durée moyenne de 200 attosecondes. La méthode de verrouillage de mode, réalisée par le contrôle du délai au moyen de chicanes magnétiques après chaque module, a encore réduit la durée moyenne de l'impulsion à moins de 100 attosecondes, dépassant ainsi la limite de la longueur de coopération. En outre, nous avons exploré la possibilité d'appliquer une conicité linéaire à l'intérieur du module en incorporant un onduleur à gradient transversal tourné pour chaque module. Pour la longueur d'onde de rayonnement de 1 nm, une légère conicité linéaire à l'intérieur du module onduleur peut réduire la durée de l'impulsion à 85 attosecondes.Pour la longueur d'onde de 4 nm (310 eV), l'effet de glissement est si important que la durée de l'impulsion diminue d'abord, puis augmente dans le module d'ondulation. Pour résoudre ce problème, nous avons proposé d'utiliser une forte conicité ondulatoire dans le module. Une différence de conicité de 16 % combinée à la méthode de verrouillage de mode peut générer un train d'impulsions d'une durée moyenne de 110 attosecondes jusqu'à l'extrémité du module. Il est important de noter que les résultats présentés dans ce travail sont principalement utilisés pour démontrer la validité de la méthode. Les résultats expérimentaux dans la machine SwissFEL peuvent différer de manière significative de la simulation en raison de nombreux autres effets.

En plus de la simulation et de la présentation des résultats de la simulation, la thèse a brièvement inclus la théorie FEL et a utilisé la théorie pour analyser les résultats de la simulation, ce qui rend les résultats plus compréhensibles et plus plausibles. Au cours de la discussion sur

la méthode de découpage en tranches, nous avons présenté l'évolution des paquets dans la méthode de découpage en tranches et suggéré que la dynamique de la superradiance peut être utilisée pour expliquer de nombreux résultats de simulation dans ce chapitre. Dans le chapitre sur le TGU, nous suggérons que la raison pour laquelle des impulsions aussi courtes sont générées est principalement due au fait que la grande conicité fournit un large spectre, ce qui est bénéfique pour générer des impulsions courtes lors d'un verrouillage de mode.

Mots clefs : Laser à électrons libres, train d'impulsions attoseconde, simulation, SwissFEL, SASE, ESASE, découpage, verrouillage de mode, onduleur à gradient transverse, effet de glissement, superradiance, conicité de l'onduleur.

Contents

List of Figures

List of Tables

1 Introduction

This is a simulation-based [1] PhD thesis investigating the generation of attoseconds (1 as = 10^{-18} s) free-electron laser pulses in train form at the SwissFEL facility [2, 3]. By combining existing configurations of the Athos beamline [4, 5], the research project explores the possibility of producing the shortest possible pulses in the soft X-ray regime, and demonstrates these improvements with simulation results.

A free-electron laser is a type of light source that can produce radiation over a wide range of frequencies, from microwaves to X-rays. It was first invented by John Madey [6] and experimentally demonstrated by his group in the 1970s [7]. Different from the conventional lasers, which use bound electrons in atoms or molecules to produce light by stimulated emission from excited electronic states, an FEL uses a beam of relativistic electrons, which are 'free' in that they are not bound in any atoms or molecules. Electromagnetic energy can be extracted from the kinetic energy of a relativistic electron beam to produce radiation [8, 9, 10, 11, 12, 13]. The advantage of such a light source is that it can produce wavelength-tunable, coherent and high-intensity radiation. A typical high-gain FEL operating in self-amplified spontaneous emission (SASE) mode [14] is capable of emitting coherent, multi-gigawatt, femtosecond-long [15, 16] X-ray pulses over a wavelength range in the X-ray spectrum from several nm down to 0.1 nm or even shorter [17].

Recently, high-intensity attosecond X-ray free-electron lasers have attracted increasing attention to meet the needs of attosecond science for studying the quantum mechanical motion of electrons in molecules and solids on the sub-femtosecond timescale [18, 19, 20, 21]. Also, several experimental results of generating attosecond pulse train have been reported from the SLAC laboratory [22, 23].

Building on the general concept of generating a sub-femtosecond pulse train on a FEL facility, the thesis extends the method by employing advanced configurations of the Athos beamline, presents a simulation-based study and shows the possibility of generating even shorter pulses.

The structure of the thesis

Starting with the basic theory of FEL in Chapter 2, the thesis provides a brief introduction to the basic concepts of FEL, from undulator radiation, low-gain FEL, and high-gain FEL to the concept of SASE. In addition, several important parameters are introduced, which are widely used for simulation evaluation.

In Chapter 3, the thesis provides a brief introduction to the SwissFEL machine, showing the layout of the machine and some photographs to give the reader a direct impression of the scientific facility. We use the Athos beamline as the basis for our simulations and report in this chapter, particularly on the important components related to advanced configurations, which will be discussed in the following chapters.

Beginning in Chapter 4, we present the results of the simulations. First, we show the basic functional mode of the FEL operation, the SASE. We show SASE simulations at 1 nm and 4 nm radiation wavelengths. Due to the nature of SASE radiation, the pulse position distribution is random and the pulse intensity follows a gamma distribution.

In considering the generation of attosecond pulses, we first considered enhanced SASE (ESASE) as a candidate method to generate attosecond pulses. We have obtained a pulse train of typical 500 attoseconds for $\lambda_r = 1$ nm. However, the ESASE mode alone is not sufficient to overcome the strong slippage effect [24] at a radiation wavelength of 4 nm.

Subsequently, three unique configurations in the Athos beamline are studied, that will contribute to the generation of short pulses. They are

- Chapter 5: The energy chirp-based undulator taper on a modular undulator.

- Chapter 6: The precise delay control through magnetic chicanes.

- Chapter 7: The rotated transverse gradient undulator.

These novel configurations are connected with established operating methods recognised by the FEL community, such as

- Chapter 5: The slicing method.

- Chapter 6: The mode-locking method.

- Chapter 7: The use of a strong reverse taper.

Achievements

We utilise an idealized beam for simulation to reduce the impact of electron beam parameter jitters and enhance our understanding of the dynamics. The simulation intentionally uses parameters, like energy spread and current, that are less optimal than the actual machine performance. This setup provides a conservative estimate of the simulation result compared to the experimental performance.

From the simulation results, the slicing method is able to achieve a well-separated and clean pulse with an average duration of only **200 attoseconds** and a peak power of tens of Gigawatt for 1 nm radiation wavelengths.

The mode-locking method is able to further shorten the average pulse duration to an average of less than **100 attoseconds**, which is beyond the cooperation length limit, with a peak power of around 1 Gigawatt.

The linear taper within the undulator module is able to further decrease the pulse duration, on top of the setting in mode-locking, we applied a narrow-range taper ($\sim 1\%$), and we have achieved pulses with **85 attosecond**.

At extended radiation wavelengths, such as 4 nm radiation wavelength, the simulation suggests a strong undulator taper, with the average pulse duration of the primary pulse only being **110 attoseconds**, with a peak power of tens of Gigawatt.

The simulation results we present are primarily to demonstrate the method's validity. It should be noted that the actual results from the machine may vary significantly due to other factors. Nevertheless, the results confirm that the above-mentioned configurations of the Athos undulator are beneficial for generating attosecond pulses at the SwissFEL.

In addition to employing numerical simulations to demonstrate the feasibility of generating ultrashort pulses, I have tried to incorporate theoretical knowledge of free-electron lasers into the analysis of many simulation results to make the results more understandable and plausible.

2 FEL Theory Basics

In this chapter, the basic theory of free electron lasers will be introduced. The main research of the thesis work is based on numerical simulations. A basic understanding of FEL theory is needed to configure simulation parameters and to interpret results. The discussion is limited to one-dimensional motion since three-dimensional effects like emittance [25] or diffraction [26] have little impact on the results of this thesis.

The chapter has been structured in a step-by-step manner to explain the increasing complexity of the theory. It consists of four sections:

- Undulator radiation, low gain FEL

- High gain FEL

- Collective variables, FEL instability

- Self-amplified spontaneous emission

In this initial segment, we deduce the electron dynamics in the undulator field by following the diagrammatic steps:
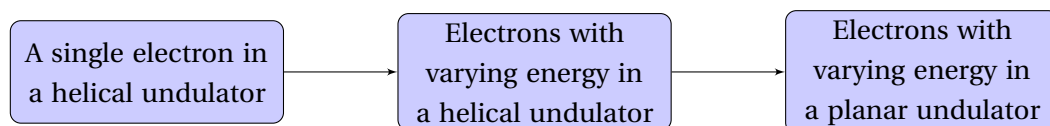
We consider both the phase and the energy changes in the electrons. Combining the evolution of both variables gives the FEL pendulum equation. With the FEL pendulum equation, we can derive the boundary conditions that determine whether the electrons participate in FEL resonance and plot these conditions in longitudinal phase space.

In the second section, we extend the model for high-gain FEL analysis. Compared to the first section, the constant field assumption is dropped. In addition, the undulator is longer, so the

radiation emitted by the electrons is considerably larger. Subsequently, the emitted radiation has a feedback effect on the phase change of the electrons, resulting in the formation of a micro-bunching structure in the beam, accompanied by an increase in the coherence of the radiation. The process is shown in the diagram below:
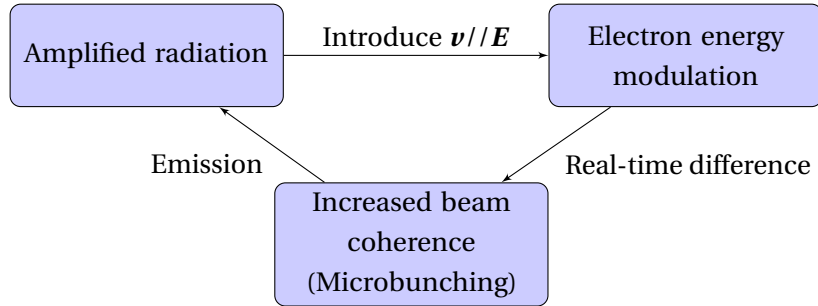
We then derive the equations in the high-gain FEL that include the electron density modulation. The derivation requires the assumption that the radiation is smoothly amplified, allowing us to drop the terms with higher-order derivatives. Under this assumption, we obtain a set of coupled first-order equations containing three subequations: one for the radiation field amplitude and phase, one for the electron phase, and one for the electron energy offset. This set of first-order equations can be transformed by rewriting the three first-order derivatives as a third-order derivative of a single term for the radiation field. This third-order derivative equation has an analytical solution, from which we obtain that the radiation field amplitude evolves exponentially along the undulator, which is the core result for high-gain FELs.

In the third section, we discuss the dynamics through several collective variables, such as the radiation field, the bunching and the energy modulation, there are two initial collective variables such as the detuning parameter and the energy spread. We use the Vlasov equation to model the system and the Laplace method to solve the linear equations. The results obtained are consistent with those obtained in the high-gain FEL. However, this approach enables us to evaluate the impact of a non-zero energy spread on the instability of the FEL, which is more practical for simulation analysis.
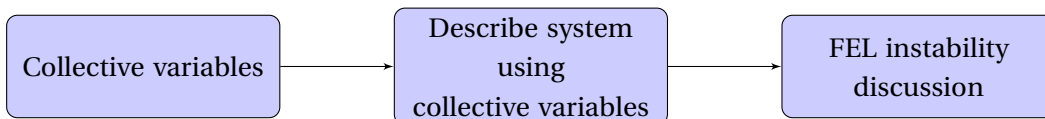
In the last section, we consider the statistical distribution of the individual electrons in the beam over space and time and its impact on the evolution of the FEL process. This leads us to discuss the properties of the radiation in the context of statistical considerations. We call the process of amplification of electron spontaneous emission to saturation self-amplified spontaneous emission (SASE). The discussion of SASE and its stochastic nature is the basis for the following chapters.

The chapter is concise, largely following the work of Schmuser [12] and Saldin [10], and [27] for the helical undulator part.

2.1   Electron's Motion and Energy Exchange

We start with the dynamics of electron motion in an undulator. The undulator is a periodic array of magnetic fields produced by permanent magnets with rotating polarities and constant field strength. This section discusses the case of a helical undulator with transverse magnetic field polarisation, shown in figure 2.1.
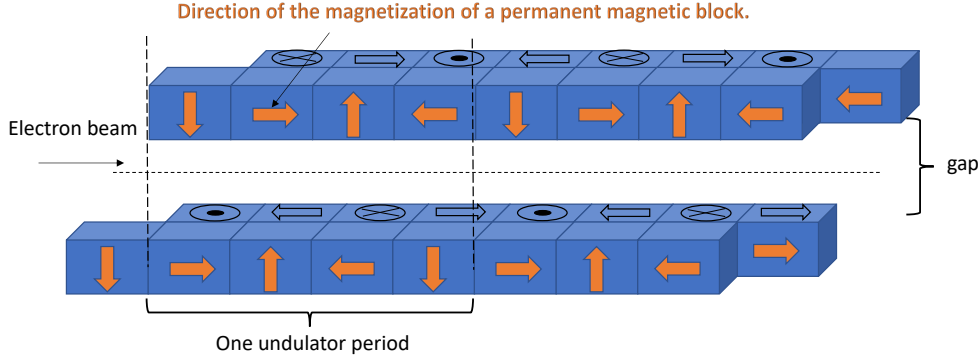
Figure 2.1: Schematic diagram of a helical undulator. Permanent magnet blocks are arranged in a sequence of four different orientations. The arrangement is designed to manipulate the circular polarity of the magnetic field. The resulting helical trajectory of these electrons is shown in detail in Figure 2.2.

2.1.1   Electron's Motion in a Helical Undulator

Consider a relativistic electron moving in a helical undulator within a Cartesian coordinate system $(\hat{x}, \hat{y}, \hat{z})$. The axis of the undulator is along the z-direction, which coincides with the primary direction of beam propagation. Since there are no sources in the gaps between the magnetic poles, the current density **j** is zero, e.g. **j** = 0. This leads to a constraint on the magnetic field:

$$\nabla \times \mathbf{B_u} = 0, \tag{2.1}$$

where B_u is the magnetic field of the undulator. On the axis, the magnetic field can be expressed as

$$\mathbf{B_u} = \mathbf{e_x} \cos(k_u z) + \mathbf{e_y} \sin(k_u z), \tag{2.2}$$

where $k_u = 2\pi/\lambda_u$ is the undulator wave number, λ_u is the undulator period length.

The Lorentz force on an electron in the presence of a magnetic field is

$$\frac{d\mathbf{p}}{dt} = \mathscr{F} = -e\mathbf{v} \times \mathbf{B_u}, \tag{2.3}$$
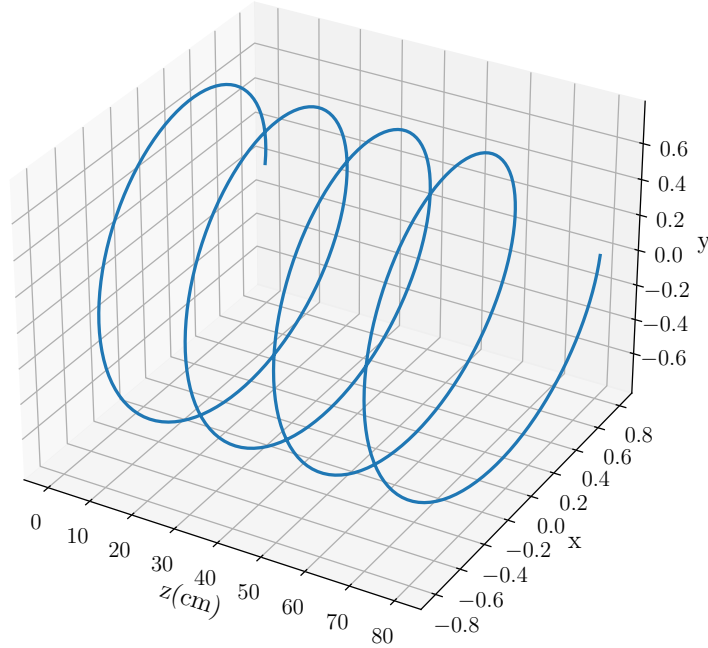
Figure 2.2: Three-dimensional representation of an electron trajectory in a helical undulator. The helix-shaped curve illustrates the path of an electron as it propagates through the undulator, with the z-axis representing the longitudinal direction (z) in centimeters, the x-axis corresponding to the normalised horizontal displacement (x), and the y-axis denoting the normalised vertical displacement (y).

where $|\mathbf{v}| = \sqrt{v_x{}^2 + v_y{}^2 + v_z{}^2}$ represents the length of the velocity vector. Considering electrons with charge $-e$ and mass m_e, the equations of motion for the electron in the x and y directions can be derived as follows

$$m_e\gamma\frac{dv_x}{dt} = ev_zB_y = -ev_zB_u\sin(k_uz), \quad m_e\gamma\frac{dv_y}{dt} = -ev_zB_x = -ev_zB_u\cos(k_uz), \quad (2.4)$$

where γ is the Lorentz factor. Here the condition that the total energy of the electron is conserved must be satisfied, since the electron is moving in a magnetic field.

In accelerator physics, it is common practice to replace the independent variable t by the path length z along the nominal beam path. This substitution simplifies the equations of motion. For relativistic particles, the approximation $dz = v_zdt \approx cdt$ holds, since $v_x, v_y \ll v_z \approx c$. By defining $\widetilde{B} = B_x + iB_y$ and $\widetilde{v} = v_x + iv_y$ as a complex quantity representing the transverse magnetic field components, the equations in 2.4 can be combined to give the following equation:

$$m_e\gamma\frac{d\widetilde{v}}{dz} = -iev_z\widetilde{B} = -iev_zB_u\exp(-ik_uz) \tag{2.5}$$

To further analyse the transverse relativistic velocity $\boldsymbol{\beta}_\perp$, we can integrate the left side of the equation 2.5, which leads to

$$\boldsymbol{\beta}_\perp = \frac{\tilde{v}}{c}\tilde{\boldsymbol{v}} = \frac{\lambda_u e v_z B_u}{2\pi m_e c}\frac{\exp(-ik_u z)}{\gamma}\tilde{\boldsymbol{v}} \tag{2.6}$$

The equation allows us to define the undulator parameter $K = \frac{\lambda_u e B_u}{2\pi m_e c}$. The typical value of K in an undulator for Athos is $K \approx 2.7$, for the European XFEL, it is $K \approx 10$.

The velocity of the electrons in the undulator field can also be expressed implicitly and then converted into an explicit expression:

$$\boldsymbol{\beta}_\perp = \frac{K}{\gamma}\exp(-ik_u z)\tilde{\boldsymbol{v}} = \frac{K}{\gamma}[\mathbf{e_x}\cos(k_u z) - \mathbf{e_y}\sin(k_u z)] \tag{2.7}$$

The result shows that the motion of the electron in the undulator follows a constrained helical trajectory parallel to the longitudinal coordinate z, with the maximum angle between the direction of electron motion and the forward direction $\theta = \frac{K}{\gamma}$. For highly relativistic electrons, it holds $\beta_\perp \approx \frac{K}{\gamma} \ll 1$.

Energy Exchange Between an Electron and the Co-Propagating Wave

We consider a circularly polarised electromagnetic field propagating parallel to an electron in the longitudinal direction in an undulator. The change in energy between the electron and the electromagnetic field is due to the transverse motion of the electron, and the rate of change is

$$m_e c^2 \frac{d\gamma}{dt} = -ec \cdot \boldsymbol{\beta}_\perp \cdot \boldsymbol{E}_\perp, \tag{2.8}$$

where

$$\boldsymbol{E}_\perp = \mathbf{e_x}E_0\cos(\omega(z/c - t)) - \mathbf{e_y}E_0\sin(\omega(z/c - t)) \tag{2.9}$$

is the electric field vector, ω is the angular frequency of the radiation. Substituting equations (2.7) and (2.9) into the right hand side of equation (2.8) we get

$$-ec \cdot \boldsymbol{\beta}_\perp \cdot \boldsymbol{E}_\perp = -ec\frac{K}{\gamma}[\mathbf{e_x}\cos(k_u z) - \mathbf{e_y}\sin(k_u z)]\cdot \tag{2.10}$$

$$[\mathbf{e_x}E_0\cos(\omega(z/c - t)) - \mathbf{e_y}E_0\sin(\omega(z/c - t))]$$

$$= \frac{-ecK}{\gamma}(E_0[\cos(k_u z)\cos(\omega(z/c - t)) - \sin(k_u z)\sin(\omega(z/c - t))])$$

$$= \frac{-ecK}{\gamma}E_0\cos[k_u z + \omega(z/c - t)] \tag{2.11}$$

To ensure effective energy transfer between the electron and the radiation, it is necessary to establish synchronisation between the electron motion and the radiation field. This synchro-

nisation is achieved when the scalar product $(-ec\boldsymbol{\beta}_\perp \cdot \boldsymbol{E}_\perp)$ remains nearly constant along the length of the undulator. The cosine function in equation 2.11 includes the ponderomotive phase:

$$\phi = k_u z + \omega(z/c - t) \tag{2.12}$$

The phase evolution is:

$$d\phi = k_u dz + \frac{\omega}{c} dz - \omega dt \tag{2.13}$$

From this, the phase evolution along the undulator can be derived as:

$$\frac{d\phi}{dz} = k_u + k - \omega \frac{1}{dz/dt} = k_u + k - k\frac{1}{\beta_\parallel}, \tag{2.14}$$

where $\beta_\parallel = \sqrt{\beta^2 - \beta_\perp^2} = \sqrt{1 - \frac{1}{\gamma^2} - \frac{K^2}{\gamma^2}} \simeq 1 - \frac{1+K^2}{2\gamma^2}$. Simplifying the expression, the ponderomotive phase evolution along the undulator is given by:

$$\frac{d\phi}{dz} = k_u - k\frac{1+K^2}{2\gamma^2} \tag{2.15}$$

To achieve a stationary state and optimize the energy transfer, it is necessary for the phase evolution equation, $d\phi/dz = 0$, to hold. By converting the wave vector to wavelength $k = 2\pi/\lambda$, the resonance condition can be expressed as:

$$\lambda = \frac{\lambda_u}{2\gamma^2}(1 + K^2), \tag{2.16}$$

where λ is the resonance wavelength. This equation shows that the resonance wavelength can be tuned continuously by adjusting the electron energy γ or the undulator parameter K. Changing these parameters allows the synchronisation between the electron motion and the radiation field to be modified.

2.1.2   Energy Offset Analysis for an Electron Beam in a Helical Undulator

Building on the discussion of a single electron in the undulator, we will now extend the discussion to multiple electrons. We will first consider the case of two electrons and then progress to a larger number, denoted by N. The energy of each electron is not identical but varies within a certain range.

So far we have concentrated on the analysis of a single electron in the undulator. This electron (0) is in resonance, so we refer to its energy as γ_0, which corresponds to the resonance energy, e.g. $\gamma_0 = \gamma_r$. Now let's consider the scenario where another electron(1) has an energy γ_1, which is not equal to γ_r, and the electron(1) is not fully in resonance. Both electrons experience the same magnetic field in the undulator.

We knew from the equation 2.15, for the electron with resonance energy γ_r :

$$\frac{d\phi_r}{dz} = k_u - k\frac{1+K^2}{2\gamma_r^2} = 0 \tag{2.17}$$

For an electron with energy γ, it holds:

$$\frac{d\phi}{dz} = k_u\left[1 - \frac{k(1+K^2)}{2k_u\gamma^2}\right] = k_u\left[1 - \frac{1}{\gamma^2}\frac{\lambda_u(1+K^2)}{2\lambda_r}\right] = k_u\left[1 - \frac{\gamma_r^2}{\gamma^2}\right] \tag{2.18}$$

In most cases, $|\gamma - \gamma_r| \ll \gamma_r$, resulting in:

$$\frac{d\phi}{dz} = k_u\left[1 - \frac{\gamma_r^2}{\gamma^2}\right] \simeq 2k_u\frac{\gamma - \gamma_r}{\gamma_r} \tag{2.19}$$

The equation shows that the rate of electron phase change in the undulator is proportional to the derivative of the electron energy from the resonance energy.

We are also interested in determining the energy loss of the electrons. To calculate this, we substitute $dz \approx cdt$ into equation (2.8) and evaluate the left side of the equation:

$$\frac{d\gamma}{dz} = \frac{d\gamma}{cdt} = -\frac{eK}{m_ec^2\gamma_r^2}E_0\cos\phi, \tag{2.20}$$

which describes the energy change of the electron along the undulator. The equation shows that the rate of change of the electron's energy depends on the resonance energy and the ponderomotive phase.

We summarise and combine the two previous equations as **FEL pendulum equations**.

$$\begin{cases} \dfrac{d\phi}{dz} = 2k_u\dfrac{\gamma - \gamma_r}{\gamma_r} \\[2mm] \dfrac{d\gamma}{dz} = -\dfrac{eK}{m_ec^2\gamma_r^2}E_0\cos\phi \end{cases} \tag{2.21}$$

The FEL pendulum equation describes how the energy deviation from the resonance energy affects the phase and energy evolution of the electron.

2.1.3 Phase Space Trajectory

We now consider a beam of electrons, where the energy of the electrons is a small fraction of the difference compared to the resonance energy. The mean value of the energy is γ_0, with a large number of electrons, denoted by N. A cold beam is assumed, which has no intrinsic energy spread.

The Hamiltonian is used for the resonance equation. The radiation amplitude E_0 of the electric field is assumed to be constant inside the undulator. We postpone taking into account the effect of changing field strength to the high gain FEL section.

When considering an electron in an ensemble of electrons, the energy of the jth electron γ_j can be different from the central energy γ_0. We take the central energy to be the resonance energy, i.e. $\gamma_0 = \gamma_r$. It is convenient to introduce the **energy offset** parameter of the electron $\eta_j = (\gamma_j - \gamma_r)/\gamma_r$ to measure the magnitude of the energy deviation. The equation (2.21) becomes

$$\begin{cases} \dfrac{d\phi_j}{dz} = 2k_u \eta_j \\ \dfrac{d\eta_j}{dz} = -\dfrac{eK}{m_e c^2 \gamma_r^2} E_0 \sin\phi_j, \end{cases} \tag{2.22}$$

with $\Omega = \sqrt{(2eKE_0)/(k_u m_e c^2 \gamma_0^2)}$. Replace ϕ with $\phi \to \phi + \frac{\pi}{2}$ to make the equation more manageable. The item with the dependence of $\frac{1}{\gamma_r^2}$ in the derivation of $d\eta_j/dz$ has been omitted.

Eliminating η_j by substituting eq.(2.22-1) into eq.(2.22-2), and the second order phase evolution over z gives

$$\frac{d^2\phi_j}{dz^2} + \Omega^2 \cos\phi_j = 0 \tag{2.23}$$

The form of equation (2.23) is the same as in a pendulum equation in classical mechanics. We take advantage of the conclusion of the pendulum problem and obtain the Hamiltonian of the co-propagating electron as

$$H_j(\phi_j, \eta_j) = k_u \eta_j^2 + \Omega^2 (1 - \cos\phi_j), \tag{2.24}$$

where $dH_j/d\phi_j = -d\eta_j/dz$, $dH_j/d\eta_j = d\phi_j/dz$. The trajectory for an electron of energy evolution in phase space (ϕ, η) is a curve of equal Hamiltonian. Those electrons with periodic oscillation and bounded are separated from the unbounded by a curve called *Separatrix*, the equation of the separatrix curve is

$$\eta_{sp}(\phi) = \pm\Omega \cos(\phi/2) \tag{2.25}$$

The curve passes through two fix-points: $(\phi = \pm\pi, \Delta = 0)$ and two extreme points of η : $(\phi = 0, \Delta = \pm 2\Omega)$. The range in between is called the "bucket". The electrons in the bucket lose or gain energy depending on their ponderomotive phase: Electrons of phases in $[0, \pi]$ lose energy during the resonance process. In contrast, those in $[-\pi, 0]$ are gaining energy.

Phase space trajectory in free electron laser
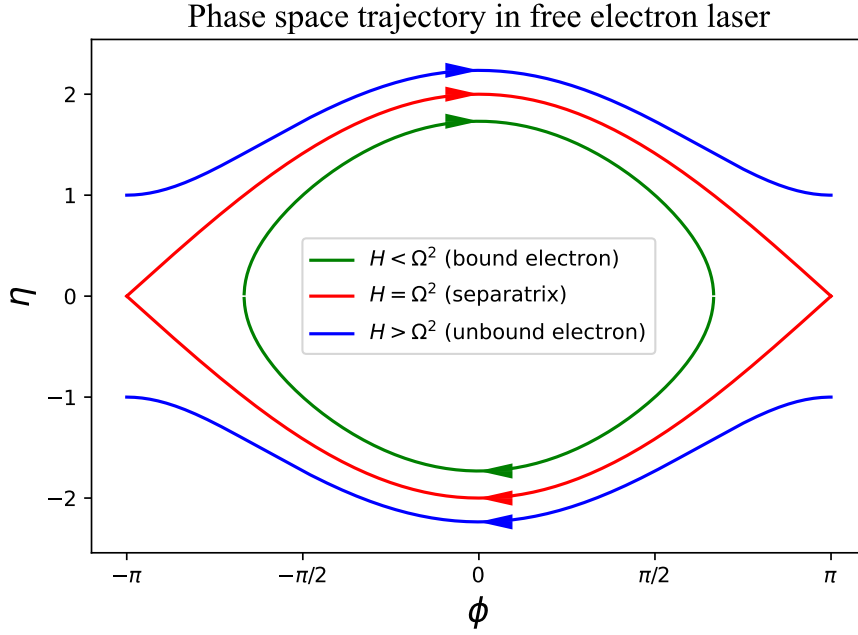
Figure 2.3: Phase space trajectories and separatrix curve in an FEL. The red line represents the separatrix (Hamiltonian $H = \Omega^2$), which delineates the boundary between bound and unbound electron trajectories. The green line depicts trajectories of bound electrons (Hamiltonian $H < \Omega^2$) confined within the separatrix. The blue line shows trajectories of unbound electrons (Hamiltonian $H > \Omega^2$), which exist outside the confines of the separatrix.

2.1.4 Dynamics in Planar Undulators

Helical undulators feature a helical configuration of magnetic poles, while planar undulators possess a flat arrangement of poles in one plane. Although they differ in design, both undulators utilize the core principle of alternating magnetic fields to produce coherent radiation. The system dynamics for planar undulators can be analyzed using a similar approach to helical undulators.

In a planar undulator, the undulator field only has one direction. Electrons oscillate in the x-direction of the transverse plane, and the momentum in the y-direction P_y is 0. The electric field is:

$$E_\perp = \mathbf{e_x} E_0 \cos(\omega(z/c - t)), \tag{2.26}$$

The longitudinal velocity of an electron is

$$\boldsymbol{\beta}_\perp = \frac{K}{\gamma} \boldsymbol{e_x} \cos(k_u z), \tag{2.27}$$
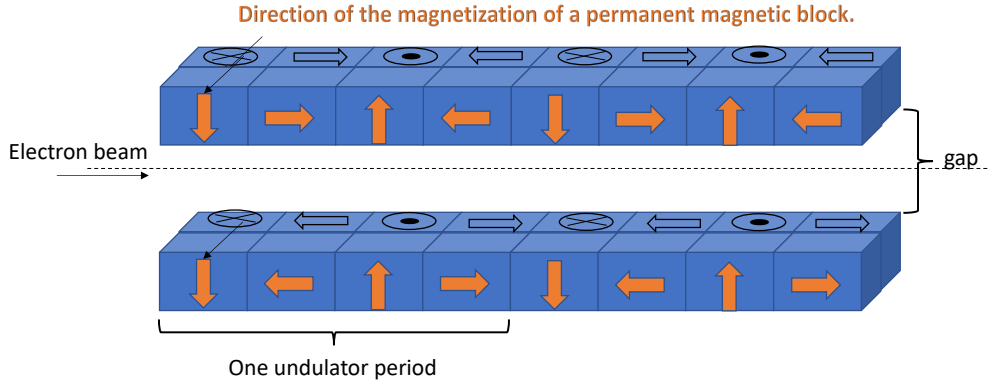
Figure 2.4: Schematic of a planar undulator. The planar undulator is characterized by a meticulously arranged sequence of oscillating magnets, each displaying two distinct polarities. These magnets create a straight-line polarized magnetic field across the device. The zig-zag path electrons take because of this field is shown in Figure 2.5.
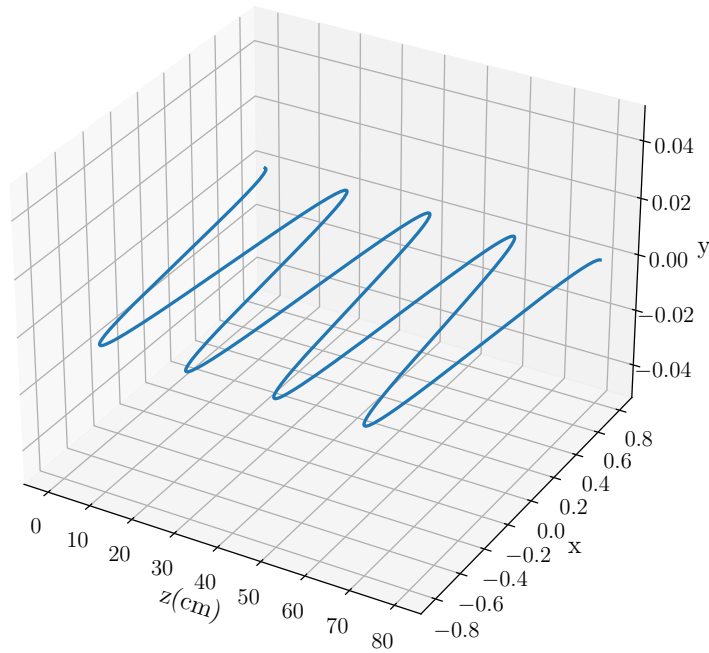
Figure 2.5: Three-dimensional representation of an electron trajectory in a planar undulator. The sinusoidal curve illustrates the path of an electron as it propagates through the undulator, with the z-axis representing the longitudinal direction (z) in centimeters, the x-axis corresponding to the horizontal displacement (x), and the y-axis denoting the vertical displacement (y).

The energy change between the field and electron over the undulator is

$$\frac{d\gamma}{dz} = \frac{-e}{m_e c^2} \boldsymbol{\beta}_\perp \cdot \boldsymbol{E}_\perp = \frac{-eK}{m_e c^2 \gamma} E_0 [\cos(k_u z) \cos(\omega(z/c - t))] \tag{2.28}$$

$$= \frac{-eK}{2m_e c^2 \gamma} E_0 [\cos(k_u z + kz - \omega t) + \cos(k_u z - kz + \omega t)]$$

The mean longitudinal velocity, denoted by $\phi_1 = \cos(k_u z + kz - \omega t)$, exhibits a resonance point when $k_u z + kz - \omega t = 0$. At this resonance, the phase condition aligns with that presented in equation (2.14), where

$$\beta_\parallel = \sqrt{\beta^2 - \beta_\perp^2} \simeq \sqrt{1 - \frac{1}{\gamma^2} - \frac{K^2}{\gamma^2} < \cos^2(k_u z) >} \tag{2.29}$$

$$= \sqrt{1 - \frac{1}{\gamma^2} - \frac{K^2}{2\gamma^2} < 1 - \sin(2k_u z) >}$$

$$= \sqrt{1 - \frac{1}{\gamma^2} - \frac{K^2}{2\gamma^2}} \simeq 1 - \frac{1 + K^2/2}{2\gamma^2}, \tag{2.30}$$

and then the resonance condition is

$$\lambda_r = \frac{\lambda_u}{2\gamma^2}(1 + \frac{K^2}{2}) \tag{2.31}$$

The planar undulator differs from the helical undulator in that the second item in equation (2.28), $\phi_2 = \cos(k_u z - kz + \omega t)$ can not be in complete resonance as

$$\frac{d\phi}{dz} = k_u + k(\frac{1 + K^2}{2\gamma^2}) > 0. \tag{2.32}$$

It is essential to account for the impact of energy evolution in the longitudinal direction, as it can not be neglected. As a result of the sinusoidal trajectory, the longitudinal component of the electron oscillation is not a fixed value but varies. From page 20 of [28], the energy evolution can be written as:

$$\frac{d\gamma}{dz} = \frac{-eK}{2m_e c^2 \gamma} E_0 [\cos(k_u z + kz - \chi \sin(2k_u z) - \omega t)$$

$$+ \cos(k_u z - kz - \chi \sin(2k_u z) - \omega t + \omega t)] \tag{2.33}$$

where, $\chi = \frac{(k + k_u)K^2}{k_u 8\gamma^2 \overline{\beta_z}} = \frac{1}{\beta_z^2} \frac{K^2}{4 + 2K^2} \simeq \frac{K^2}{4 + 2K^2}$. Equation 2.33 can be written as a series expansion [8]:

$$\frac{d\gamma}{dz} = \frac{-eKE_0}{2m_e c^2 \gamma} \cdot \sum_{m=-\infty}^{\infty} (-1)^m [J_m(\chi) - J_{m+1}(\chi)] \cdot \cos(\phi + 2mk_u z), \tag{2.34}$$

where $J_m(\chi)$ is the Bessel function of the first kind with m being an integer. The above result suggests that the effect of a longitudinal oscillation component produces higher-order harmonics in the radiation spectrum. To express the forward coupling in the equation, the coupling parameter $[JJ]$ is introduced, where

$$[JJ] = J_n\left(\frac{mK^2}{4 + 2K^2}\right) - J_{n+1}\left(\frac{mK^2}{4 + 2K^2}\right), \quad m = 2n + 1. \tag{2.35}$$

When $[JJ] = 1$, the instance becomes a helical undulator.

2.2   High-Gain FEL Model

In this section, we discuss the one-dimensional high-gain FEL theory. In the high-gain FEL, the undulator is rather long and the radiation amplitude is significantly amplified along the z-direction, an effect that can not be neglected. The discussion is based on planar undulators, but with $[JJ] = 1$ the case for helical undulators is obtained.

2.2.1   Electron Density Modulation

In the one-dimensional model, the radiation field with horizontal polarisation can be written as

$$\tilde{E}_x(z, t) = \tilde{E}_x(z)\exp(i(kz - \omega t)), \tag{2.36}$$

where the tilde over the field indicates the complex notation, and k, ω correspond to the radiation at the resonance frequency. To analyse how the electric radiation field affects electrons, we use the Maxwell's equation:

$$\left(\frac{\partial^2}{\partial z^2} - \frac{1}{c^2}\frac{\partial^2}{\partial t^2}\right)\tilde{E}_x(z, t) = -\mu_0\frac{\partial \tilde{j}_x}{\partial t}, \tag{2.37}$$

where ∇^2 is reduced to a single second-order partial derivative with respect to z due to the one-dimensional approximation, assuming that field variations in the transverse directions are negligible compared to the longitudinal direction. $\tilde{j}_x$ is the current density in the x-direction. The main contribution in equation 2.37 is the sinusoidal motion of the electron beam. Inserting the equation (2.36) into the equation (2.37), we obtain:

$$\left[2ik\frac{\partial \tilde{E}_x(z)}{\partial z} - \frac{\partial^2 \tilde{E}_x(z)}{\partial z^2}\right]\exp[i(kz - \omega t)] = \mu_0\frac{\partial \tilde{j}_x}{\partial t}, \tag{2.38}$$

where the time derivative is dropped using the steady-state approximation. Assuming smooth changes in radiation amplitude over z and small changes over a single radiation wavelength, the Slow Varying Envelope Approximation (SVEA) can be applied:

$$\left|\frac{\partial^2 \tilde{E}_x}{\partial z^2}\right| \ll \left|k\frac{\partial \tilde{E}_x}{\partial z}\right|, \quad \left|\frac{\partial \tilde{E}_x}{\partial z}\right| \ll \left|k\tilde{E}_x\right| \tag{2.39}$$

With SVEA, the second-order derivatives are neglected, and the first-order derivatives, although also small, highlight the gradual change in amplitude. This evolution of the amplitude can be summarised as follows

$$\frac{d\tilde{E}_x}{dz} = -\frac{i\mu_0}{2k}\frac{\partial \tilde{j}_x}{\partial t}\cdot\exp\left[-i(kz - \omega t)\right], \tag{2.40}$$

where the temporal variation in current density can be expressed as:

$$\left[\frac{\partial \tilde{j}_x}{\partial t}\right]_{z=const} = \frac{\partial \tilde{j}_z}{\partial t}\frac{K[JJ]}{\gamma_0}\cos(k_u z),$$

(2.41)

and the current density in the longitudinal direction $\tilde{j}_z$ can be written as

$$\tilde{j}_z = j_0 + \tilde{j}_1(z)\exp(-i(kz-\omega t)),$$

(2.42)

where the item with $\tilde{j}_1(z)$ represents the complex amplitude of a wave-like perturbation in the current density. The amplitude deviation in the transverse direction becomes

$$\frac{d\tilde{E}_x}{dz} \simeq -\frac{\mu_0 c K[JJ]}{4\gamma_0}\tilde{j}_1 \cdot (1+\exp(i2k_u z))$$

(2.43)

Finally, considering an average across an undulator period, the factor $\exp(i2k_u z)$ will be averaged to zero. Thus, there is

$$\frac{d\tilde{E}_x}{dz} = -\frac{\mu_0 c K[JJ]}{4\gamma_0}\tilde{j}_1$$

(2.44)

2.2.2 Micro Bunching

Micro-bunching occurs when radiation modulates the energy of electrons based on their position relative to the radiation wave. Electrons with higher energies will move forward, while those with lower energies fall backward. As electrons traverse the undulator, they accumulate at the nodes of the radiation wave where the energy change is zero. This results in the electron beam splitting into small bunches, separated by λ_r, as shown in 2.6. At these bunched positions, the radiation intensity is amplified due to the enhanced coherence of the emission. This process is cyclic and the radiation is constantly amplified, forming the core mechanism of the high gain FELs. In addition to coherent emission, there is also coherent absorption, which is more of a factor to be considered in the saturation regime.

Our main focus is on the amplitude of the electric field in the z-direction, which is derived from the one-dimensional model based on Maxwell's equation. The electric static field from a modulated charge density is given by $\nabla \cdot \boldsymbol{E} = \rho/\epsilon_0$, where ρ stands for the charge density. In an FEL, it could be written as:

$$\frac{\partial \tilde{E}_z(z,t)}{\partial z} = \frac{\tilde{\rho}_1(z)}{\epsilon_0}\exp(i\phi),$$

(2.45)

with $\tilde{\rho}_1$ the first Fourier coefficient of the current density distribution. Since the space charge modulation is periodic, the derivative along the z-direction can be approximated using the SVEA approach $\frac{\partial \tilde{E}_z(z)}{\partial z} \approx ik\tilde{E}_z(z)$. By substituting this expression into Equation 2.45, we can
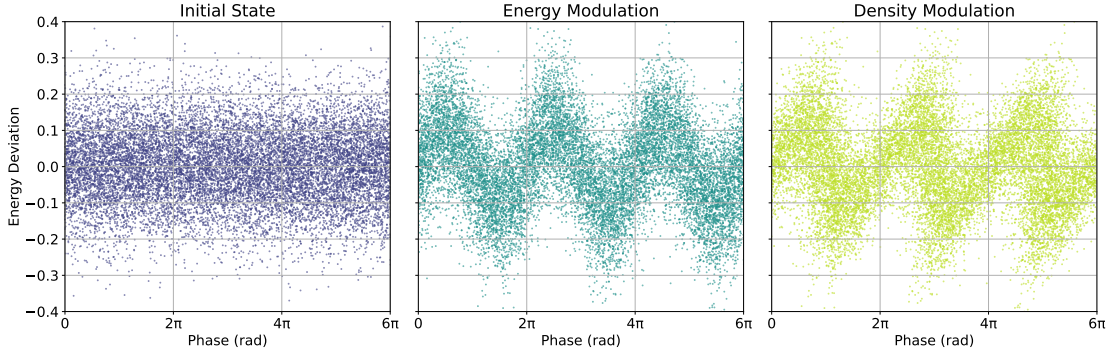
Figure 2.6: Visualisation of the electron beam micro bunching process. The first figure depicts the initial state with a uniform distribution of electrons. In the middle figure, the electrons introduce an energy modulation after interaction with radiation. The energy modulation is converted into density modulation and forms the microbunch in the right plot.

conclude that

$$\tilde{E}_z(z) = -\frac{i}{\epsilon_0 k}\tilde{\rho}_1(z) = -\frac{-i\mu_0 c^2}{\omega_0}\tilde{j}_1(z) \tag{2.46}$$

Equation 2.46 demonstrates the relationship between longitudinal forces and changes in charge density. The concentrated electron beams within the microbunch cause an increase in the Coulomb force between the electrons, leading to their repulsion and consequent space charge effect.

For the space charge effect in a single microbunch, the following result can be obtained by combining equation (2.46) with equation (2.44) and eliminating $\tilde{j}_1$, according to [12] :

$$\tilde{E}_z(z) = -\frac{i4\gamma_0 c}{\omega_0 K[JJ]}\frac{d\tilde{E}_x}{dz} \tag{2.47}$$

2.2.3   FEL Equation Sets Including Beam Density

In the first section, we have derived the phase space trajectory of an ensemble of electrons in the presence of an electromagnetic field in an undulator, as well as in the presence of a radiation wave. The phase evolution in the longitudinal direction of a relativistic electron is as follows:

$$\frac{d\phi}{dz} = 2k_u\eta, \tag{2.48}$$

where η represents the relative deviation in energy from the resonant energy. Its change along the undulator coordinate due to the coupling of fields in the case of a planar undulator is:

$$\frac{d\eta}{dz} = -\frac{eE_0 K[JJ]}{2m_e c^2 \gamma_0^2} \cos\phi \tag{2.49}$$

So far, we have treated the electric field amplitude E_0 as a constant to simplify the complexity of the dynamics. This applies to the short undulator. In cases of high gain, the amplitude may undergo significant changes and exhibit exponential growth. It must be treated as a z-dependent variable. Although the electric field $\tilde{E}_x(z)$ has a complex form, for simplicity, it is considered to be a real quantity. Hence, the equation (2.49) can be expressed conveniently as follows:

$$\left[\frac{d\eta}{dz}\right]_{coupling} = -\frac{eK[JJ]}{2m_e c^2 \gamma_0^2} \Re(\tilde{E}_x e^{i\phi}) \tag{2.50}$$

The space charge force has been discussed in the context of the micro-bunching of the electron beam. This force has an impact on energy deviation through the electric field in the longitudinal direction in 1D approximation, the change rate without the undulator field can be written as

$$\left[\frac{d\eta}{dz}\right]_{space\text{-}charge} = -\frac{e}{m_e c^2 \gamma_0} \Re(\tilde{E}_z e^{i\phi}) \tag{2.51}$$

Combine the two fields yields

$$\frac{d\eta}{dz} = \left[\frac{d\eta}{dz}\right]_{coupling} + \left[\frac{d\eta}{dz}\right]_{space\text{-}charge} = -\frac{e}{m_e c^2 \gamma_0} \Re\left[(\frac{K[JJ]\tilde{E}_x}{2\gamma_0} + \tilde{E}_z)e^{i\phi}\right] \tag{2.52}$$

The next step is to evaluate how this combined field acts on the electrons and changes beam density. If we look at the particles as point-like, their longitudinal distribution can be written as

$$S(\phi) = \sum_{n=1}^{N} \delta(\phi - \phi_n), \quad \phi, \phi_n \in [0, 2\pi] \tag{2.53}$$

We keep the assumption of treating an infinitely long electron beam. Initially, the beam density is assumed to be homogeneous everywhere. With the presence of the radiation field, the electron beam is modulated, grouped and bunched with a distance equal to the radiation wavelength. The electron beam is divided into several short slices, which allows us to expand the distribution into the Fourier series:

$$S(\phi) = \frac{c_0}{2} + \Re\left[\sum_{k=1}^{2\pi} c_k e^{ik\phi}\right], \tag{2.54}$$

with the coefficients,

$$c_k = \frac{1}{\pi} \int_0^{2\pi} S(\phi) e^{-ik\phi} \, d\phi \tag{2.55}$$

The current density can be expressed in Fourier coefficients. Initially, it is a DC current density proportional to the zeroth order Fourier coefficient. Thus, $c_0/2 = N/2\pi$. We define a segment of the electron bunch with transverse size A_b, then the number of electrons within one wavelength is $n_e = N/(A_b \lambda_r)$. Applying $j_0 = -ecn_e$ yields the result:

$$j_0 = -ec\frac{2\pi}{A_b\lambda_r} \cdot \frac{c_0}{2}, \tag{2.56}$$

where n_e is the number of electrons per unit volume, N is the number of electrons within the slice area of A_b and the longitudinal length λ_r, j_0 is the electron density at DC current. j_0 denotes the electron density with a DC current, while the modulation current $\tilde{j}_1$ is proportional to the first-order Fourier coefficients c_1:

$$\tilde{j}_1 = -ec\frac{2\pi}{A_b\lambda_r}c_1 = 2j_0 c_1/c_0 = j_0\frac{2}{N}\sum_{n=1}^{N} e^{-i\phi_n}, \tag{2.57}$$

with $c_1 = 1/\pi \sum_{n=1}^{N} e^{-i\phi_n}$ the first order coefficient.

With these results, we can finally write down the coupled equation in the first-order coupled equation for a periodic model. They are, respectively,

$$\frac{d\phi_n}{dz} = 2k_u\eta_n, \quad n = 1, 2, 3...N, \tag{2.58a}$$

$$\frac{d\eta_n}{dz} = -\frac{e}{m_e c^2 \gamma_0}\Re\left[(\frac{K[JJ]\tilde{E}_x}{2\gamma_0} + \tilde{E}_z)e^{i\phi_n}\right], \tag{2.58b}$$

$$\tilde{j}_1 = j_0\frac{2}{N}\sum_{n=1}^{N} e^{-i\phi_n}, \tag{2.58c}$$

$$\frac{d\tilde{E}_x}{dz} = -\frac{\mu_0 cK[JJ]}{4\gamma_0}\tilde{j}_1 \tag{2.58d}$$

Equation (2.58a) shows how the phase, ϕ_n, changes, and equation (2.58b) explains the change in energy, η_n, for each electron ($n = 1, 2, 3...N$). Equation (2.58c) describes how the charge density scale with the collective of bunching, while equation (2.58d) shows the change in radiation amplitude along the undulator coordinate. Because the number N is very large, finding an exact solution to $2N + 1$ sets of equations is computationally costly.

2.2.4 Analytical Solution of the FEL Equation

Given its large number of electrons, the first-order equation set becomes a complex many-body problem, which can be computationally expensive. However, this can be reformulated into a third-order differential equation.

The approach is motivated by three first-order differential equations, as shown in Equation (2.58). Instead of treating these equations individually over variables like phase, energy offset, and radiation field, they can be transformed into a single third-order differential equation concerning just the radiation field $\tilde{E}_x$. This transformative approach eliminates parameters ϕ_n and η_n, paving the way for an analytical solution that details power growth.

A derivation of this procedure is provided in Section 4.7 of [12]. By following this methodology, the resultant equation is:

$$\tilde{E}_x''' + i4k_u\eta\tilde{E}_x'' + (k_p^2 - 4k_u^2\eta^2)\tilde{E}_x' - iG^3\tilde{E}_x = 0 \tag{2.59}$$

Equation 2.59 represents the third-order equation of the high-gain FEL for a cold electron beam.

It is important to note that η here does not measure the distance between electron energy γ_j and resonance energy γ_r due to the assumption of non-constant radiation intensity. If one were to discuss the process on an individual electron basis, a high gain FEL could not be achieved. Instead, η reflects the collective impact of the entire electron beam, demonstrating the average energy γ_0 of the beam relative to the resonance energy γ_r. We will delve further into collective variables in a later section.

In this equation, two novel coefficients have been incorporated to consolidate all the constants for concision. The first is the gain parameter, symbolized as G, and the second is the space charge parameter, denoted by k_p. The definitions of these coefficients are as follows:

$$G = \left[\frac{\mu_0 K^2[JJ]^2 j_0 k_u e}{4\gamma_0^3 m_e c}\right]^{\frac{1}{3}}, \quad k_p = \left[\frac{2\mu_0 j_0 k_u e}{\omega_0 \gamma_0 m_e}\right]^{\frac{1}{2}} \tag{2.60}$$

We can rewrite Equation (2.59) using a normalisation factor to provide context for the FEL parameter. This involves dividing both sides of the equation by G^3, resulting in:

$$\frac{\tilde{E}_x'''}{G^3} + i2\left(\frac{2k_u\eta}{G}\right)\frac{\tilde{E}_x''}{G^2} + \left[\frac{k_p^2}{G^2} - \left(\frac{4k_u^2\eta^2}{G^2}\right)\right]\frac{\tilde{E}_x'}{G} - i\tilde{E}_x = 0 \tag{2.61}$$

To further simplify the equation, we introduce a scaling parameter and define the FEL param-

eter ρ [14] as:

$$\rho = \frac{G}{2k_u} = \left[\frac{\mu_0 K^2 [JJ]^2 n_e}{32\gamma_0^3 k_u^2 m_e} \right]^{\frac{1}{3}} \tag{2.62}$$

The dimensionless FEL parameter ρ, also known as the Pierce parameter [29], characterises the interaction intensity between the electron beam and the radiation field as well as the efficiency and performance of the FEL process. A higher value of ρ implies a more significant interaction, resulting in a faster FEL process.

Analytical solution of cubic equation

We begin by addressing the simplest form of the cubic equation. Assuming the space charge force is negligible ($k_p = 0$), and all the electrons are in resonance (i.e., $\eta = (\gamma - \gamma_r)/\gamma_r = 0$), the cubic equation 2.59 simplifies to:

$$\tilde{E}_x''' - iG^3 \tilde{E}_x = 0 \tag{2.63}$$

With the ansatz $E_x(z) = E_0 \exp(\alpha z)$, the roots of this equation are:

$$\alpha_1 = e^{i\frac{\pi}{6}} G \qquad \alpha_2 = e^{i\frac{5\pi}{6}} G \qquad \alpha_3 = e^{i\frac{9\pi}{6}} G \tag{2.64}$$

By applying Euler's formula, these roots can be rewritten in a more explicit form:

$$\alpha_1 = \frac{(i + \sqrt{3})G}{2} \qquad \alpha_2 = \frac{(i - \sqrt{3})G}{2} \qquad \alpha_3 = -iG \tag{2.65}$$

The three roots are illustrated in figure 2.7, which contribute to amplification in unique ways:

- α_1 has a positive real part, which results in exponential power growth.

- α_2 has a negative real part, leading to exponential decay.

- α_3 lacks a real part, causing oscillations with constant amplitude as a function of z.

The general solution for equation (2.63) can be expressed as a combination of these three solutions, which represents the diverse behaviours of the electron beam and its interaction with the radiation field:

$$\tilde{E}_x(z) = \frac{E_0}{3} \left[e^{\frac{1}{2}(i+\sqrt{3})Gz} + e^{\frac{1}{2}(i-\sqrt{3})Gz} + e^{-iGz} \right] \tag{2.66}$$

This solution (2.66) assumes that both the first and second derivatives of $\tilde{E}_x$ are zero at the entrance of the undulator, e.g. $\tilde{E}_x' = 0, \tilde{E}_x'' = 0$, which is a simplified initial condition.

23
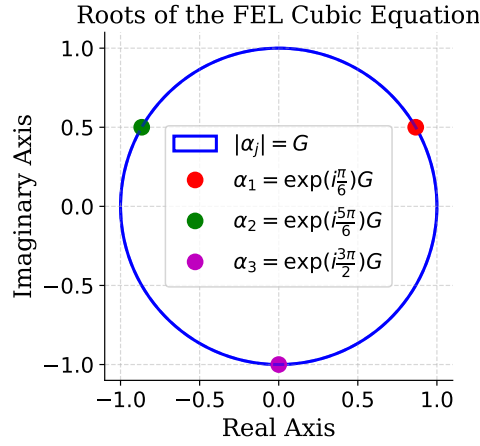
Figure 2.7: The diagram visualizes the three roots of the FEL cubic equation plotted on a complex plane. The roots are labeled as α_1, α_2, and α_3, positioned at angles $\frac{\pi}{6}$, $\frac{5\pi}{6}$, and $\frac{3\pi}{2}$, respectively, from the positive real axis. The surrounding circle indicates the boundary $|\alpha_j| = G$.

In the power profile, the three roots of the equation contribute with similar strength, resulting in an increase in power that is not observed in the initial stage of the FEL process. This stage is called the lethargy regime, as shown in Figure 2.8, where for the first three gain lengths, the obtained power growth from the approximation characterises this region as the lethargy regime.

However, when the beam and radiation are propagating together in a long undulator, the exponential growth rate of α_1 will eventually dominate as it grows faster than the other two. Thus the contributions of α_2 and α_3 become negligible and the field simplifies to:

$$E_x(z) \approx \frac{E_0}{3} \exp(\frac{\sqrt{3}Gz}{2})$$ (2.67)

The power of the radiation then becomes:

$$P(z) \propto |\tilde{E}_x(z)|^2 \approx \frac{E_0^2}{9} \exp(\sqrt{3}Gz) = \frac{E_0^2}{9} \exp(\frac{z}{L_{g0}}),$$ (2.68)

where a new parameter is introduced in 2.68: the gain length L_{g0}, defined as follows:

$$L_{g0} = \frac{1}{\sqrt{3}G} = \frac{1}{4\pi\sqrt{3}} \frac{\lambda_u}{\rho}$$ (2.69)

The gain length measures the rate of FEL power growth under ideal conditions. The subscript '0' indicates fundamental mode operation, distinguishing it from L_g, which is the gain length
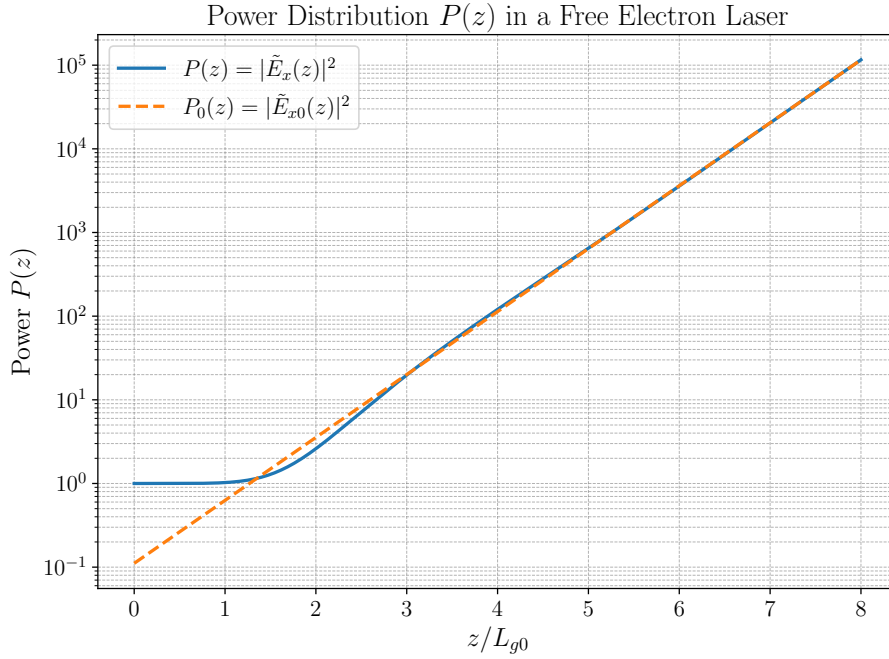
Figure 2.8: Power distribution $P(z)$ plotted on a semi-logarithmic scale. The solid line represents the full power distribution $P(z) \sim |\tilde{E}_x(z)|^2$, while the dashed line shows the power distribution $P_0(z) \sim |\tilde{E}_{x0}(z)|^2$ for the first root of the electric field expression, as described in Eq.2.67. The figure shows that the approximation is mainly valid for long undulators.

measurable in real experiments. A shorter gain length indicates greater efficiency in the energy transfer from the electron beam to the radiation, resulting in increased amplification over a shorter undulator length. Minimising the gain length is often a key objective in an FEL facility design.

2.3   Analysis of Ensemble of Electrons with Collective Variables

Beyond the perturbation method, a more general approach can be used to represent the system using the Vlasov equation, as it includes the effects of finite energy spread. We start by looking at the system through collective variables.

2.3.1   Collective Variables

Given the vast number of electrons, a single electron's description is not sufficient to fully characterize the electron beam. Therefore, to fully capture the behaviour of the beam, we will adopt a collective approach and adjust multiple parameters. There are two different types of collective parameters, one type is the z-dependent parameters: the bunching, energy modulation and radiation fields, where the bunching is commonly used for FEL simulation

analysis; another type of collective parameters are z-independent, such as the detuning parameters and the energy spread, which are input variables.

- **Bunching factor**

  The bunching factor quantifies the coherence of particle clustering in the phase space of an electron beam. It is defined as :

$$b = \left| \frac{1}{N} \sum_{j=1}^{N} \exp(i\phi_j) \right|, \tag{2.70}$$

  where N is the number of electrons, ϕ_j describes the position of the jth electron in longitudinal phase space.

  When all electrons cluster at a particular phase, the bunching factor approaches 1, indicating strong bunching. If the electrons are uniformly distributed in phase space, the bunching factor is near 0, indicating no bunching.

- **Detuning parameter**

  The energy detuning parameter, Δ, has been already introduced in the high gain FEL, where the FEL radiation gain is considerable. The parameter is defined as:

$$\Delta = \frac{<\gamma> - \gamma_r}{\gamma_r}, \tag{2.71}$$

  where $<\gamma>$ represents the average energy of the electron beam.

  Although the detuning parameter can range from -1 to infinity, the relativistic electron energy loss in an X-ray FEL is only a small fraction of the total energy, so the detuning parameter is typically very small. A 0.1% change can result in a significant difference in laser efficiency.

- **Energy spread parameter**

  The detuning parameter determines the average deviation in energy, but it does not account for the natural variation in the initial energy of each electron. To address this, we must calculate the average squared deviation. We define the energy spread parameter as:

$$\sigma_E^2 = \frac{<(\gamma - <\gamma>)^2>}{<\gamma>^2} \tag{2.72}$$

  In the X-ray FEL, the energy spread varies from 0 to 1. Nonetheless, even a minimal increment in the energy spread parameter, such as 0.1%, could negatively impact the resonance while assessing the beam's overall performance.

2.3.2 Vlasov Equation and Laplace Techniques

When utilizing the perturbation method, it is assumed that employing a uniform electron distribution with minimal energy and phase variations simplifies the computations. However, computing the direct derivative over the dispersive equations poses a challenge, particularly with a non-zero energy spread.

We are examining a group of electrons characterized by a distribution function $f(\phi, \eta, z)$. It is assumed that the interactions between electrons are much weaker than their interactions with collective magnetic and radiation fields. As stated by Liouville's Theorem, the electron phase distribution f remains unchanged throughout co-propagation despite the collective interaction, as long as a Hamiltonian can describe it. It holds:

$$\frac{df}{dz} = \frac{\partial f}{\partial z} + \frac{\partial f}{\partial \phi}\frac{d\phi}{dz} + \frac{\partial f}{\partial \eta}\frac{d\eta}{dz} = 0 \tag{2.73}$$

The system's evolution is described by the Vlasov equation and the distribution function $f(\eta, \phi, z)$.

In line with our previous section's methodology, we assume a minor perturbation in the electron beam's energy distribution, denoted by $f_1(\eta)$. We can express f as a Taylor series expansion up to the first order, given by $f = f_0 + f_1 e^{i\phi} + f_1^* e^{-i\phi}$. We have obtained the first order equation in (2.58a, 2.58b). As a reminder,

$$\frac{d\phi_j}{dz} = 2k_u \eta_j, \tag{2.74a}$$

$$\frac{d\eta_j}{dz} = -\frac{e}{m_e c^2 \gamma_0^2}\Re\left[\frac{K[JJ]\tilde{E}_x}{2\gamma_r} + \tilde{E}_z\right]e^{i\phi} \tag{2.74b}$$

In Equation 2.74b, every electron's energy is measured relative to the resonance energy. To break down the deviation, we can separate it into two components - the deviation of the jth electron from the average energy and the deviation of the average energy from the resonance energy. The latter is known as the energy detuning parameter. We can reformulate the phase evolution as:

$$\begin{aligned}
\frac{d\phi}{dz} &= 2k_u \frac{\gamma - \langle\gamma\rangle + \langle\gamma\rangle - \gamma_r}{\gamma_r} \\
&= 2k_u\left[\frac{\gamma - \langle\gamma\rangle}{\gamma_r} + \frac{\langle\gamma\rangle - \gamma_r}{\gamma_r}\right] \\
&\simeq 2k_u(\delta + \Delta),
\end{aligned} \tag{2.75}$$

where Δ is the detuning parameter defined in Equation 2.71. The variable δ denotes the energy deviation of a particle from the average energy $<\gamma>$, while Δ represents the gap between the resonance energy and $<\gamma>$.

In the Vlasov equation, when discussing a certain phase, all the terms, when grouped by the

power of the item $e^{i\phi}$ after inserting the Ansatz in Eq 2.73, will be individually zero. To apply this simplification, two conditions must be met. Firstly, Slowly-Varying Envelope Approximation (SVEA) must be applicable to slow down energy changes. Secondly, the distance z being taken into consideration should be considerably larger than an undulator period. If both prerequisites are fulfilled, it is possible to exclude the term $e^{i\phi}$ without affecting the validity of the treatment. The terms proportional to $e^{i\phi}$ gives:

$$\frac{\partial \tilde{f}_1}{\partial z} + 2ik_u(\delta + \Delta)\tilde{f}_1 - \frac{e}{m_e c^2 \gamma_0}\left[\frac{K[JJ]\tilde{E}_x}{2\gamma_0} + \tilde{E}_z\right]\frac{\partial f_0}{\partial \delta} = 0 \tag{2.76}$$

In order to obtain solutions to the Vlasov equation, we need to set boundary conditions. If we assume that the initial electron beam is homogeneous with no density or energy modulations, we can have the boundary conditions as follows:

$$f_0\big|_{z=0} = N_0 F(\delta), \qquad \tilde{f}_1\big|_{z=0} = 0, \qquad \int F(\delta)\,d\delta = 1 \tag{2.77}$$

F is the energy distribution function of the electron beam, representing the electron energy distribution at the undulator entrance. This is a normalised function, so the integral of F over the entire electron beam equals 1. N_0 represents the number of electrons. After applying the boundary conditions, we observe that for f_1 the Vlasov equation 2.76 takes the form of $y(z)' - iAy(z) = x(z)$, where A is a constant. The general solution of this type of partial differential equation can be written as follows:

$$y(z) = \int_0^z x(s)e^{iA(z-s)}\,ds + C_1 e^{iAz} \tag{2.78}$$

C_1 is an arbitrary constant. Since there is an initial condition $f_1\big|_{z=0} = 0$, upon unmodulated beam the constant C_1 is 0. The solution to equation 2.76 is therefore

$$\tilde{f}_1(\delta, z) = -\frac{en_0}{m_e c^2 \gamma_0}\frac{dF}{d\delta}\int_0^z\left[\frac{K[JJ]\tilde{E}_x(z')}{2\gamma_0} + \tilde{E}_z(z')\right]e^{i2k_u(\delta+\Delta)(z'-z)}\,dz' \tag{2.79}$$

The quantity f_1 represents the first-order perturbation of the electron distribution. As a reminder, the particle distribution can be separated into a zeroth-order and first-order perturbation terms, such that $f = f_0 + \tilde{f}_1 e^{i\phi} + c.c.$. The current density of the beam can be obtained by integrating the particle distribution over energy and multiplying by c and e, which yields $\tilde{j}_z = -j_0 + \tilde{j}_1 e^{i\phi} + c.c.$. We must integrate the distribution function $\tilde{f}_1$ to determine the perturbed current density $\tilde{j}_1$. This integration results in the following expression:

$$\tilde{j}_1 \simeq -ec\int \tilde{f}_1\,d\delta = -\frac{e^2 n_0}{m_e c\gamma_0}\int_{-\infty}^{\infty}\frac{dF}{d\delta}\int_0^z\left[\frac{K[JJ]\tilde{E}_x(z')}{2\gamma_0} + \tilde{E}_z(z')\right]e^{i2k_u(\delta+\Delta)(z'-z)}\,d\delta\,dz' \tag{2.80}$$

We can now use the previously derived equation 2.44 and equation 2.47

$$\frac{d\tilde{E}_x}{dz} = -\frac{\mu_0 cK[JJ]}{4\gamma_0}\tilde{j}_1, \qquad \tilde{E}_z(z) = -\frac{i4\gamma_0 c}{\omega_0 K[JJ]}\frac{d\tilde{E}_x}{dz} \tag{2.81}$$

Now, we reach the last step of the section by substituting 2.80 and 2.47 into 2.44 and obtain:

$$\frac{d\tilde{E}_x}{dz} = -\frac{e^2 n_0 \mu_0 K[JJ]}{4\gamma_0^2 m_e} \int_{-\infty}^{\infty} \frac{dF}{d\delta} \int_0^z \left[\frac{K[JJ]\tilde{E}_x(z')}{2\gamma_0} - \frac{i4\gamma_0 c}{\omega_0 K[JJ]} \frac{d\tilde{E}_x(z')}{dz} \right] e^{i2k_u(\delta+\Delta)(z'-z)} d\delta\, dz'$$

(2.82)

Equation 2.82 is an integrodifferential equation that combines integration and differentiation. It describes the evolution of the electric field $\tilde{E}_x$ as a function of the position z. It contains a convolution integral that accounts for the interaction of the electric field at different positions along the z-axis, including the electron energy distribution and bunching.

The equation includes a term involving F, which describes energy spread and can not be accurately described using perturbation methods in the previous section. It can have various shapes, such as rectangular, Gaussian, and Lorentzian distributions. If we set F as Dirac delta distribution such as $F = n_0 \boldsymbol{\delta}(\delta)$ and perform a partial differentiation on the electron bunching scaling z' in Equation 2.82, we obtain a result involving multiple partial derivatives of E_x, similar to what has been discussed in the section without collective variables.

To solve the integral equation in the presence of energy spread, we employ a unique method that utilizes Laplace transforms, inverse Laplace transforms, and the Gaussian residue theorem. The derivation of the solution to the integro-differential equation (2.82) is given in **Appendix A**. While the results are consistent with those obtained using the perturbation method, the latter approach has the additional advantage of taking into account the energy spread.

2.3.3   FEL Instability and Saturation

Electrons would synchronize perfectly with the radiation phase in a setting without detuning. This synchronization leads to an optimal energy exchange and maximum radiation growth.

However, the introduction of detuning changes the phase-matching condition between the electrons and the radiation wave throughout the FEL process. Electrons that were initially synchronised with the radiation field can fall out of phase, reducing the efficiency of the energy exchange. Similarly, energy spread within the electron beam can further affect this efficiency. These factors affect the instability of the growth rate, which determines the rate at which the radiation intensity increases. The growth rate is highest in the absence of detuning and energy spread.

The amplifying radiation extracts energy from the electron beam throughout the process. A significant fraction of the electrons lose energy until they are out of resonance. As a result, the amplification begins to slow down due to increased losses. Eventually, a point is reached where the gain of the radiation is neutralised by its loss, resulting in a stabilised radiation intensity. This state of equilibrium is called **saturation**. Typically, the saturation energy is scaled with $\sim \rho$.

2.4   Start From Noise: Self-Amplified Spontaneous Emission

This section explores the principles and characteristics of Self-Amplified Spontaneous Emission (SASE) [14, 30, 31, 32]. We first investigate the initial shot noise characterization, showing the stochastic nature of SASE. We then delve into the coherence properties, bandwidth, spectrum, and peak intensity, examining their interdependence and influence on FEL performance. The spontaneous emission serves as a seed for the amplification process, the basis for the simulations in this thesis study.

2.4.1   Shot-Noise Characterization

We begin with the shot-noise characterization, where the electrons in the beam are randomly spaced, and their arrival time at the entrance of the undulator varies. The beam current is given by

$$I(t) = (-e) \sum_{k=1}^{N} \boldsymbol{\delta}(t - t_k), \tag{2.83}$$

where N is the number of electrons within a finite electron slice with duration T, t_k denotes a random arrival time of an electron. The Fourier Transformation of the current is:

$$\overline{I}(\omega) = \int_{-\infty}^{\infty} e^{i\omega t} I(t) dt = (-e) \sum_{k=1}^{N} e^{i\omega t_k} \tag{2.84}$$

which is the sum of many complex phasors with random phases ωt_k. We calculate the first-order correlation of the Fourier harmonics, namely $\overline{I}(\omega)$ and $\overline{I}(\omega')$:

$$\langle \overline{I}(\omega) \overline{I}^*(\omega') \rangle = e^2 \langle \sum_{k=1}^{N} \sum_{n=1}^{N} e^{i\omega t_k} e^{-i\omega' t_n} \rangle \tag{2.85}$$

$$= e^2 \left\langle \sum_{k=1}^{N} e^{i(\omega - \omega') t_k} \right\rangle + e^2 \left\langle \sum_{k \neq n} e^{i\omega t_k - i\omega' t_n} \right\rangle \tag{2.86}$$

The second term is the contribution of incoherent bunching, which is entirely random. To simplify the result, assume that the number of electrons is infinite, e.g., $N \to \infty$. The result becomes

$$\langle \overline{I}(\omega) \overline{I}^*(\omega') \rangle = \lim_{N \to \infty} e^2 \left\langle \sum_{k=1}^{N} e^{i(\omega - \omega') t_k} \right\rangle \tag{2.87}$$

When we take the beam duration as infinity, the expression can then be written as:

$$\langle \overline{I}(\omega) \overline{I}^*(\omega') \rangle = 2\pi e I_0 \boldsymbol{\delta}(\omega - \omega'), \tag{2.88}$$

where I_0 is the average current over the duration T, with $eN = I_0 T$. Equation 2.88 represents the first-order spectral correlation.

2.4.2   SASE Power in the Linear Regime

The initial shot noise is defined by the first-order correlation, which is based on the properties of 'white noise'. The second-order correlation function is expressed as $1 + |g_1|^2$. This function is used to evaluate the intensity fluctuations of the noise over time, where g_1 represents the first-order correlation. To establish the connection between the output signal and its corresponding input noise signal, we use Green's functions. The radiation field can be expressed as:

$$E_y(z, t) = \frac{1}{2\pi} \int_{-\infty}^{\infty} \overline{E}(\omega, z) e^{i\omega t} d\omega, \tag{2.89}$$

with the Fourier harmonics of radiation field $\overline{E}(\omega, z)$ written as

$$\overline{E}(\omega, z) = g(\omega, z)\overline{I}(\omega), \qquad \omega > 0, \tag{2.90}$$

here $g(\omega, z)$ is the spectral Green's function. When $\omega < 0$, the Fourier transform turns into $\overline{E}^*(\omega, z) = E(-\omega, z)$.

In the linear regime of SASE, the stochastic process follows the central limit theorem [10], which results in the probability distribution p as

$$p_I(I) = \frac{1}{\langle I \rangle} e^{-I/\langle I \rangle}, \tag{2.91}$$

with an intensity fluctuation of 100%. Each electron contributes to a given radiation frequency, which are different only in radiation phases. Even though each electron's contribution might be random and possibly not normally distributed, the sum of all their contributions will tend to be a Gaussian distribution. On page 363 of [10], the radiation energy in one radiation pulse is derived. Applying Poynting's vector and Parseval's theorem, the result is

$$\langle E_{SASE} \rangle = \frac{cS}{4\pi^2} \int_0^{\infty} A e^{-\frac{(\omega-\omega_0)^2}{2\sigma_\omega^2}} \langle |I(\omega)|^2 \rangle d\omega, \qquad \omega > 0 \tag{2.92}$$

where S is the transverse surface of the electron beam, and

$$A = \frac{4}{9} \left(\frac{E_0}{I_0} \right)^2 e^{\sqrt{3}\hat{z}}, \qquad \sigma_\omega = 3\sqrt{\frac{2}{\sqrt{3}}} \frac{\rho\omega_0}{\sqrt{\hat{z}}}, \tag{2.93}$$

σ_ω is the frequency bandwidth, which is the width of the average spectrum. We can also characterise the coherence time by

$$T_{coh} = \frac{\sqrt{\pi}}{\sigma_\omega}. \tag{2.94}$$

The duration for which electrons can be correlated due to interactions with the radiation fields of other electrons is measured by the coherence time. To increase the coherence time, one can decrease the radiation bandwidth.

Suppose the coherence time is shorter than the electron beam length. In that case, several modes contribute to the formation of separated and uncorrelated radiation spikes, with the coherent mode number M estimated as :

$$M \simeq \frac{T_{bunch}}{T_{coh}} \tag{2.95}$$

As shown in [10, 33], the energy per pulse follows the gamma distribution:

$$p(W) = \frac{M^M}{\Gamma(M)} \left(\frac{W}{\langle W \rangle} \right)^{M-1} \frac{1}{\langle W \rangle} e^{-M\frac{W}{\langle W \rangle}} \tag{2.96}$$

Here, $\langle W \rangle$ represents the average or expected value of the energy per pulse, and $\Gamma(M)$ denotes the gamma function. The result is originally from [34] in statistical optics. The distribution is plotted in figure 2.9.
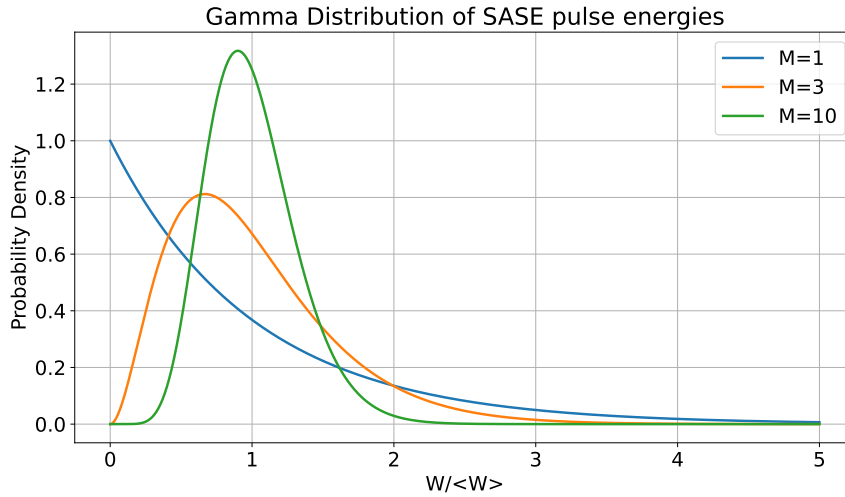
Figure 2.9: Gamma distribution of SASE pulse energies for various shape parameters M. The plot illustrates how the distribution of normalised energy per pulse varies with different M values. As M increases, the peak of the distribution becomes more pronounced and shifts towards higher average energies. The distribution for $M = 1$ is exponential while more peaked forms are obtained for higher M values.

2.5   Simulation Approach

Based on the understanding of the FEL theory, we discuss briefly the way of conducting simulations in FEL. There are four basic steps for a simulation in FEL [35]:

1. Generation of the initial phase space distribution for the electron beam.

2. Solving the ordinary differential equations for the electron beam variables.

3. Solving the partial differential equations associated with the radiation and electrostatic fields.

4. Management and documentation of radiation field and electron beam parameters, coupled with efficient allocation of computing resources to facilitate time-dependent simulation and ensure accurate results.

In this thesis, we use Genesis [1] as the simulation tool. Genesis is simulation code, utilizing a time-dependent and three-dimensional model of the FEL equations within the paraxial approximation for single-pass FEL simulations. Detailed information on Genesis's functionalities is available in [1, 35, 36]. We will discuss the input and output when performing a Genesis simulation.

2.5.1 Input

To run Genesis code, a minimum of two input files are necessary. The first file, known as the **.in file**, defines the beam parameters, including s (beam axis), current, energy spread, energy, beam size, and other basic beam parameters. The second file, known as the **.lat file**, defines the machine parameters, such as undulator parameters, chicane delays, and component longitudinal length.

It is worth noting that the undulator parameter inserted in the lattice file is typically represented as aw = K/ $\sqrt{2}$, rather than K directly. The thesis discusses either aw or K.

2.5.2 Output

The two prepared files are sent to the program to compute. In my PhD, I performed calculations using clusters, including the Euler cluster of ETH Zurich and Piz Diant of the Swiss National Supercomputing Centre (CSCS). The simulation results are obtained by reading the output files. Some parameters can be read directly, such as:

Table 2.1: Summary of direct-readout parameters

No.	Direct-readout parameters	Dimension	Unit
1	Time*	Assuming m^{**}	fs
2	z position	Assuming n	m
3	FEL power	$m \times n$	W
4	Electron energy	$m \times n$	/
5	Beam current at the entrance	$m \times 1$	A
6	Energy spread	$m \times n$	/
7	Bunching	$m \times n$	/

(*) Here, time is the output of Genesis, where $t-> s-ct$. The 's' is then normalized to show the length scale in time units, which is a practical measure.

(**)m and n are integers representing the size of the data.

This thesis will not discuss certain parameters, such as emittance, transverse position, and transverse velocity.

Additionally, some output parameters require extra calculations.

1. Pulse Energy ($1 \times n$)
The pulse energy is calculated using the integration of FEL power along the z direction. The dimension of pulse energy is $1 \times n$, with the unit Joule.

2. Spectrum ($m \times n$)
To analyze the spectrum of a time-domain signal, we first apply the fft function, which computes the Fast Fourier Transform of the signal. We then apply the fftshift to reorder the output of the fft so that the zero-frequency component is centered in the array.

3. Pulse duration ($1 \times n$)
The duration of the pulse is determined by directly measuring the FEL power at various z positions. Spikes are detected first, and then the FWHM of the spikes is measured, provided that they are detectable. The initial measurement position may vary from different simulations depending on the output data. In this thesis, pulse duration is always measured using FWHM.

3 Introduction to SwissFEL

This chapter introduces the SwissFEL. The Athos beamline of the SwissFEL is the basis for simulation in the PhD thesis. SwissFEL is a state-of-the-art free-electron laser facility at the Paul Scherrer Institute in Villigen, Switzerland [37, 38]. It delivers X-ray pulses with photon energies between 260 eV and 12.4 keV with high peak brightness [2, 3], giving researchers access to new domains of ultrafast X-ray science [39].

There are comparable facilities around the world, including LCLS [40] in the United States, SACLA [41] in Japan, SXFEL [42] in China, FERMI [43] in Italy, FLASH [44] and European XFEL [45] in Germany, and PAL [46] in South Korea.

This chapter presents the SwissFEL facility's design and layout and briefly introduces the main components, namely, the electron injector, the linear accelerators (linacs), the undulators and the end stations. The layout of SwissFEL is shown in the figure below.
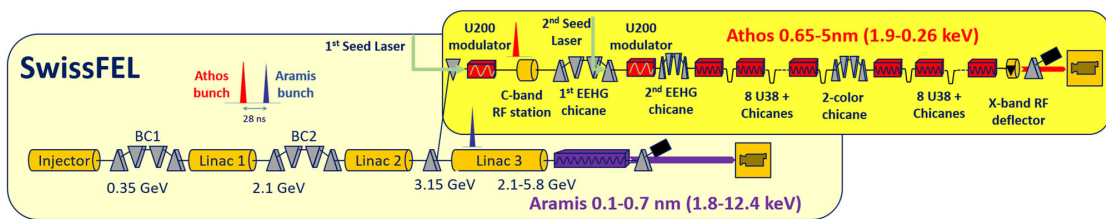
Figure 3.1: SwissFEL accelerator layout [4].

In the undulator part, we will show images of three configurations in Athos that are directly related to the short pulse generation in the thesis: they are the HERO modulator, the delaying magnetic chicanes and the transverse gradient undulator configuration.

3.1 Electron Injector

The SwissFEL electron injector initiates the electron beam, employing a 2.5-cell S-band RF photoinjector gun [47]. It releases 7.1 MeV electron bunches, which are generated by an

infrared Yb:CaF$_2$ laser interacting with a Cs$_2$Te-coated copper photocathode [48].
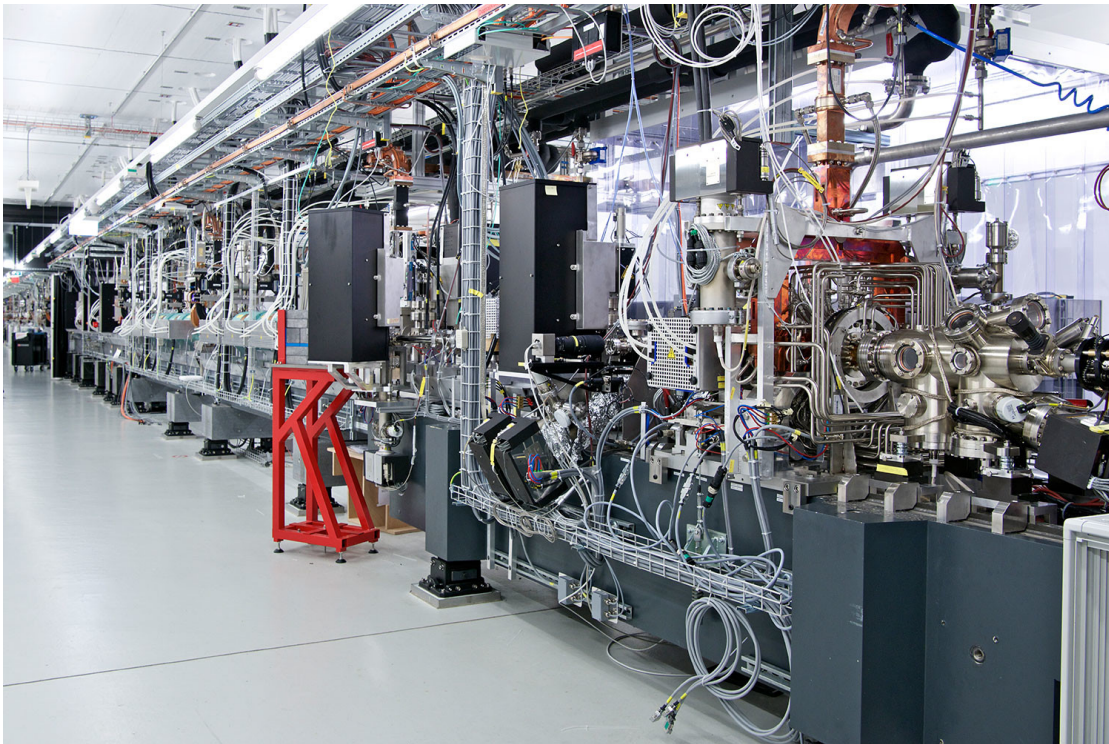
Figure 3.2: SwissFEL electron injector [49].

A subsequent booster linac enhances the beam's energy, preparing it for the compression stage in the first bunch compressor (BC1). The SwissFEL injector has two booster sections [50]. Booster 1, equipped with two S-band traveling-wave cavities, accelerates the electron beam to 150 MeV. It's followed by booster 2, which raises the electron energy to 300 MeV, enabling longitudinal bunch compression.

3.2   Linac

The linear accelerator comprises three segments - Linac 1, Linac 2, and Linac 3. Linac 1 elevates the energy of the electron beam up to 2.1 GeV, which is then subjected to additional compression within the second bunch compressor (BC2). Post Linac 2, the beam energy attains 3.15 GeV, and a switchyard [51] can direct electron bunches to the Aramis beamline or deflect them towards the Athos beamline. The configuration allows SwissFEL to simultaneously serve two separate beamlines [52].
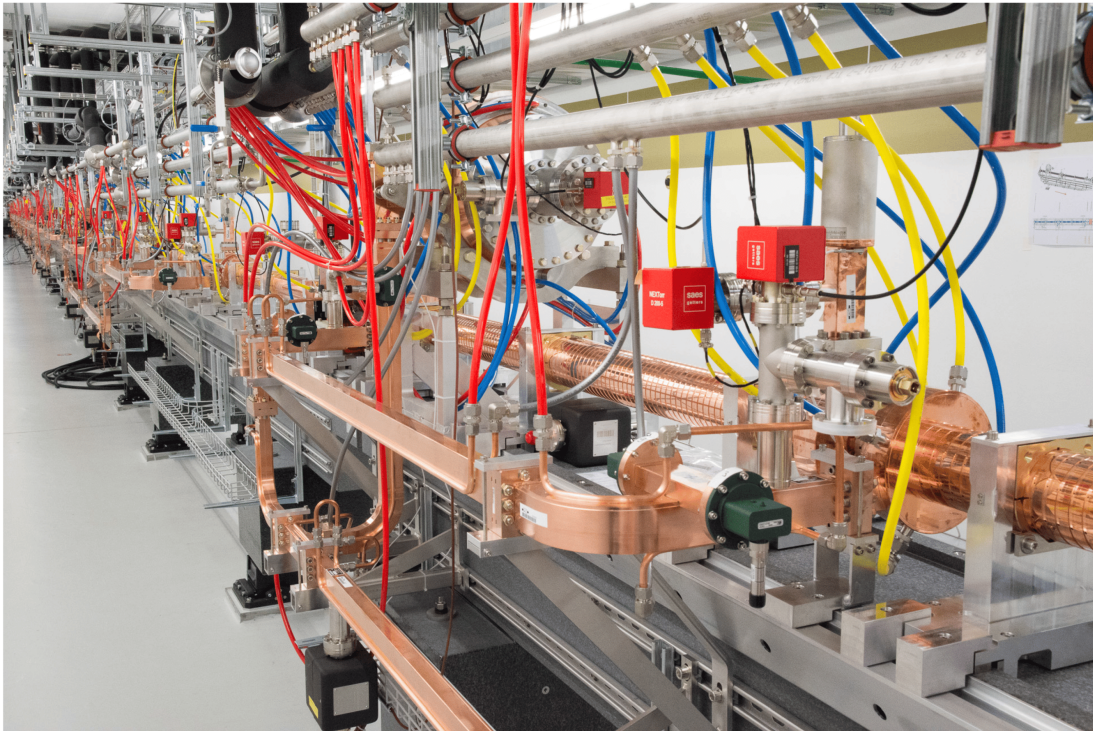
Figure 3.3: The Linac at SwissFEL. The showing part is a C-band in Linac [3].

3.3   Undulator

There are currently two undulator beamlines in the SwissFEL, the hard X-ray beamline Aramis and the soft X-ray beamline Athos.

Aramis Beamline

The Aramis undulator at SwissFEL is designed to cover the radiation wavelength range of 0.1-0.7 nm [53]. A planar undulator configuration is employed with dysprosium-enriched NdFeB [54] permanent magnets. The magnet array is mounted inside the vacuum tank, allowing for a small inter-magnet gap for the electrons [55]. There are 13 modules in Aramis, each 4 m long, with an undulator period of 15 mm.

Figure 3.4: Aramis undulator at SwissFEL. The Aramis undulator is 60 m long, with a 4 m length for each module and 0.75 m for each intersection [3].

The typical parameters of Aramis are in table 3.1:

Table 3.1: SwissFEL Aramis beamline parameters [2]

Electron accelerator	
Beam Energy	6.2 GeV
Energy Spread (r.m.s.)	1 MeV
Normalised Emittance	200 nm
Peak Current	3.0 kA
Undulator parameters	
Undulator Period, u	15 mm
Total Length	60 m
Photon parameters	
Wavelength	1–7 Å
Bandwidth	0.05–2.3 % [56]

Athos Beamline

The Athos beamline at SwissFEL is dedicated to generating soft X-rays in a photon energy range of 250-1900 eV [57, 5]. Athos undulator supports helical and planar operation modes [58]. It features 16 modules, each stretching 2 m with 0.75 m intersections, totalling 44 m. The electron beam delivered to Athos has a lower energy than Aramis because it bypasses Linac 3. There exists a C-band RF station located before the Athos undulator that has the capability of adjusting the beam energy by ±250 MeV [4]. Moreover, Athos has many unique configurations.

Figure 3.5: Athos undulator at SwissFEL. The Athos undulator is 44 m long, comprising 16 modules. Each module measures 2 m in length, with 0.75 m intersections between them [59].

The typical parameters are presented in table 3.2.

Table 3.2: SwissFEL Athos beamline parameters [4]

Electron accelerator	
Beam energy	2.9 - 3.4 GeV
Undulator parameters	
Undulator Period	38 mm
Undulator Module Length	2 m
Number of Modules	16
Period Number per Module	52
Intramodule Length	0.75 m
Total Length	44 m
Photon parameters	
Wavelength	0.65 - 5 nm
Pulse Energy	3 mJ at 1 keV

.

We present three configurations of Athos that are directly relevant to research in this thesis: the HERO modulator, the magnetic chicane positioned in each inter-undulator space, and the Apple X undulator configuration.

HERO modulator

In the high gain FEL, intense radiation induces modulation in electron energy and density, leading to exponentially growing microbunching [12]. Another approach is employing an intense external laser [60] to interact with the electron beam, producing an energy modulation with a much larger modulation amplitude.

Energy-modulated beams are foundational for advanced FEL techniques, particularly when generating short-duration pulses through methods like slicing [61] or ESASE [62]. The principle of generated energy-modulated beams will be further discussed in Chapter 4.

We employ the HERO modulator, where "HERO" stands for a research grant funded by the European Research Council (ERC), as detailed in [63]. The HERO modulator, as depicted in Figure 3.6, is dedicated to the HERO research program. The modulator consists of 8 periods, with a period length of 0.2 m. Considering the electron beam energy range, the K value varies between 12 and 36 to span the wavelength scale from 260 to 1600 nm [64].

Figure 3.6: HERO modulator at Athos beamline, the left shows an installed modulator with eight periods. The right figure shows one period [64].

Delaying magnetic chicane after each undulator module

Magnetic chicanes are commonly used throughout the SwissFEL facility. Specifically, we refer to the delaying magnetic chicanes located after each Athos undulator module, with much less strength than those for bunch compression.

The design of the magnetic chicane is presented in Figure 3.7. Four of the motors can control both halves of the magnetic track. The length of the magnetic track is 200 mm, and the minimum gap is 6 mm [5]. The electron beam can be delayed by as much as 5 fs for each break section relative to the radiation field.

The primary function of delaying chicanes is to serve as a phase shifter, a topic that will be explored in detail in Chapter 6. Beyond this fundamental role, delaying chicanes also have applications in optical klystrons, multi-stage fresh bunch configurations [65], and the enhancement of coherence length.
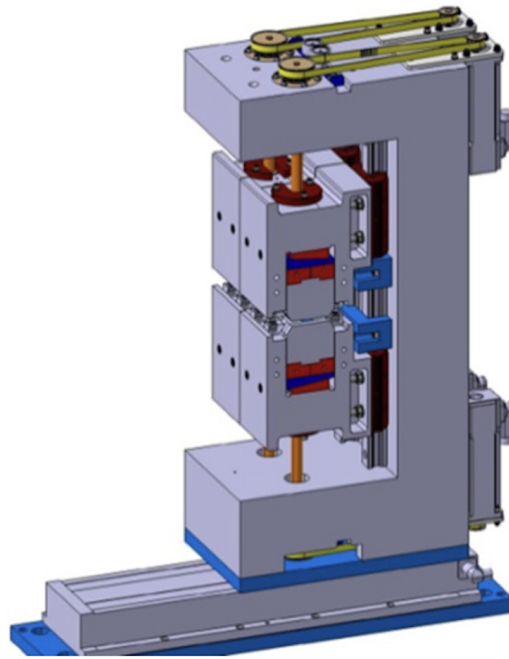
Figure 3.7: Delaying magnetic chicane after each Athos undulator module [5].

Apple X configuration

The APPLE (Advanced Planar Polarization Light Emitter) X configuration employs radially movable magnetic arrays within the undulator modules, which allow for precise tuning of the K value without necessitating any longitudinal shifts in the magnet arrays, thereby maintaining a consistent polarisation. The connection to research in the thesis is that the distinct asymmetry in the radial distances of the four magnetic arrays enables Athos to generate a transverse field gradient for all polarisations, a technical achievement known as a transverse-gradient undulator (TGU) [66], which will be helpful for generating ultra-short FEL pulses (see Chapter 7).
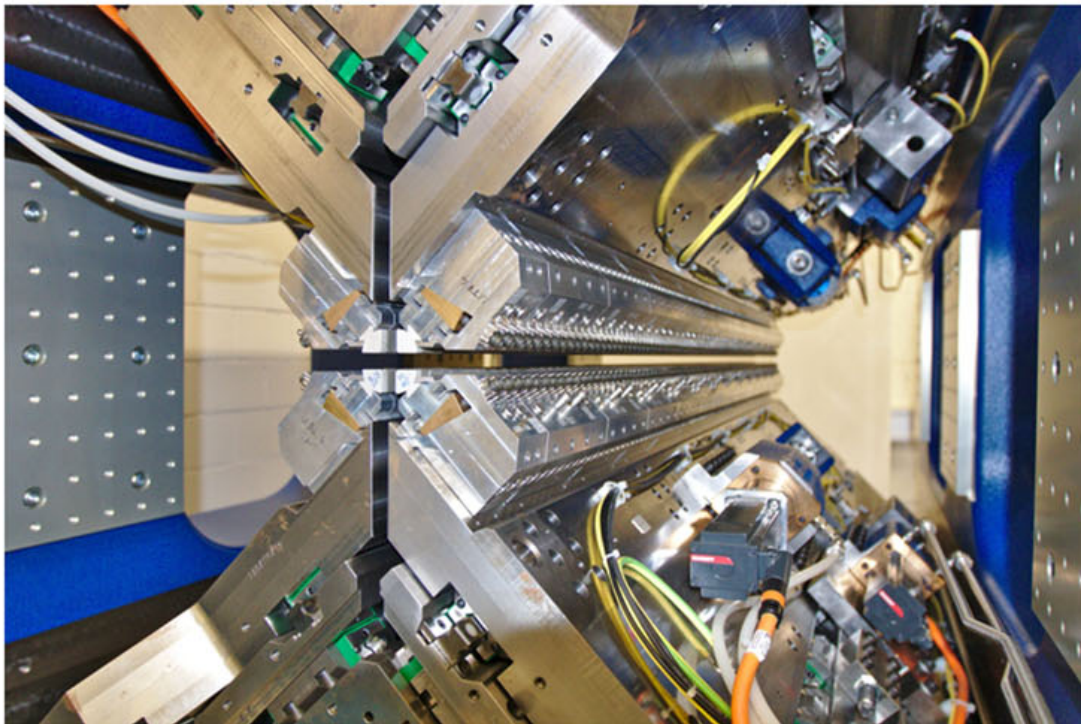
Figure 3.8: Apple X undulator [4].

3.4   Experimental Stations

The Aramis beamline at SwissFEL generates hard X-rays in the range of 1.8 to 12.4 KeV and consists of three different photon beamlines, each leading to individual experimental chambers. The Alvra experimental station is devoted to investigating ultrafast processes in photochemistry and photobiology, whereas the Bernina experimental station explores the ultrafast dynamics in condensed matter physics [67]. The Cristallina experimental station serves both quantum science and structural biology, allowing for imaging of quantum many-body states under extreme conditions and serial femtosecond protein crystallography [68].

The Athos beamline provides soft X-rays in the range of 0.26-1.9 KeV and contains two experimental stations. The Furka station is committed to investigating quantum materials through the utilisation of time-resolved resonant inelastic and elastic X-ray scattering as well as absorption spectroscopy [69]. The Maloja station principally focuses on atomic, molecular, and non-linear X-ray physics, and chemical dynamics [70].

The station with the most demand for ultrashort soft X-ray pulses is the Maloja station in the Athos beamline.

4 Slippage effect in SASE and Enhanced SASE

This chapter discusses the slippage effect and its impact in generating short pulses. Slippage refers to electrons in the undulator travelling slower than the group velocity of FEL light. As a result, FEL pulses generated by the electrons move towards the head of the electron beam. The slippage effect is evident in the soft X-ray regime, making it challenging to generate attosecond pulses. To generate such short pulses, we will discuss the possibility of using the Enhanced SASE (ESASE) method [62]. This involves using an external laser to manipulate electron energy and a magnetic chicane to create a current spike, which improves performance owing to the high electron density at the spike. The chapter concludes with simulation results indicating that ESASE alone is insufficient to address slippage in the soft X-ray region.

4.1 Slippage Effect

This section discusses the slippage effect in SASE. We first derive the FEL group velocity and the slippage speed. Then, we demonstrate the slippage effect in SASE simulations.

4.1.1 FEL Group Velocity

Group velocity is of particular interest in SASE FELs because the characteristic 'spike' in SASE radiation is a wave packet propagating at the group velocity.

For the specific case of SASE, Green's function is given (refer to page 362 in [10]):

$$g_{SASE}(\hat{z}, t) = \frac{2E_0}{3I_0} \exp\left[\frac{\sqrt{3}}{2}\left(1 - \frac{\hat{\Delta}^2}{9}\right)\hat{z} + \frac{i}{2}\left(1 - \frac{4\hat{\Delta}}{3}\right)\hat{z}\right] \exp(i\omega t + ik\hat{z}) \tag{4.1}$$

Here, $\hat{\Delta} = \Delta/G = \Delta/\rho * 2k_u$ represents the normalised detuning parameter. From this equation, we observe a change in wave number expressed as

$$k' = k + \frac{1}{2} - \frac{2}{3}\hat{\Delta} \tag{4.2}$$

Subsequently, the calculation of the group velocity is

$$v_g = \frac{d\omega}{dk'} = \left(\frac{dk'}{d\omega}\right)^{-1} = \left(\frac{dk}{d\omega} - \frac{2}{3}\frac{d\hat{\Delta}}{d\omega}\right)^{-1} = \left(\frac{1}{c} - \frac{2}{3}\frac{d\hat{\Delta}}{d\omega}\right)^{-1} \tag{4.3}$$

With two expressions from [12] :

$$\frac{d\hat{\Delta}}{d\omega} \approx \frac{k_u}{\omega}, \qquad ck_u = \omega\frac{1}{2\gamma_0^2}\left(1 + \frac{K^2}{2}\right), \tag{4.4}$$

the result of the calculation is :

$$v_g = c\left[1 - \frac{1}{3\gamma_0^2}\left(1 + \frac{K^2}{2}\right)\right] \tag{4.5}$$

4.1.2 Slippage speed

We compare the difference between the group velocity of the radiation and the average longitudinal velocity of electrons.

The average velocity of electrons using Equation (2.11) in [12] is:

$$\overline{v}_z = c\left(1 - \frac{1}{2\gamma_0^2}\left[1 + \frac{K^2}{2}\right]\right) \tag{4.6}$$

Then, the difference is :

$$v_g - \overline{v}_z = \frac{c}{6\gamma_0^2}\left[1 + \frac{K^2}{2}\right], \tag{4.7}$$

where v_g is smaller than the speed of light but still greater than the electron's speed. We define the **slippage speed** $v_{\rm sp}$ as :

$$v_{\rm sp} = c\frac{v_g - \overline{v}_z}{c - \overline{v}_z} = \frac{1}{3}c\frac{\lambda_r}{\lambda_u} \tag{4.8}$$

The FEL radiation light surpasses the electrons by one-third of a radiation wavelength for each undulator period. This result holds when the electrons are in complete resonance. When the electrons are completely out of resonance, the FEL light travels at the speed of light, with a slippage of one wavelength per period.

4.1.3 Slippage in SASE Simulation at Athos Undulator

In this subsection, we demonstrate the slippage effect in SASE simulations. We show the simulation result in two radiation frequencies, namely $\lambda_r = 1$ nm and $\lambda_r = 4$ nm.

Simulation setup

Table 4.1: Beam Parameters for SASE Simulation

Parameter	Value
Beam Center Energy	3.33 GeV
Beam Length	10000 nm
Current	3 kA
Energy Spread	501 keV
Emittance (x and y direction)	300 nm

The beam has a constant energy of 3.33 GeV, corresponding to $\gamma = 6653$. The beam is 10000 nm long, corresponding to a duration of 33.3 fs. For the undulator, aw = 1.153083 (1 nm), and aw = 2.884472 (4 nm), where aw = $K/\sqrt{2}$. The undulator parameter is the same for all modules.

4.1.4   Simulation Result

In this section, we present the results obtained from the Genesis simulation code [1]. Our focus is on the demonstration of slippage.

1 nm Radiation Wavelength

In Figure 4.1a, the FEL pulse energy is amplified within the undulator until it reaches about 10^{-3} J after passing through 10 undulator modules. The horizontal bars on the amplification curve represent the intersections between each undulator module where no energy amplification occurs.

Figure 4.1b shows the normalised FEL power. The left side of the figure is green-dominated, conveying the relative insignificance of the FEL pulse compared to the background noise. From z = 10 m, the background colour shifts to a bluer hue, indicating the exit from the lethargy regime of the FEL process. Figure 4.1c shows the whole FEL power data at five different z-positions. These five positions correspond to the red dashed line on the gain curve and the 2D power plot. The FEL spikes are formed and randomly positioned on the beam. Besides, the spikes move towards the head of the beam, i.e. the larger time axis, as z increases.

In terms of the time axis, light moves faster than electrons and should arrive earlier, resulting in a smaller time axis. However, in this case, time is the output of Genesis, where it is transformed to $s - ct$. The s-coordinate is then normalized to show the length scale in time units, which is a practical measure.
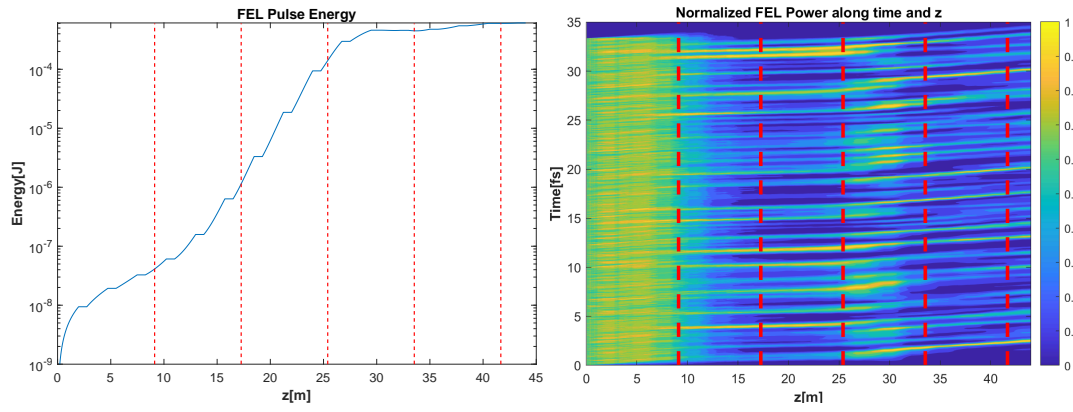
(a) FEL pulses energy along the z-axis

(b) FEL power along the z-axis and time axes.
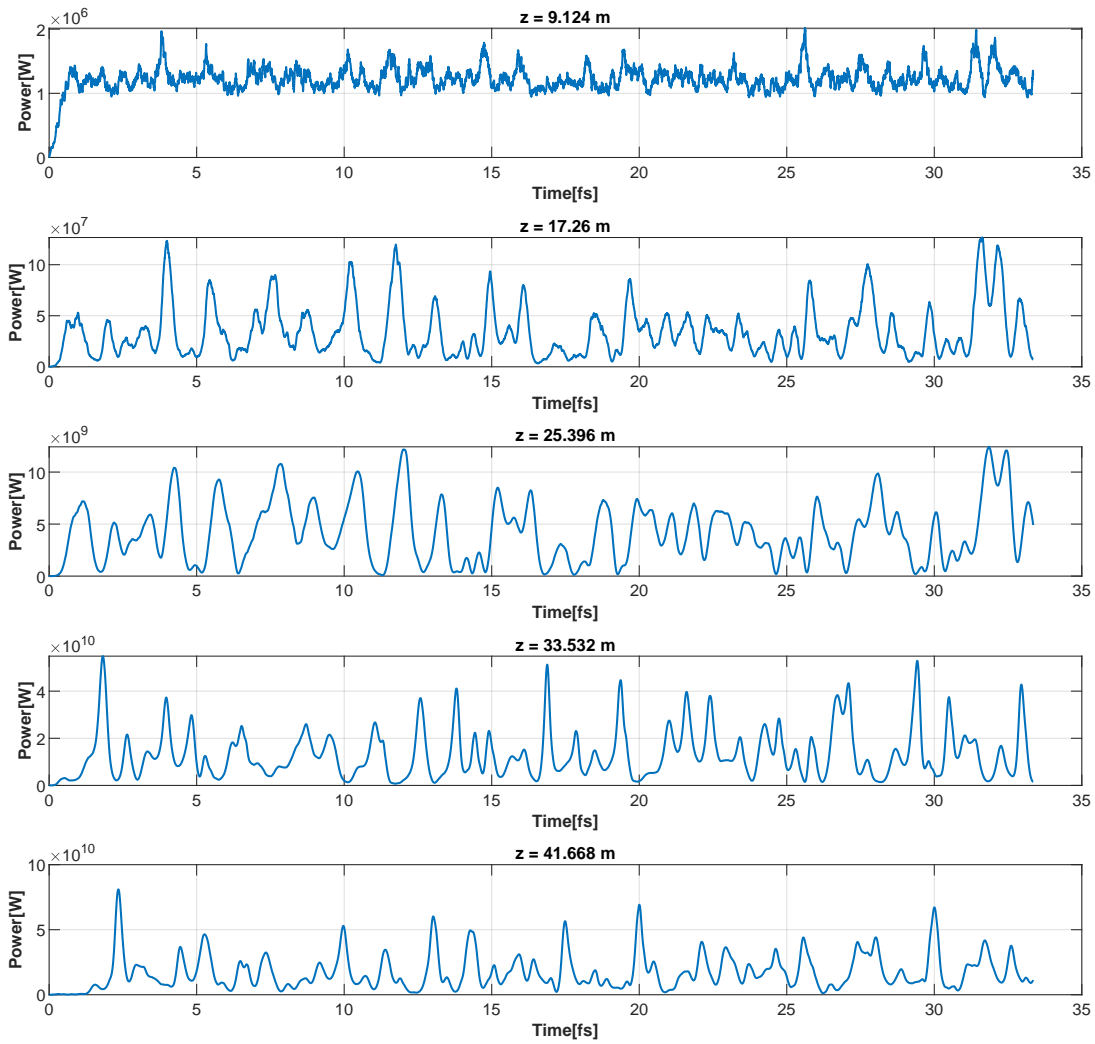
(c) The power at different z positions.

Figure 4.1: SASE Simulation results for $\lambda_r = 1$ nm.

4nm Radiation Wavelength

The second set of simulation results for the SASE refers to λ_r = 4 nm. In Figure 4.2a, only 6 undulator modules are necessary to achieve saturation energy of approximately 10^{-3} J, resulting in a significantly faster FEL process. In Figure 4.2b, the lethargy regime spans about 2 undulator modules. After saturation, the tendency of the FEL peaks to drift towards the beam head becomes even more apparent compared to in λ_r = 1 nm. In Figure 4.2c, the SASE power are highly random spaced on the time axis.

4.1.5   Conclusion in SASE simulation

We present two typical SASE simulation results for λ_r = 1 nm and 4 nm. Although many spikes are produced, the spike duration and intensity are very random, which is an important characteristic of SASE. Furthermore, it is observed that at both frequencies, the SASE peaks undergo a significant shift towards the beam head due to the slippage effect. This effect is more pronounced after saturation, consistent with our calculations of slippage speed. The slippage effect is more pronounced when the electrons are completely out of resonance.

(a) FEL pulses energy along the z-axis.

(b) FEL power along the z-axis and time axes.
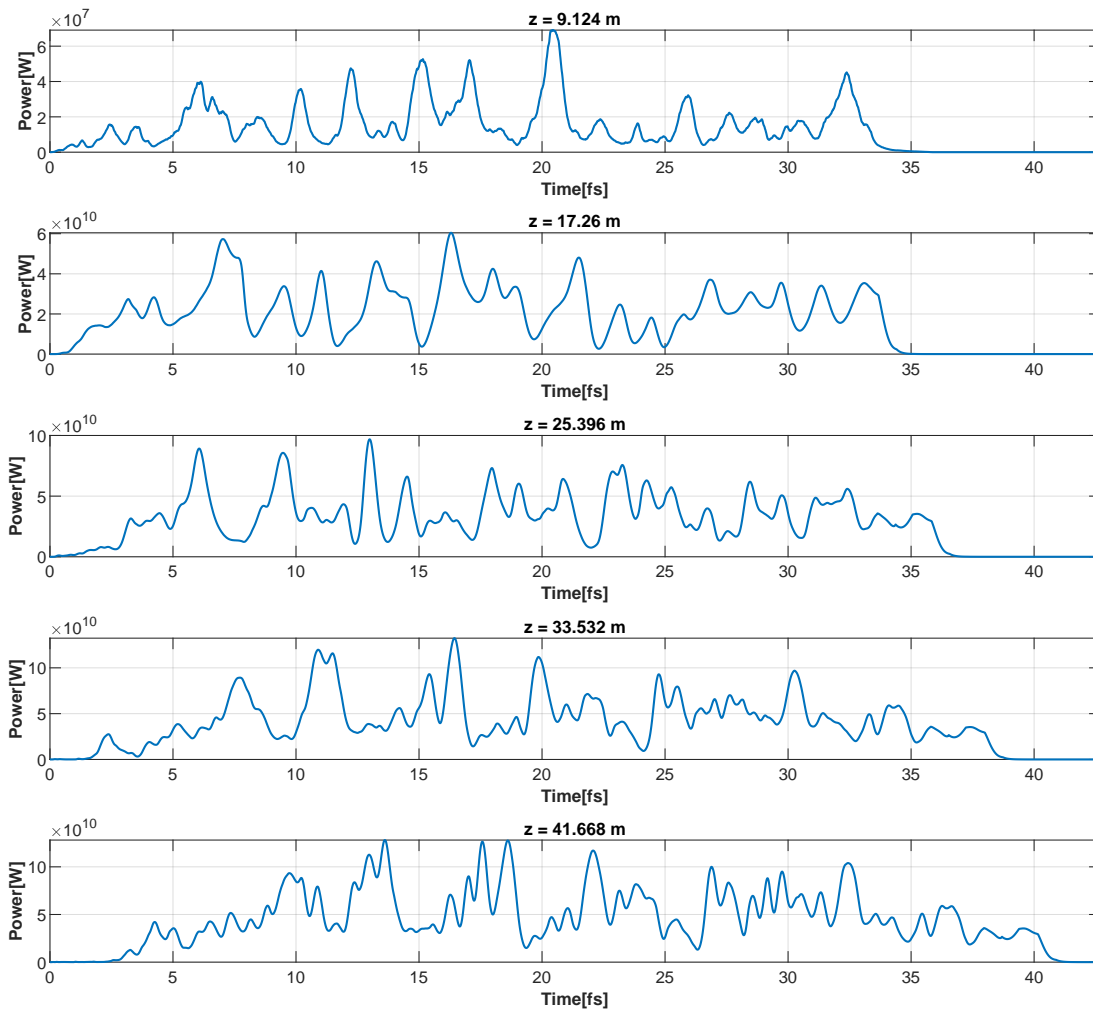
(c) The power at different z positions.

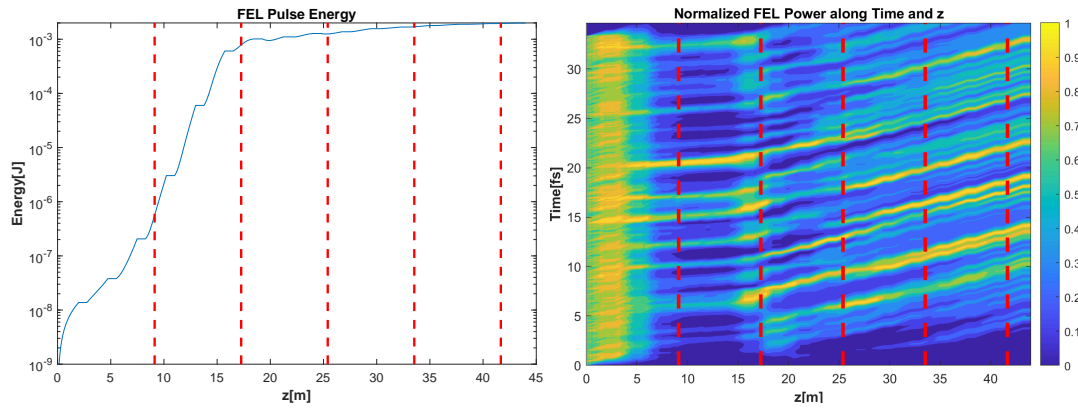Figure 4.2: SASE Simulation results for $\lambda_r = 4$ nm.

4.2 Enhanced SASE

Only the SASE method is not able to produce attosecond pulses at the soft x-ray range. In this section, we show the ESASE method, which is a candidate to produce it. However, at the end of the section, we conclude that ESASE alone is insufficient to mitigate the impact of slippage.

4.2.1 Energy Modulation with External Laser

The ESASE method requires energy modulation of the electron beam. This modulation arises from interaction with a high-power external laser beam, typically reaching up to 100 GW. This interaction occurs in a device called the modulator, which functions similarly to a wiggler and contains multiple magnetic periods [62]. We assume the laser beam has the form of a plan wave, that is :

$$E_L(z, t) = E_L(0) \sin[k_L(z - ct)] \tag{4.9}$$

$E_L(0)$ is the laser electric field before the interaction. In Chapter 2, we derived the electron's
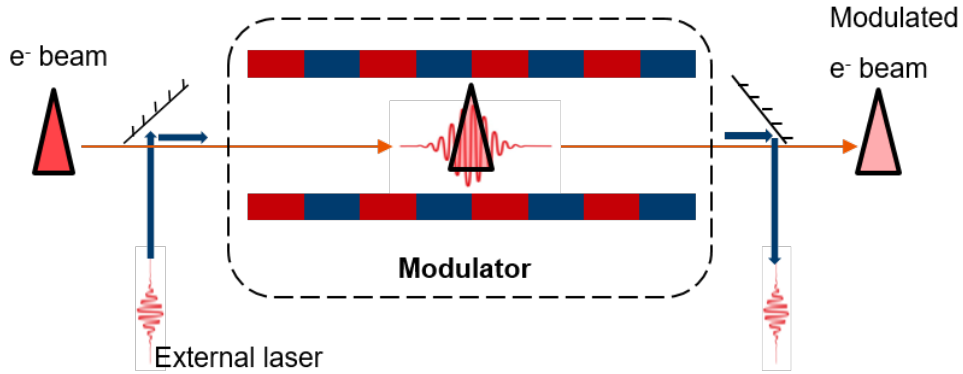
Figure 4.3: In Athos, a Ti:Sapphire laser at 800 nm was used as the seeding laser. The modulator is composed of 8 wiggler periods. The beam energy is modulated after interaction within the modulator.

energy changes in the presence of an external seeding laser:

$$\frac{d\gamma}{dz} = \frac{eKE_L(0)[JJ]}{2\gamma mc^2} \cos(k_L s/\overline{\beta}_z) \tag{4.10}$$

with the co-propagation coordinate $s = z - c\overline{\beta}_z t$. The resulting energy modulation is much smaller compared to the average beam energy. The energy change can be directly integrated over the undulator length and expressed in terms of the laser-beam power $P_L = \frac{cE_L(0)^2 w_0^2}{16\pi}$, where w_0 is the seeding laser waist. The energy change at the end of the undulator is then

given by [71]:

$$\Delta\gamma(s) = \sqrt{\frac{P_L}{P_0}} \frac{2KL_u[JJ]}{\gamma w_0} \cos(k_L s), \tag{4.11}$$

where $P_0 = \frac{I_A mc^2}{e} \approx 8.7\,\text{GW}$, and $I_A = \frac{mc^3}{e} \approx 17\,\text{kA}$, which is identified as the Alfén current. One can observe that the period of energy modulation along s corresponds to that of the seeding laser.

4.2.2   Density Modulation with Magnetic Chicane

Beam manipulation in the longitudinal plane requires a dispersive element. For relativistic electrons with $\gamma \gg 1$, they move nearly at light speed. In a cold beam Ansatz with minimal energy spreads and space charge effects, the relative longitudinal velocities are so small that positions remain unchanged on a straight path. However, a dispersive element can guide different energy electrons along varied paths, allowing longitudinal adjustments.

The chicane, often made up of four dipole magnets, is the most commonly used element in accelerator physics for longitudinal dispersion, where lower energy particles take a longer, curved path while higher energy particles take a shorter path. The tail particles have more energy than the head particles. As they move through the chicane, the tail catches up with the head, compressing the bunch, provided the tail particles don't overtake [71].

Chicanes can be used to compress energy-chirped beams to achieve high peak currents. This compression is similar to a linear transformation: reducing bunch length while raising energy spread and peak current. Interaction between electron and laser in an undulator creates a sinusoidal modulation with both positive and negative chirp regions. After passing through an appropriately dispersive chicane, represented by $R_{56} = \partial s/\partial\eta$, a density modulation is formed.

4.2.3   ESASE simulations at Athos Undulator

In this section, we present the results of the ESASE simulation. Since the beam is density-modulated, the FEL efficiency at the current spikes is higher, therefore, generating short pulses is possible. However, ultimately, we conclude that the strong slippage effect makes it challenging to generate attosecond pulses.

Simulation setup

The beam center energy is 3.33 GeV, which corresponds to a gamma factor of 6653. The energy modulation amplitude is 1 percent. The length of the beam is 40000 nm, corresponding to a duration of 133.3 fs. The initial current of the beam is 3 kA. After laser manipulation and magnetic chicane, the peak current reaches 8 kA. The seeding laser has a wavelength of 800 nm, i.e. a period of 2.67 fs. The energy modulation has the same period as the laser, and it is

also 800 nm. For the undulator, aw = 1.153 (1 nm) and aw = 2.884 (4 nm), where aw = $K/\sqrt{2}$. There is no taper in the undulator. We present simulation results set for λ_r = 1 nm and 4 nm.

Table 4.2: Parameters for ESASE simulation

Parameter	Value
Beam Centre Energy	3.33 GeV
Energy Modulation Amplitude	1%
Beam Length	40000 nm
Initial Beam Current	3 kA
Peak Beam Current (post-compession)	8 kA
Beam Energy Spread	501 keV
Beam Emittance (x and y directions)	300 nm
Seeding Laser Wavelength	800 nm
Energy Modulation Period	800 nm

The beam in Figure 4.4 will be applied for both λ_r = 1 nm and 4 nm. Figures 4.4a and 4.4b show the current and energy profiles. The beam used in the simulation does not include the dispersion after the seeding process. When considering this dispersion, the beam energy will fluctuate slightly. However, this should not significantly affect the FEL process and is therefore not taken into account.

(a) Beam current.   (b) Beam energy.
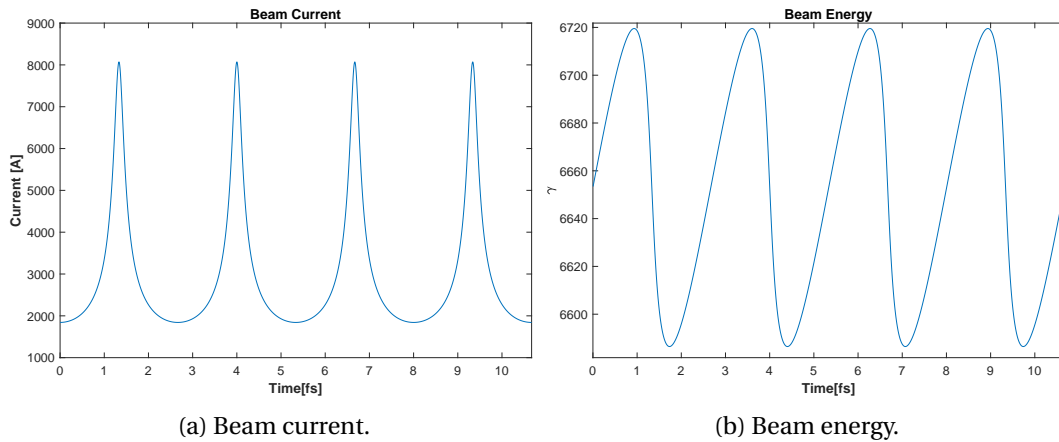
Figure 4.4: Beam energy and beam current for ESASE simulation.

In addition, this beam will be used again in Chapter 7, where we will combine multiple advanced configurations in Athos to generate short pulses (approximately 100 attoseconds) for a 4 nm radiation wavelength.
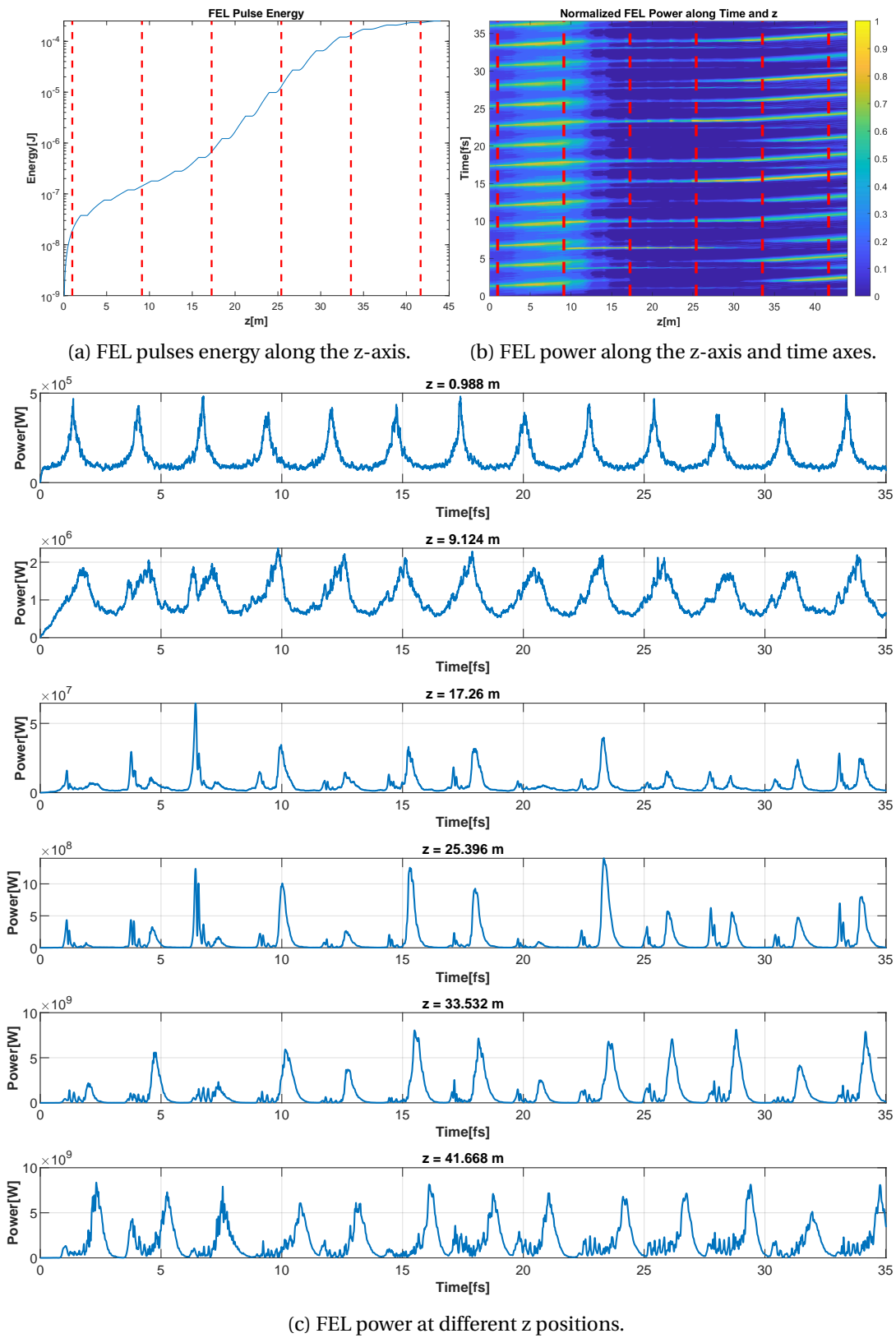
(a) FEL pulses energy along the z-axis.

(b) FEL power along the z-axis and time axes.

(c) FEL power at different z positions.

Figure 4.5: ESASE Simulation results for $\lambda_r = 1$ nm.

1 nm Radiation Wavelength

In Figure 4.5a, it takes about 12 modules to reach saturation, with a saturation energy of 200 μJ. Figure 4.5c shows the FEL power spikes at 6 different positions, corresponding to the 6 dashed red lines in figure 4.5b. There is a pulse train at the very beginning of the undulator. Each FEL spike is split into two spikes following the lethargy regime (z > 12 m). These two spikes in one cycle are located at the top and bottom of the energy modulation, where the rate of energy chirp is zero. At a position of z = 33.532 m, the FEL power spikes are located on the right side of the pair pulses (e.g., Time = 10 fs) and typically have a pulse duration of 500 attosecond FWHM.

4 nm Radiation Wavelength

From Figure 4.6a, it takes only 7 modules to reach saturation, with the saturation energy around 500 μJ. Figure 4.6c shows the power spikes of the FEL at six different locations, which align with the six dashed red lines depicted in figure 4.6b. The separate FEL pulse train is well generated at the beginning of the undulator. However, the fine structure of pulses is completely washed out with the slippage along the undulator.

4.3   Conclusion

In this chapter, we first discussed the slippage in the FEL process. Then, we presented the classical SASE simulations at two radiation wavelengths: $\lambda_r = 1$ nm and 4 nm. In Enhanced SASE, an increase in FEL power at the locations of current spikes was observed, which results in a shorter gain length. However, a pronounced slippage effect causes the electrons at current spikes to fall out of resonance, resulting in an extended duration of the FEL pulse. At $\lambda_r = 1$ nm, we obtained FEL spikes typically of 500 attoseconds FWHM duration. However, at $\lambda_r = 4$ nm, the fine structure of the spikes has been completely washed out due to strong slippage.

In addition, although ESASE offers a variety of input beam options, such as different peak currents, we present a single result in this chapter. The same beam parameters will be used in Chapter 7 to allow comparison. This comparison will highlight the significant reduction in pulse duration achievable with the configurations in Athos, which will be discussed in the following chapters. The chapters 5, 6 and 7 deal with optimisation at a wavelength of 1 nm. In Chapter 7 we will discuss the 4 nm case, where the strong slipping effect at this frequency requires the use of all the configurations presented in this thesis to achieve the short pulses in the 100 attosecond range.
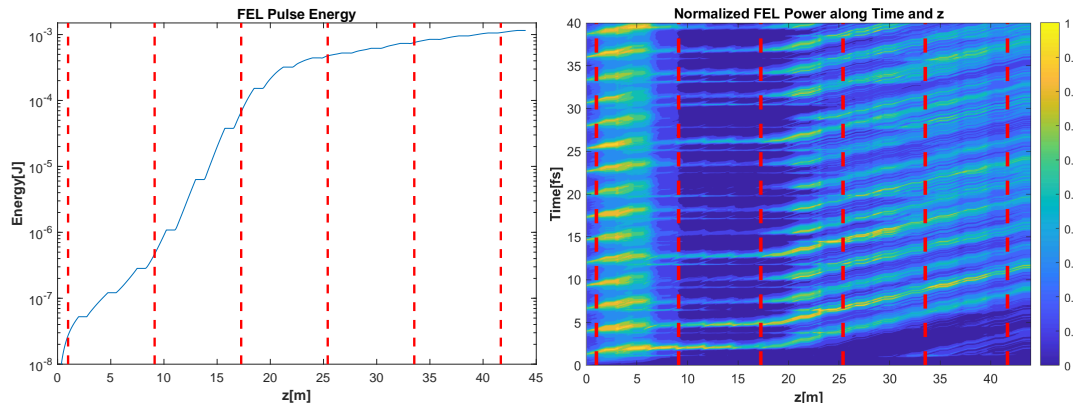
(a) FEL pulse energy along the z-axis.

(b) FEL power along the z-axis and time axes.
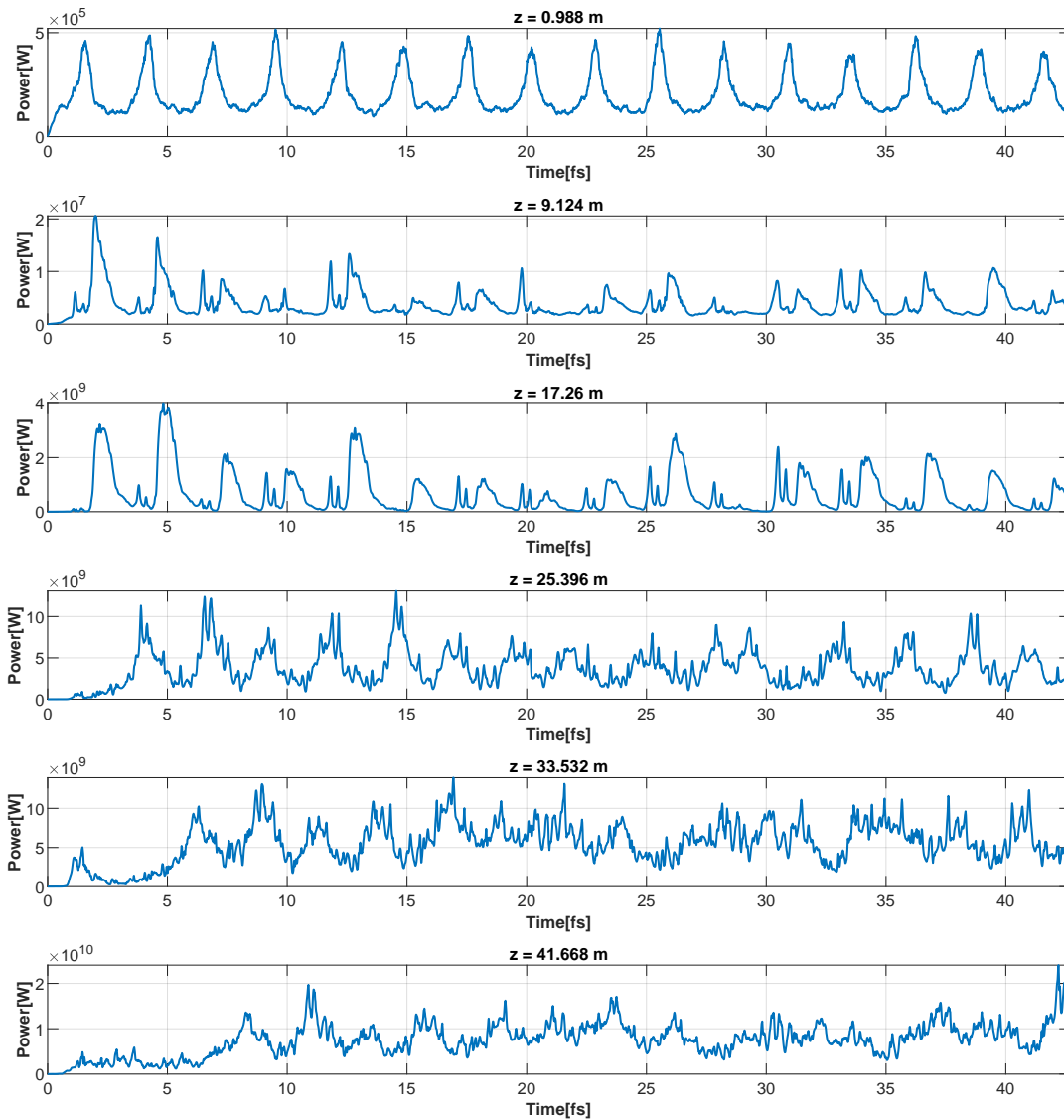
(c) FEL power at different z positions.

Figure 4.6: ESASE Simulation results for $\lambda_r = 4$ nm.

5 | Slicing Method: Chirp-Based Undulator Taper

In addition to the ESASE method, another approach to produce attosecond pulses involves applying an undulator taper to an uncompressed, energy-modulated beam. In the case of energy modulation with slippage, the FEL radiation fields slip towards the head of the beam. Meanwhile, the wavefront of the fields slips into different parts of the modulation where the energy of the interacting beam varies. We can estimate the energy change during slipping as the uncompressed beam maintains the same modulation shape as the seeding laser. By adjusting the undulator parameters, resonance can be maintained in the part of the beam where the FEL pulses are present. In contrast, the remaining parts may fall out of resonance, leading to degraded lasing. This method is called slicing and has also been explained in [61, 22]. It effectively reduces the impact of slippage, resulting in shorter FEL pulses. The simulation results show that the slicing method implemented in the Athos undulator setup produces spikes with an average duration of only 200 attoseconds. In addition, we have explored the application of a strong taper in the saturation regime.

5.1 Undulator Taper

This section discusses the general concept of the undulator taper, which is the basis for the chirp-based undulator taper. The undulator taper is originally intended to extract more energy from the electrons into radiation, especially when the FEL process is approaching saturation [72, 73, 74], where the changed electron energy violates the resonance condition, reducing efficiency and degrading the amplification process. The undulator taper aims to adjust the undulator parameters to maintain resonance for electrons of new energy. The formula for the varying electron energy to maintain a constant radiation frequency is given by:

$$\gamma_r^2(z) = \frac{\lambda_u}{2\lambda_r} \left[1 + \frac{K^2(z)}{2} \right], \tag{5.1}$$

where $K(z)$ represents the undulator parameter at position z. When electrons are in resonance, there is a resonant phase ϕ_r, which denotes the centre of the FEL oscillator phase, where the
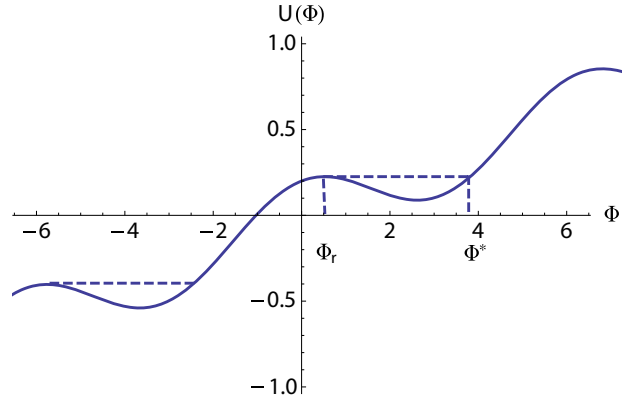
Figure 5.1: Potential with undulator taper [8].

collective energy change is zero. Since the FEL process approaches saturation, the majority of particles will have phases other than the resonant phase ϕ_r. To counteract the phase differences, another phase Φ_t is chosen to trap and slow down the maximum number of particles. This trapping phase is defined by the energy extraction rate. If there is no desired energy change, the trapping phase coincides with the resonance phase. Those particles close to the phase Φ_t experience deceleration at a nearly constant rate, particles further away from the phase do not experience deceleration. Suppose the resonant energy γ_r varies slowly along the z-axis and its variation over one undulator period is negligible. This implies that:

$$\frac{\lambda_u}{\gamma_r^2}\frac{d\gamma_r^2}{dz} \ll 1 \tag{5.2}$$

The pendulum equation for a single particle is modified as follows:

$$\frac{d\eta_j}{dz} = -\frac{eK}{m_e c^2 \gamma_0}E_0\left(\sin\phi_j - \sin\phi_r\right) \tag{5.3}$$

$$\frac{d\phi_j}{dz} = 2k_u\eta_j \tag{5.4}$$

Here, η_j represents the dimensionless energy offset of an electron, and ϕ_j represents the electron phase. The addition of a predefined phase item ϕ_r to the pendulum equations results in the modification of the system's Hamiltonian:

$$H_j = k_u\eta_j^2 - \frac{eK}{m_e c^2 \gamma_0}E_0\left(\cos\phi_j + \phi_j\sin\phi_r\right) \tag{5.5}$$

We define the potential item as $U(\phi_j)$, which is plotted in figure 5.1:

$$U(\phi_j) = \frac{eK}{m_e c^2 \gamma_0}E_0\left(\cos\phi_j + \phi_j\sin\phi_r\right) \tag{5.6}$$
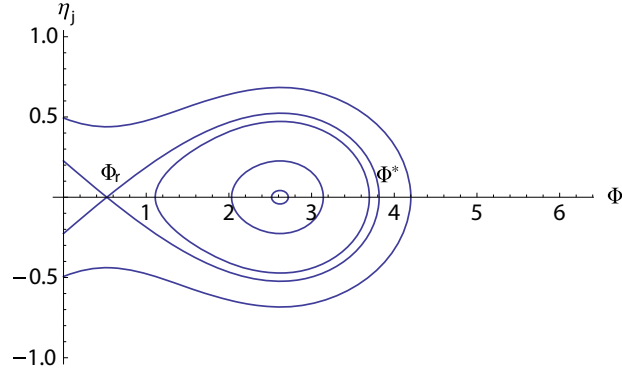
Figure 5.2: Phase space trajectory with undulator taper [8].

Note that in equation 5.6, there is E_0 as a parameter for the depth of the potential. If the term E_0 is too small, there is no real separatrix. As a result, the taper is generally applied around the saturation. In figure 5.1, a potential well can be observed between the phases of $\phi_j = \phi_r$ and $\phi_j = \phi^*$. This well will trap electrons between the two phases, and these electrons will participate in the oscillation. In figure 5.2, we present the phase space trajectory with taper. At two extreme points, the potential reaches its maximum and minimum within the range of (0, 2π). The intersection point on the right side of the semicircle is denoted by ϕ^*.

Electrons with $\eta_j < \eta_{\max}$ and $\phi_r < \phi_j < \phi^*$ demonstrate stable oscillations at the phase of $\pi - \phi_r$. The ideal value of the phase to extract the largest energy from the electrons lies between these two extremes, requiring fine-tuning of undulator parameters. The general taper concept will be directly applied in section 5.5, where the FEL process is in saturation regime.

5.2 Slicing: Energy-Modulated Beam With Undulator Taper

The slicing method is a chirp-based taper. The energy chirp introduced by energy modulation leads to a frequency chirp in the radiation. There are some references discussing the chirp-based taper [75, 76], but they are all based on slowly varying approximation.

The slicing method allows for the use of undulator taper in any regime of a FEL. In this method, the modulation amplitude is much larger than the SASE bandwidth, so the slowly varying approximation is no longer applicable. In [61], there is a discussion about the linear regime of this dynamic. The resonance wavelength is :

$$\lambda_r = \frac{\lambda_u}{2\gamma^2(z)} \left(1 + \frac{K^2(z)}{2} \right) \tag{5.7}$$

Since we have a well-defined energy modulation profile, we can make an estimation of the energy variation accompanying specific FEL pulses as they slide along the electron beam. The

undulator parameter is then calculated as follows:

$$K(z) = \sqrt{2\left(\frac{2\lambda_r \gamma^2(z)}{\lambda_u} - 1\right)} \tag{5.8}$$

This adjustment maintains the resonance condition at FEL spikes despite slippage. The method is illustrated in figure 5.3.
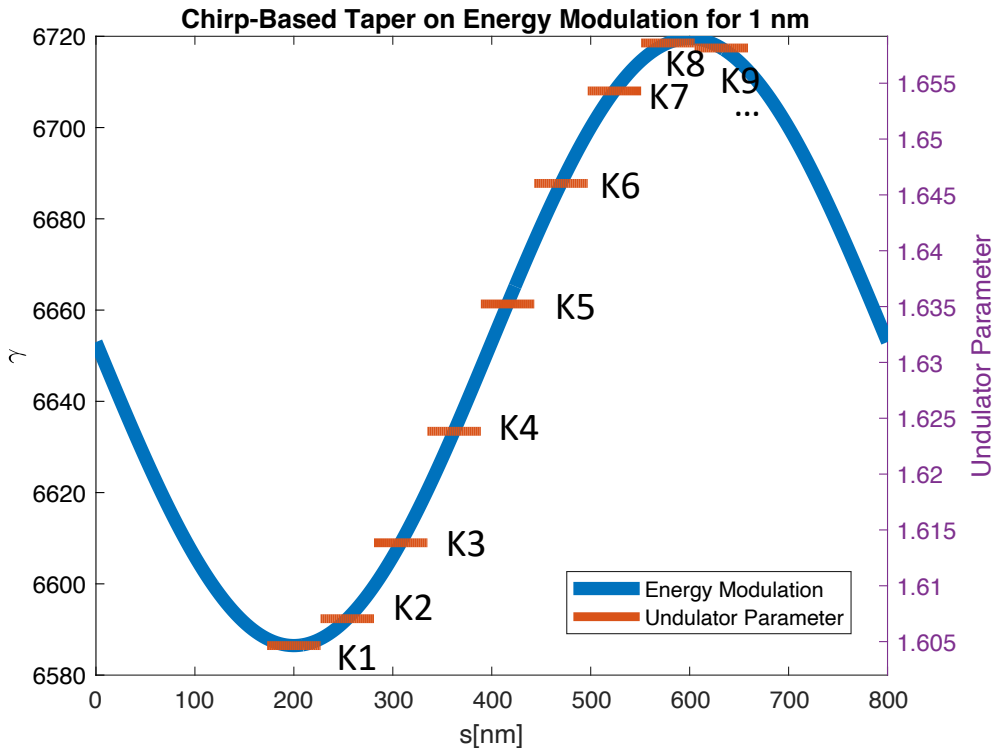
Figure 5.3: Undulator taper profile for slicing method. The term "K1" refers to the undulator parameter in the first module, "K2" in the second, and so on. The slippage in one module is about 55 nm, calculated by adding 52 nm to an additional 3 nm for the slippage in the intermodule. This model does not include the dispersion introduced by seeding.

In addition to conducting simulations for the delivery of short pulses, we propose that there may be an intermediate regime between the lethargic and linear regimes in slicing dynamics, based on our study, namely:
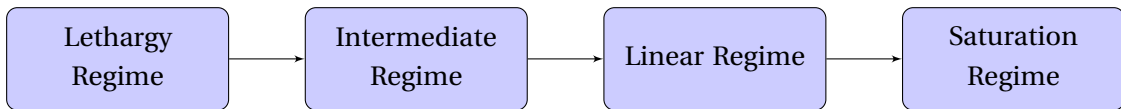
In this intermediate regime, the power of the FEL is not fully amplified. The formation of two bunching spikes is observed when the constant taper direction is maintained. The two bunching peaks mentioned above are found on the same chirp, whether it's a negative chirp

for a negative taper or a positive chirp for a positive taper. The regime ends up with the direction change of the taper. The generated bunching spike, which is already at the extreme of the modulation, begins to slide on the beam following the new taper direction, from where the dynamic is the same as in figure 5.3. The complete showcase can be found in figure 5.13 accompanied by the simulation results and will be presented in section 5.4.2.

5.3 Simulation Setup

Simulations are required to determine the strategy for finding the optimal solution. In certain simplified cases, such as the undulator taper discussed earlier, it is possible to establish upper and lower bounds. However, the exact location of the optimal point in the full dynamics remains unclear. In this section, we show the simulation setup for the slicing method, and how to find the best taper parameters.

5.3.1 Beam Definition

The electron beam displays energy modulation with an 800 nm period. The beam duration is 40000 nm, corresponding to 133.3 fs in the time axis. The centre energy of the beam is denoted by $\gamma = 6653$, while its modulation amplitude is 1%, corresponding to a maximum variation of $\Delta\gamma_{max/min} = \pm66.53$. The beam's energy spread is 501 keV, amounting to only 0.017% of the entire beam energy. This value is significantly smaller than the bandwidth, which ranges from 0.05% to 0.1%. Thus, the initial energy spread has a negligible impact when considering efficiency.

Table 5.1: Simulation Parameters for the Slicing Method.

Parameter	Value
Beam Centre Energy	3.33 GeV
Modulation Amplitude	1% ($\Delta\gamma_{max/min} = \pm66.53$)
Beam Length	40000 nm
Initial Beam Current	3 kA
Beam Energy Spread	501 keV
Beam Emittance (x and y directions)	300 nm
Seeding Laser Wavelength	800 nm
Energy Modulation Period	800 nm

5.3.2 Undulator Parameter Setup

Building upon the idea of slicing, we set up the taper profile. The simplest fitting method is to assume that the period of the taper profile coincides with the modulation of the electron

beam, e.g.,

$$K(z) \sim \Delta\gamma(s) \sim \cos(k_L s), \qquad s(z) = \frac{\lambda_r}{\lambda_u} z, \tag{5.9}$$

with $\Delta\gamma(s)$ the energy change after modulation, k_L the wave number of the seeding laser and s the coordinate in the electron beam. Equation (5.9) shows that the starting point is considered at the bottom of the beam energy modulation due to the dependence on $\cos(k_L s)$.

In the case of full resonance, the slippage velocity is one-third of that of full non-resonance (see equation 4.8). The real value for the actual model should be somewhere in between. Based on the analysis of velocity disparities, it is probable that the taper profile requires a larger period than the energy modulation. To determine the optimal simulation setup, we scanned a range of taper periods, corresponding to the energy modulation between 750 nm and 1130 nm. A total of 39 sets were investigated, with varying step sizes for each simulation. The energy modulation is at 800 nm, but we use different taper periods to search for better performance assuming a slippage velocity other than one radiation wavelength per undulator period. We did not extensively explore periods less than 800 nm due to their poorer duration performance.

The amplitude of the taper is also an important factor to consider. We have chosen different amplitudes ranging from 0.8 % to 3 %, giving a total of 11 data sets (the step is not the same for each simulation). The taper amplitude is consistently 1%, but we explore different taper profiles corresponding different amplitude to improve performance. Additionally, we conducted a partial cross-scan to examine scenarios with varying combinations of period and amplitude to determine the optimal setup.

5.4   Simulation Result and Analysis

5.4.1   Simulation Result

We have scanned the undulator parameter in the taper setup for both period and amplitude. The comparison between different amplitudes is in figure 5.4. The decision is to keep 1 % since it has a good energy performance.

For the taper periods, we show the comparison between 800 nm and 980 nm in Figure 5.5. At z = 37.91 m (indicated in the figure by black dots), the pulse duration for Taper 1 is 266.3 as. For Taper 2, it is 207.6 attoseconds. Consequently, the decision was made to adopt 980 nm as the taper period.
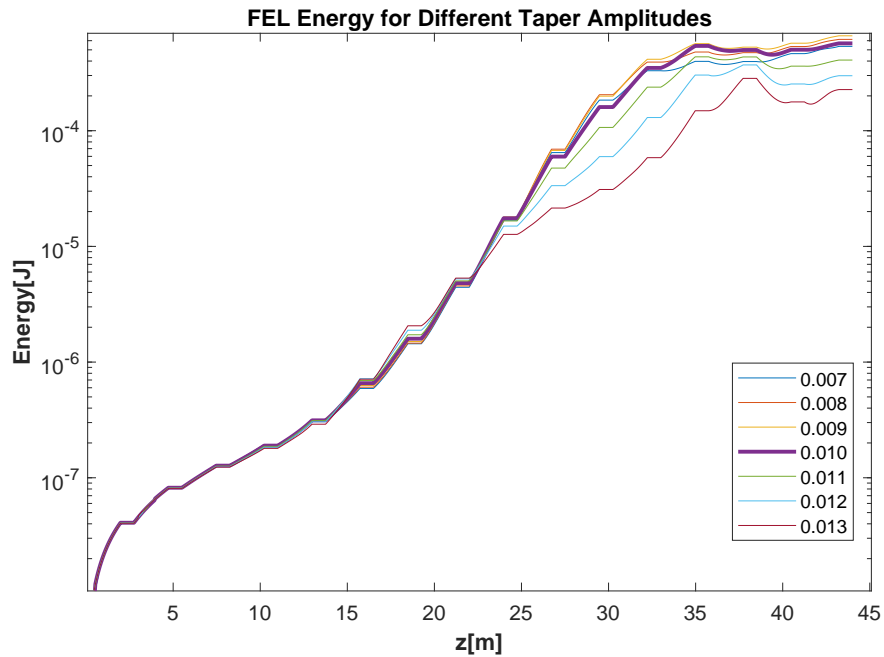
Figure 5.4: FEL energy for different taper amplitudes, where $K(z)$ corresponds to the energy chirp variation. The numbers in the legend indicate the reference amplitude of the energy modulation used to calculate the corresponding undulator parameter. The result with 0.010 (amplitude 1% of energy modulation, bold purple line) has a good pulse energy performance compared to other cases.
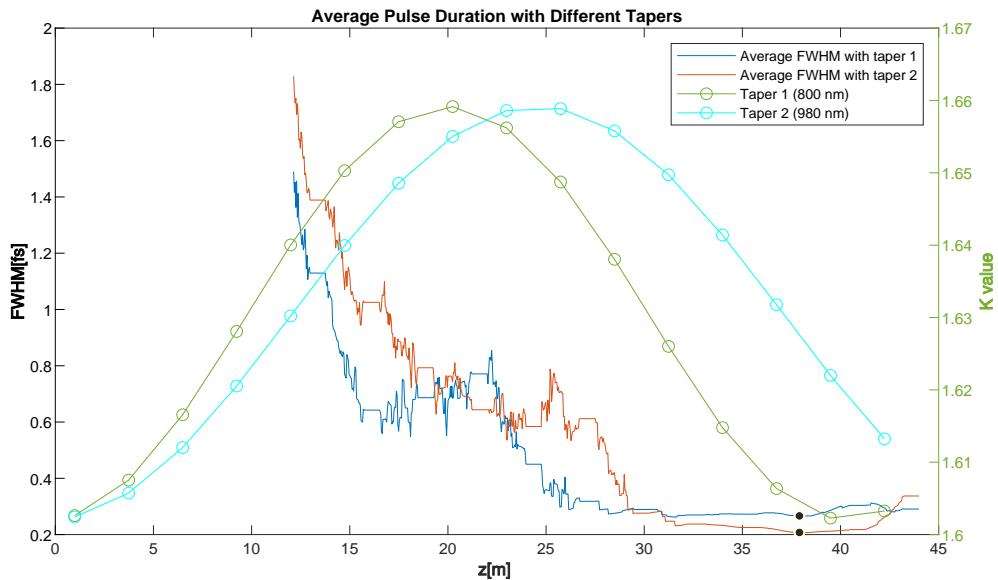
Figure 5.5: The average FWHM pulse duration for Taper 1 (800 nm period) and Taper 2 (980 nm period) are shown by blue and red curves, respectively, with Taper 2 reaching 207.6 attoseconds at 37.91 m, compared to Taper 1's 266.3 attoseconds.

In the end, the taper profile is:

$$K(z) = \sqrt{2\left(\frac{2\lambda_r\left(\gamma_0(1 + 0.01 \times \sin(\frac{s(z)}{980} \times 2\pi))\right)^2}{\lambda_u} - 1\right)}, \qquad s(z) = \frac{\lambda_r}{\lambda_u}z \qquad (5.10)$$

where s is the coordinate in the beam.

Following this setup, we present the results of the simulation. The simulation results include several figures:

1.Gain curve.
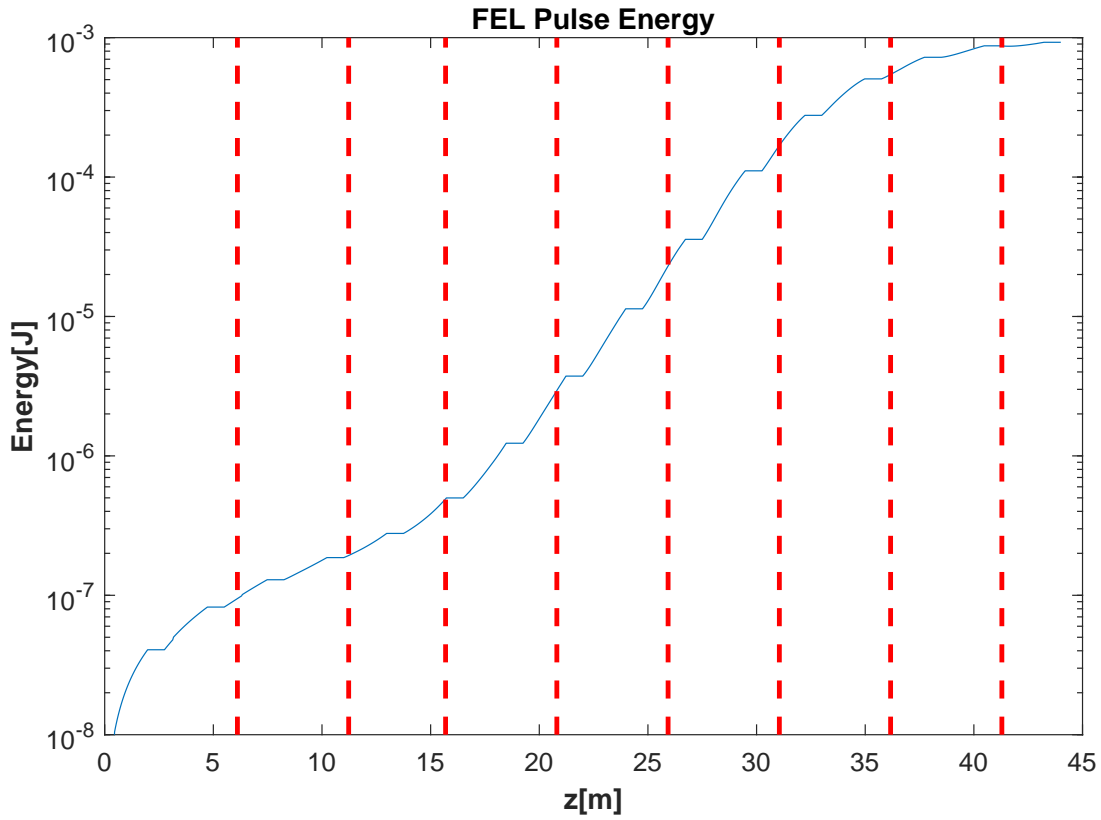
Figure 5.6: The FEL pulses energy along the z-axis. We use the taper profile corresponding to an energy modulation amplitude of 1% and a taper period of 980 nm. The pulse duration is calculated by integrating the FEL power along the z-position. The red lines are selected positions where the pulse structure is shown in figure 5.8.

In Figure 5.6, saturation is reached after 13 modules. The saturation energy is approximately 1 millijoule.

2. Normalised FEL power along the z-axis and the time axis.
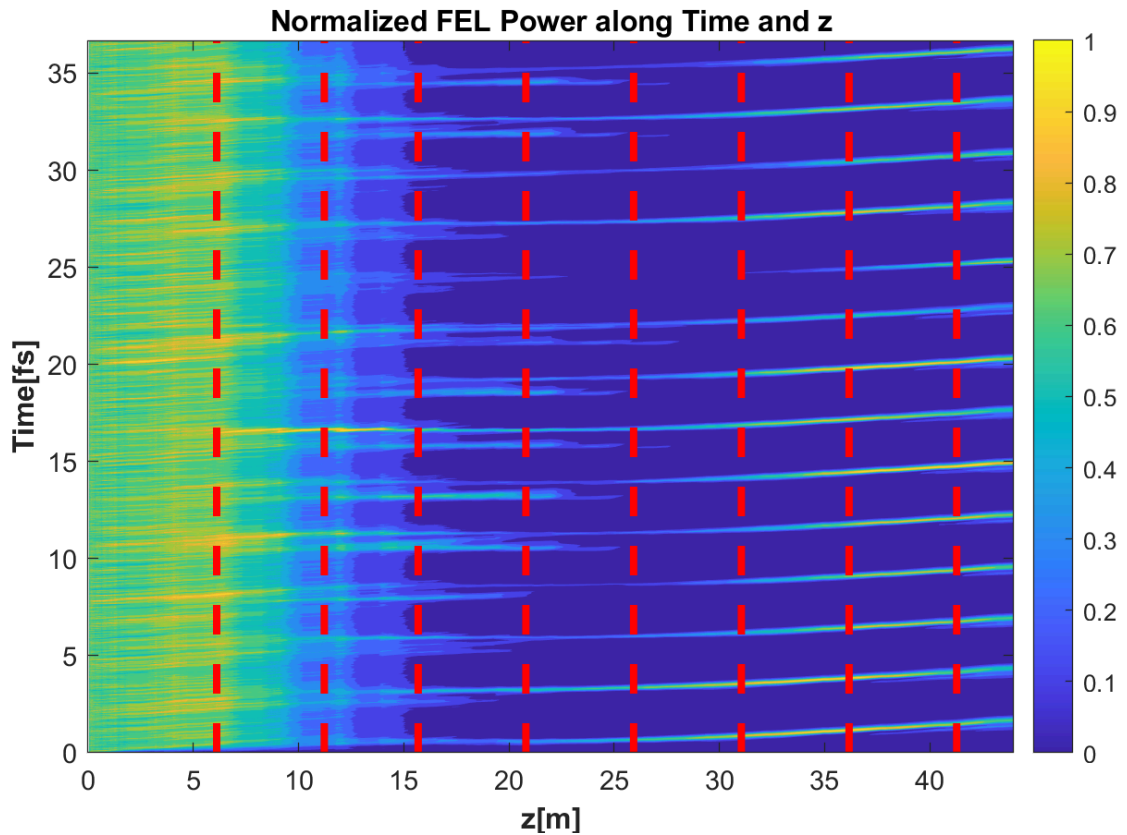
Figure 5.7: Normalised FEL Power along the time axis and the z-axis, with normalisation applied for each z coordinate. The red lines represent the selected positions in figure 5.8.

The initial position on the left shows uniform FEL power with many transverse modes, resulting in minimal fluctuation in the radiation power. This consistency is shown by the color coding, where the green color corresponds to the average power due to the choice of colour ramp. As the FEL pulse power increases along the z-axis, the background gradually darkens after normalisation.

As for the s-coordinate (time coordinate), we select a portion of the beam (time = 0 fs to 33.3 fs) to display, which is the same as in chapter 4. No discernible pulses are observed in the range from z = 0 m to z = 10 m. Between 15 and 25 m, we observe the generation of multiple pulses, typically two in number, for most cycles. After z = 25 m, there is only one pulse in each cycle, which increases in amplitude until it reaches saturation. The reason will be discussed in figure 5.14 in the analysis section.

3. Typical pulse structures at different z positions.

Figure 5.8 shows the power profile at selected z-positions. The data is not normalised, therefore the value of power can be read. At z = 41 m, the typical saturation power is around 100 gigawatts.

Figure 5.8: The structure of pulses varies at different z positions. It is important to note that there are typically two FEL spikes in one modulation cycle before z = 25 m. The selected positions are indicated by red lines in figure 5.6 and figure 5.7.
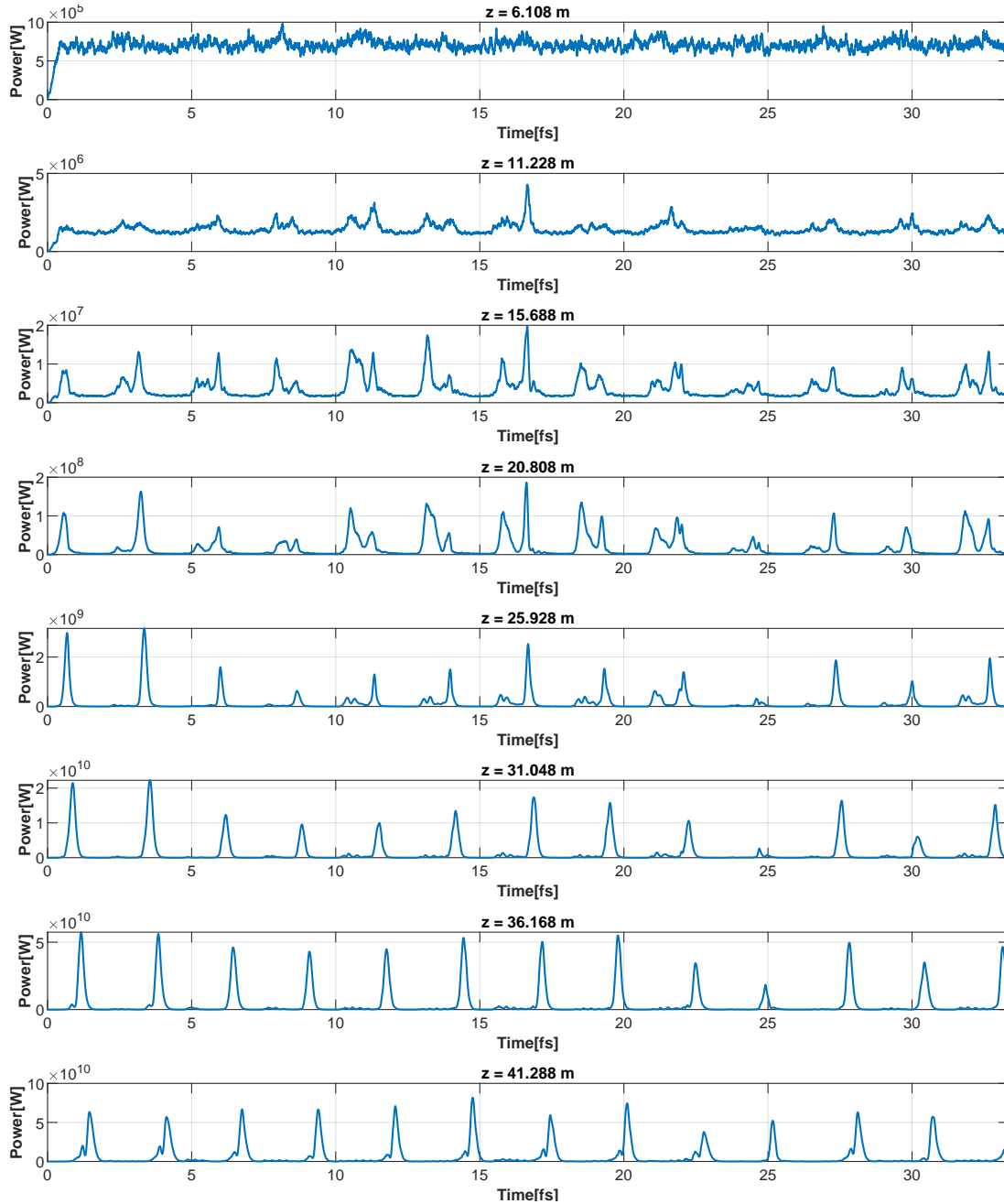
4. Average pulse duration along the z-axis, with error bars.
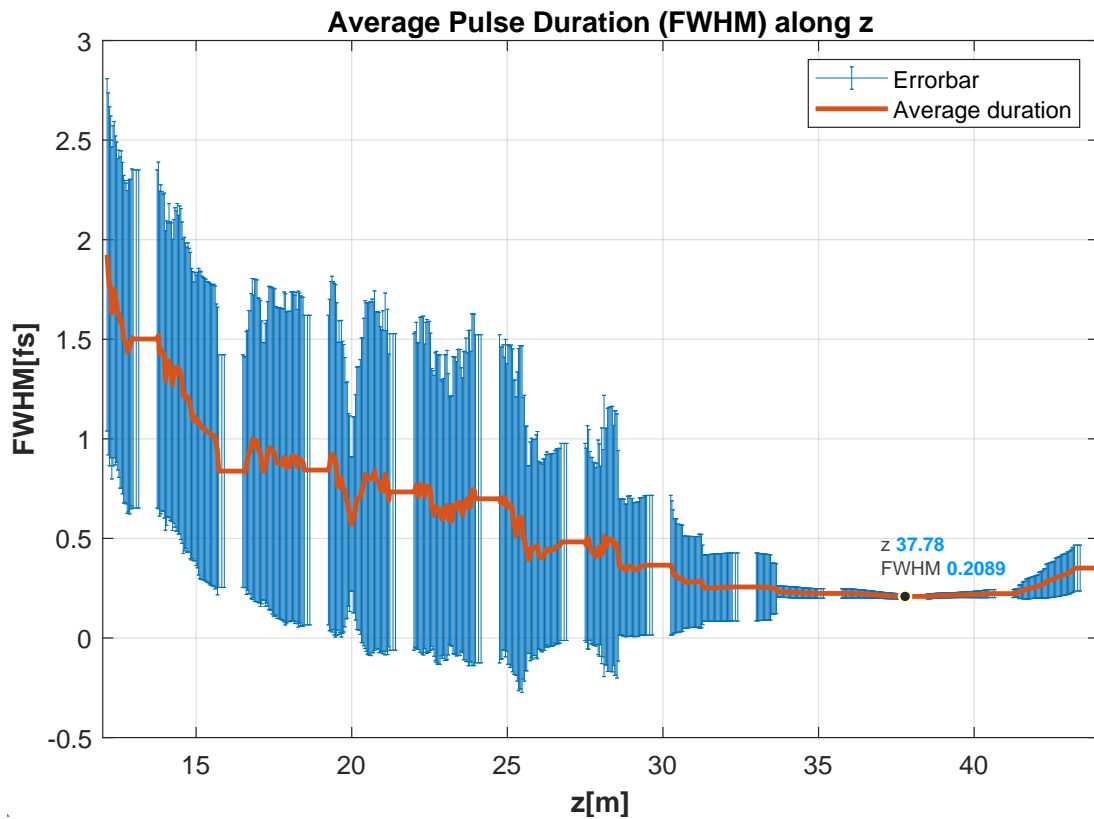
Figure 5.9: Average pulse duration in figure 5.7. The red curve represents the average Full Width at Half Maximum (FWHM) duration, while the blue colour indicates the error bars.

We measure the pulse duration in Figure 5.7 and plot the result in figure 5.9.

The measurement approach is direct. The peak is first detected, followed by locating the left half-maximum within a 400 nm range. Subsequently, the right half-maximum is searched for to determine the duration. This approach accurately reflects the typical fluctuation range, especially in cases involving multiple pulses. The results would be less representative if only the largest pulses were selected, and measurements were confined to their fluctuation. However, the first method is more effective when the goal is to identify one peak per cycle.

The measurements start at a distance of $z = 12$ m. The average duration shows a continuous decrease along the z-axis. At around 33 metres, the average bandwidth displays a small error bar, which is generated by MATLAB's 'errorbar' function and can produce both positive and negative values depending on the variation. The duration at the end of the 14th module is 208.9 attoseconds.

The average duration results are robust. We obtained these results from 50 cycles, each with random shot noise. Therefore, the results remain consistent even when the seed of the random number generator for the shot noise calculation in the simulation is varied.

5. FEL power as a function of radiation wavelength and z
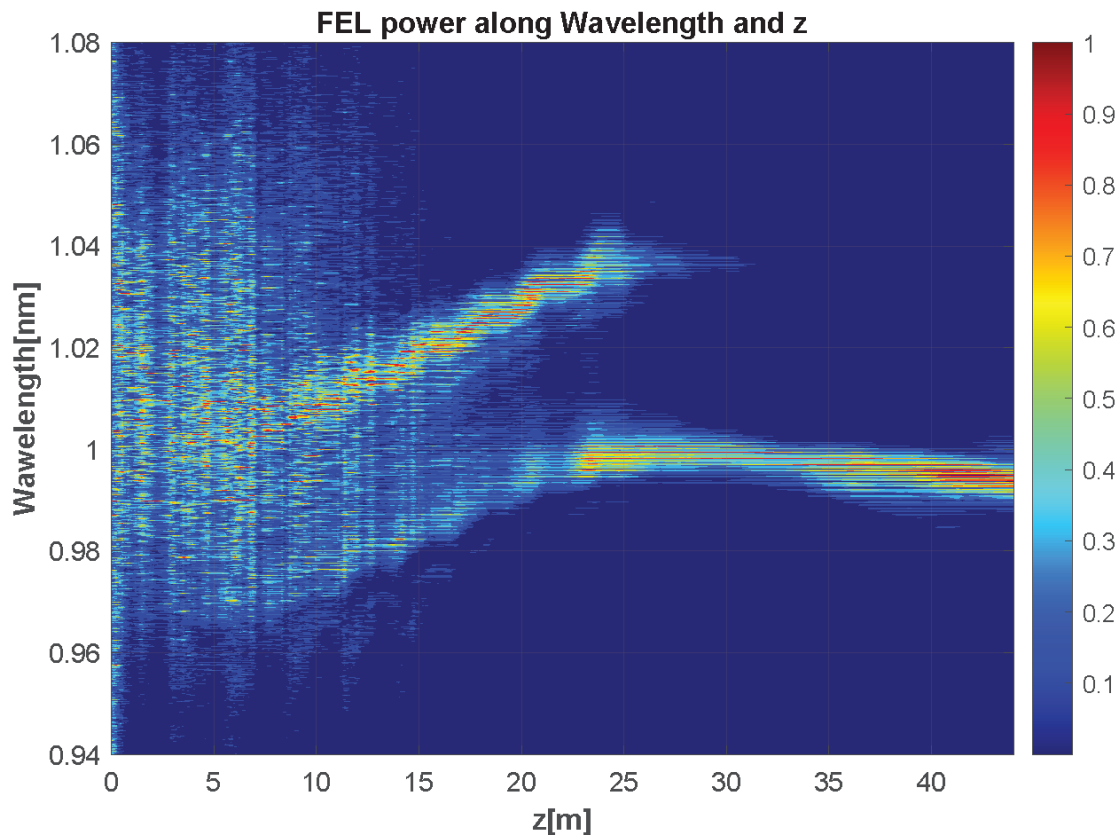
Figure 5.10: FEL power along z and wavelength[I]. The spectrum is obtained by applying the Fast Fourier Transform and then a Fast Fourier Transform shift on the signal. The key finding is the presence of two colors between z = 5 m and 25 m, and one color from z = 25 m to the end.

In figure 5.10, between z = 0 and z = 10 m, the range of wavelengths is particularly wide; From z = 10 m to 25 m, two optical beams with a spacing of 0.04 nm coexist, and they redshift at the same rate along the z-axis. The spike with a larger wavelength is more intense than the other. From z = 25 m, the direction of the taper changes from positive to negative, and the spectrum displays only one color while the other vanishes.

[I]For a clearer illustration, the reader is referred to the PDF version, which is clearer than the printed version.

6. Electron energy after each undulator module along the time axis.

(a) Electron energy after each module.

(b) Energy variation after each module.
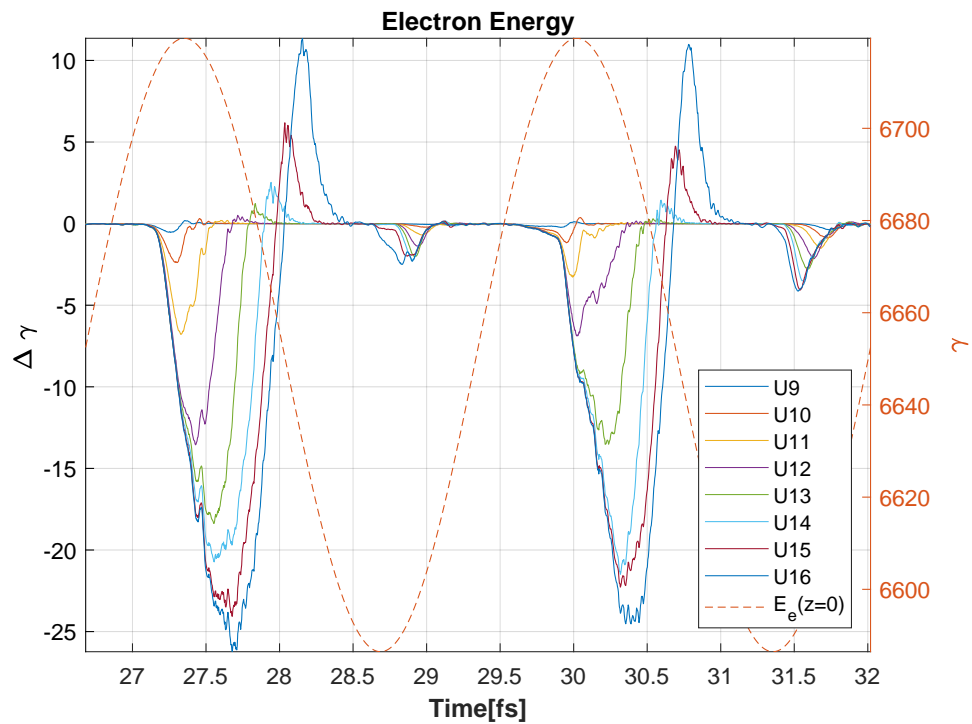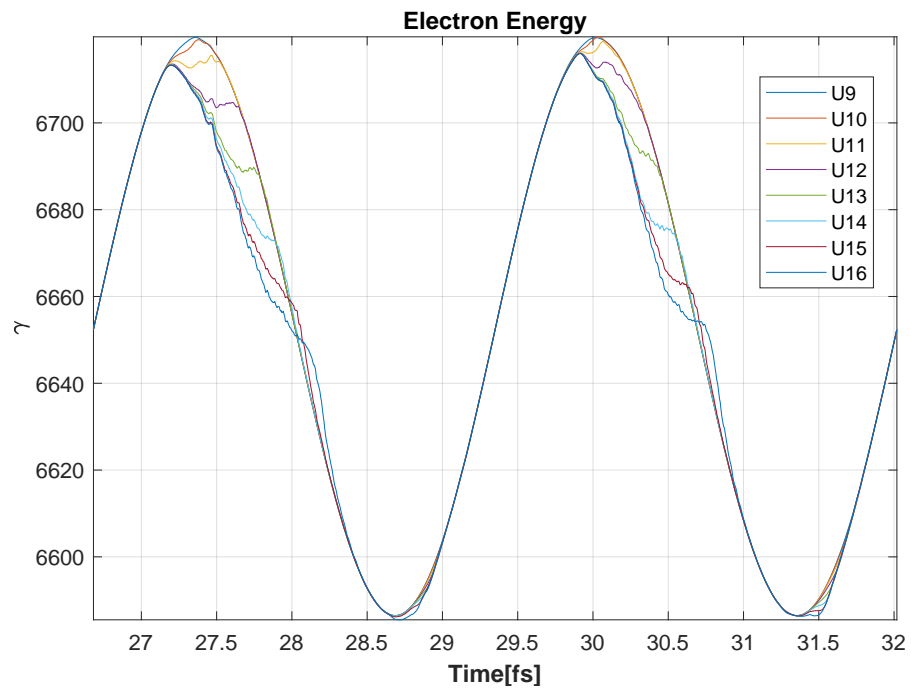
Figure 5.11: Electron energy (a) and its variation (b) after each undulator module. (More caption is available on the next page.)

Figure 5.11. The main result is the resonant beam shift in different modules with the presence of an undulator taper. The abbreviation 'U9' in the legend refers to the end of module 9, and so on. A dashed orange line in figure 5.11b indicates the initial energy, which makes it easier to find the top and bottom of energy modulation.

The energy difference is only plotted after the ninth undulator module due to the lack of normalization. It is observed that there is a significant loss of beam energy after this module. The resonant beam position shifts with the undulator taper for the beam at the top of the energy modulation. Additionally, there is minor energy loss at the bottom of the modulation. In figure 5.11b, the beam at the top of the modulation loses energy from its right edge, while the beam at the bottom of the modulation lose energy from their left edge. Since they are in opposite directions, the generated FEL pulses are approaching during the FEL process.

In U15 and U16 of figure 5.11b, electrons absorb energy from photons, which is not desired. To optimize this energy absorption, we will apply a significant taper, and the optimized results are presented in figure 5.17 of Section 5.5.

7. Bunching at different positions.

Figure 5.12 presents the bunching at different positions corresponding to the red lines in Figures 5.6 and 5.7. From z = 31 m, the bunching spikes stop growing at around 0.7, indicating the saturation. We see in most cycles, two bunching spikes are formed. After z = 25 m, the taper direction was changed, causing the bunching spike at the right side in one modulation cycle to shift to the right side, while the spike at the left side continued to shift to the left.

Figure 5.12: Bunching at different positions corresponding to the red lines in Figures 5.6 and 5.7.
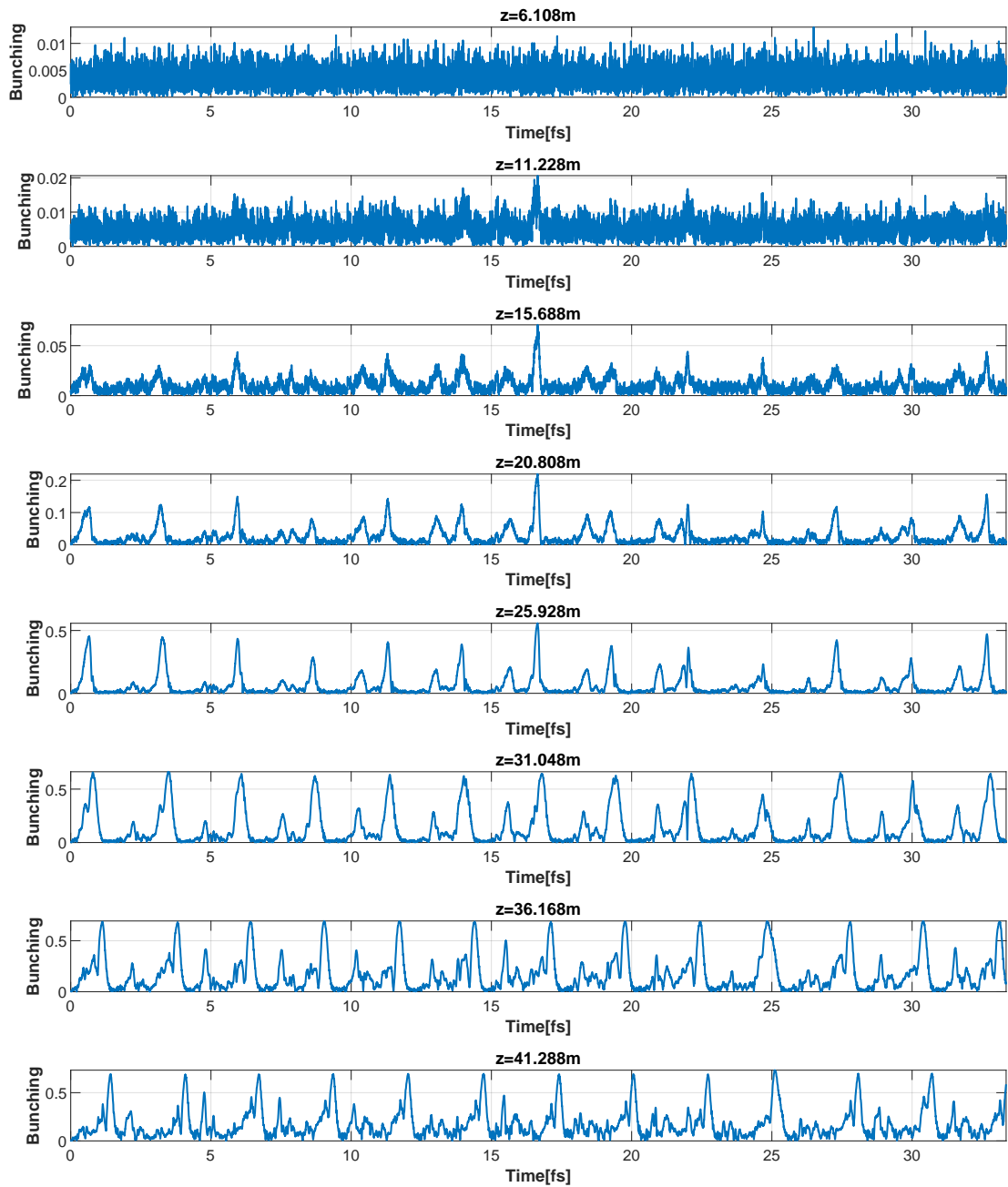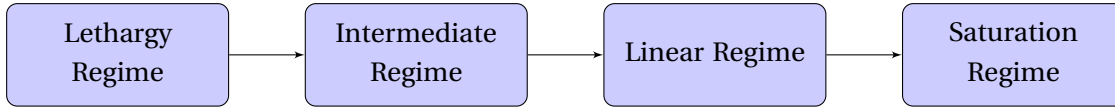
5.4.2 Simulation Result Analysis

In this analysis subsection, we will refer to the simulation results from the previous section. The whole FEL process is divided into four parts.

| Lethargy Regime | → | Intermediate Regime | → | Linear Regime | → | Saturation Regime |

A) Lethargy Regime (z = 0 - 10m)

In a high-gain FEL, the intensity growth of the FEL pulses is slow within the initial 2-3 undulator gain lengths. This regime is referred to as the lethargy regime. In the slicing method, the collective coupling strength between electrons and radiation is lower due to the presence of the undulator taper, which introduces extra frequency detuning. As a result, a longer distance has been observed in the lethargy regime compared to SASE, approximately 4 undulator modules (refer to Figure 5.6). The bunching in this regime (z = 6.108 m in Figure 5.12) has almost no spike shape; the FEL pulses at the same position in Figure 5.8 begin to exhibit a vague pulse shape, but almost the whole bunch is lasing. The taper within this region appears to have no effect on the selection of beam portions for lasing.

B) Intermediate Regime (z = 10m - 23m)

After the lethargy regime, the amplification process does not immediately transition to exponential growth. Instead, it first enters an intermediate state that intervenes between the two.

This period is named the "intermediate regime," as bunching factor spikes are generated during this stage. Figure 5.13 shows the bunching factor at different z-positions. Since the taper is always positive in this regime in the simulation, all the bunching in the negative chirp is suppressed compared to the positive chirp. There are two bunching spikes formed on the positive chirps, which correspond to the two frequencies in the spectrum (Figure 5.10) in this regime. According to the results in the spectrum, two spikes are radiating at shifting frequencies due to the presence of the taper, though not shifted significantly in Figure 5.13. The formation of the two bunching spikes is not fully understood and requires further investigation.

The effect of the taper differs from what is typically discussed in a general taper scenario. Here, there are no strong radiation pulses or significant electron bunching. Therefore, the taper analysis can not be based on the electron bucket, as the bucket contains few electrons. The effect of the taper can be attributed to the instability induced by the detuning parameter. The positive taper slope at the upper ends of the energy modulation results in a certain amount of energy being absorbed from the radiated pulses and converted into electrons, thereby increasing the bunching factor.
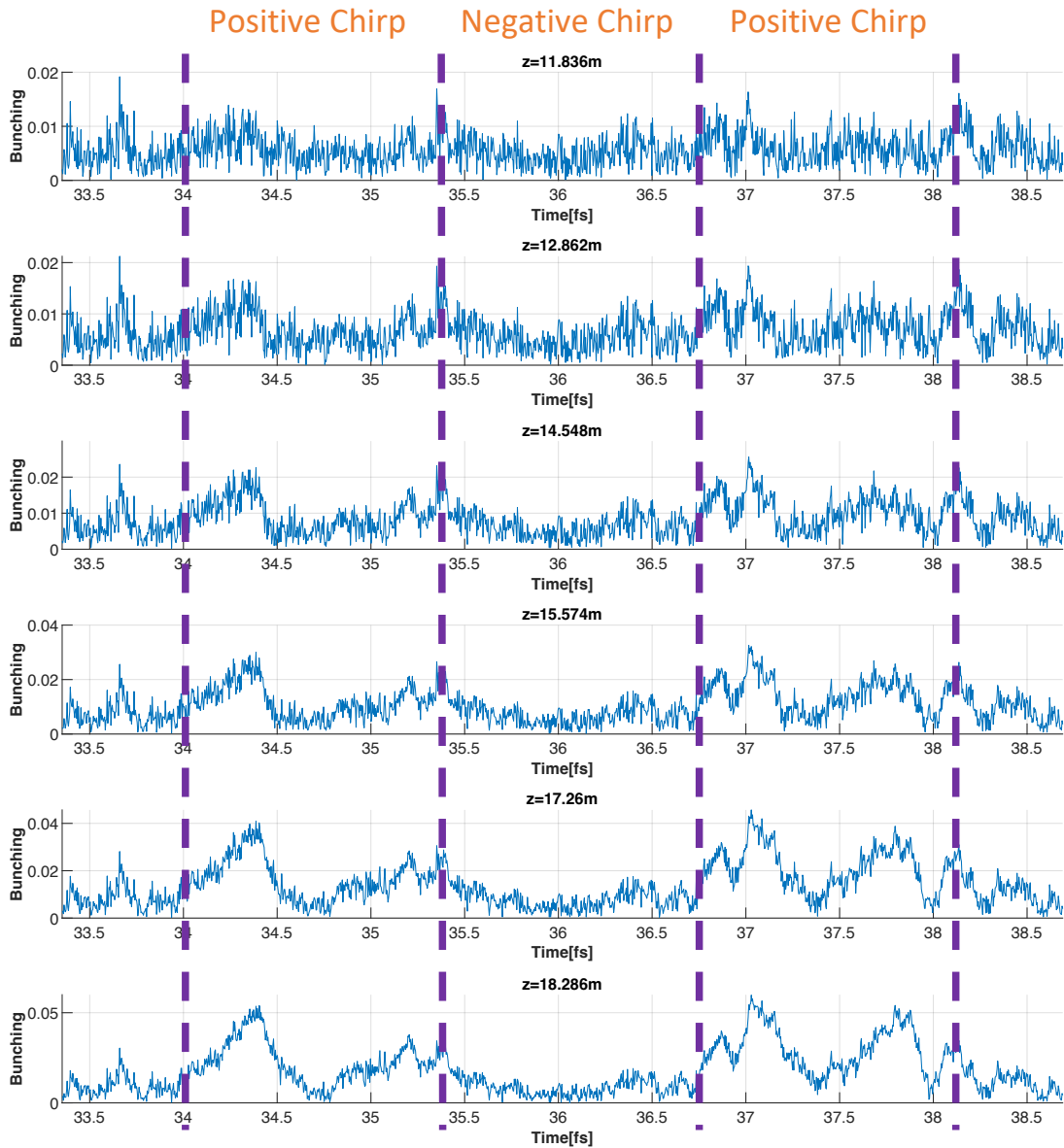
Figure 5.13: Bunching factor for two modulation periods (1600 nm) in the intermediate regime. The purple dashed lines are the boundaries between positive chirps and negative chirps. We notice the bunching growth mainly takes place in the positive chirps.

The intermediate regime typically begins in the third or fourth undulator module and continues until the seventh or eighth undulator module. At a later stage, in accordance with our taper profile design for the undulator parameter, the K-profile reaches its maximum. After this point, the negative taper begins, and the system transitions from the previous regime to the linear regime. These bunching spikes being prepared in this regime will notably contribute to the FEL process in the linear regime.

C) Linear Regime (z = 23m - 40m)

The linear regime is similar to our discussions in Chapter 2. In the section about SASE, we calculated the Green function, assuming that the electron beam is infinitely long and the Green function is steady.

The top and bottom of the beam modulation experience smaller energy variations. Thus, it is closer to fulfilling the requirement of achieving SASE-like gain. The center of the energy modulation, where the slope of the energy modulation is very steep, violates the above assumptions.

However, the situation changes once the bunching and significant FEL radiation have been prepared in the intermediate regime. We can use the undulator taper to maintain the resonance condition at the positions where the FEL pulses are present. The dynamics can be analysed based on the electron bucket, where a formula is often used when talking about tapers [61]:

$$\frac{1}{H_{w0}} \frac{dH_w}{dz} = -\frac{1}{2} \frac{(1 + K_0^2)^2}{K_0^2} \frac{1}{\gamma_0^3} \frac{d\gamma}{dz}, \tag{5.11}$$

where H represents the magnetic field strength, The formula contains two derivatives, one on the left side and one on the right side. The change in dH/dz on the left may compensate for the change in $d\gamma/dz$ on the right, which is the fundamental principle of the slicing method. The simulation result, in particular, Figure 5.11a, validates the method's functionality.

Explanation over the single spike in each cycle in linear regime: (refer to figure 5.10)

In Figure 5.8, the two FEL spikes present in one cycle in the intermediate regime are reduced to a single spike in the linear regime. At the same time, the two colors in Figure 5.10 are also reduced to one color. To enhance the illustration of the process, it would be beneficial to plot the FEL pulses and bunching together in a single figure:

The bunching factor (red) remains insignificant at the beginning ($B \ll 1$). At z = 19.782 m, there are two bunching spikes (red), the bunching spike at the lower energy of the positive chirp located on the left side of the FEL pulse (blue). The bunching peak on higher energy of the energy chirp lines up accurately with the FEL pulses. Starting at z = 25 m, due to the direction change of the taper, the bunching peak at the lower energy location gradually shifts to even lower energy parts, while the FEL pulses vanish. Similarly, the bunching peak on the higher energy part is shifting but towards the right direction on the time axis. Both the bunching and FEL peaks are amplified. Ultimately, only the right peak has distinct and clean FEL pulses. Through Figure 5.14, we demonstrate how in the linear regime, only one pulse in the period can survive, and pulses of a different color vanish. This is due to the matching condition between the bunching and FEL peaks, where only high bunching and high FEL pulse intensity can lead to high-efficiency lasing.
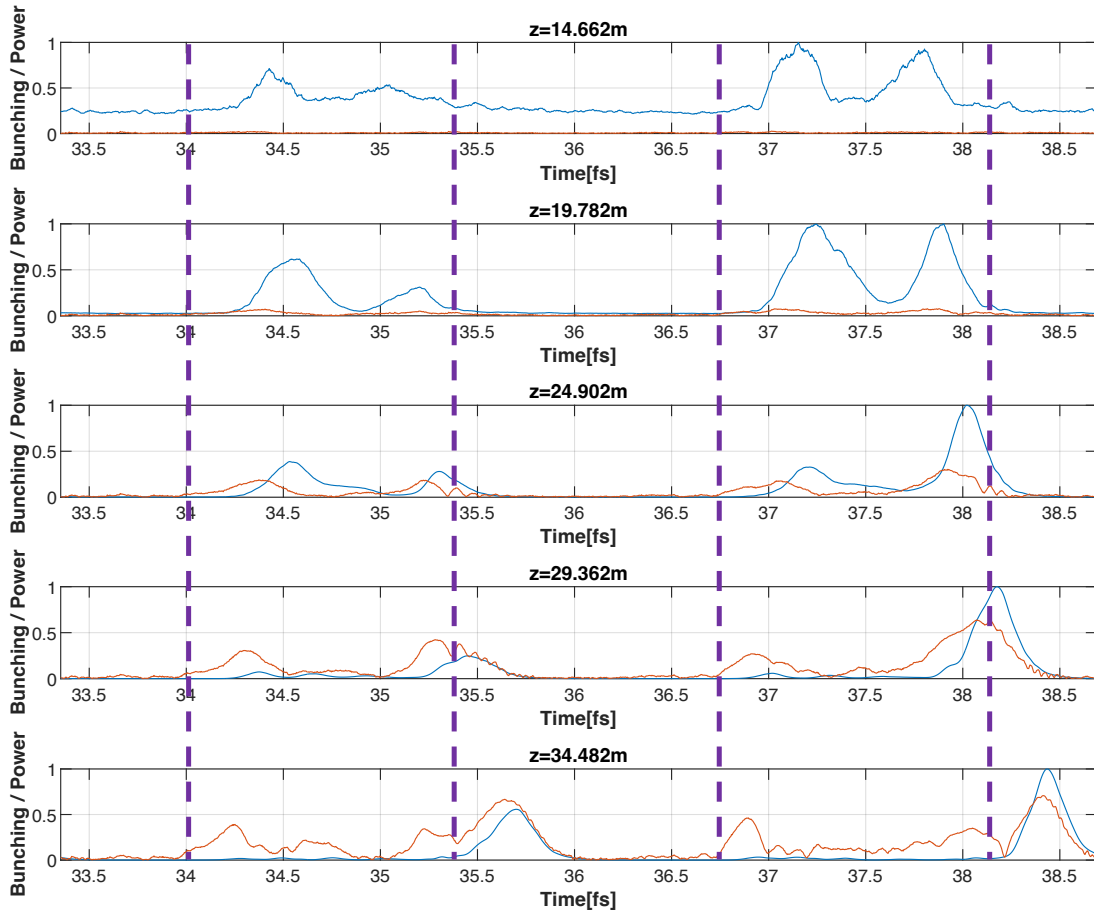
Figure 5.14: FEL power and bunching factor for two modulation periods (1600 nm). Blue curves are the normalised FEL power, and reds are the corresponding bunching factor. The plot starts at around 15m and continues every 5m until around 35m. Two segments, specifically 34 fs to 35.37 fs and 36.67 fs to 38.1 fs, represent the rising edges of the energy modulation. The purple lines indicate the top or bottom of modulation.

D) Saturation Regime (z = 40m - 44m)

In a saturation regime, the radiation intensity can no longer grow exponentially because the beam energy that can be converted into light is exhausted. The intensity of the generated light reaches a maximum level and then stabilizes. From Figure 5.12, it can be observed that several bunching peaks for the last three undulators have reached around 0.7 and are displaying no further growth. This indicates the saturation.

5.5   Optimization through a Stronger Taper in the Saturation Regime

At the beginning of the chapter, we derived the dynamics of the general taper strategy that usually occurs just before the saturation regime, which will allow for more energy extraction

from the electrons to the FEL radiation.

An interesting optimization opportunity was identified, as depicted in Figure 5.11b, where it was observed that the electron beam extracted substantial energy from the photons in the final two modules of the undulator. This observation suggests that our current setup of the K-undulator might not be yielding optimal performance. To address this issue, we conducted a small-scale optimization to find a better configuration of the undulator parameter. In principle, we need a steeper undulator taper, as shown in Figure 5.15:
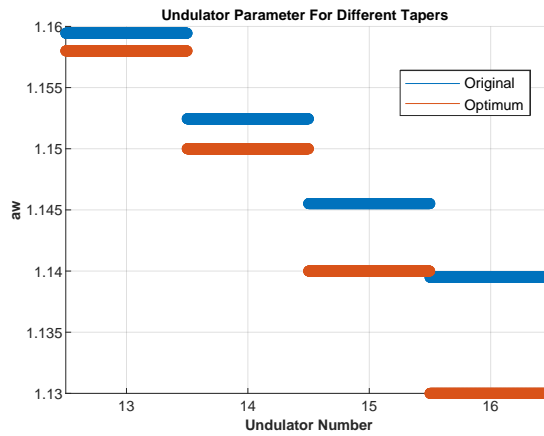
Figure 5.15: We apply different undulator parameters for the last four undulators from the 13th to the 16th. The key is that we need a stronger taper. The 'aw' in the figure equals $K/\sqrt{2}$
.

The result in figure 5.16 shows the performance improvement after applying a strong undulator taper. There is more pulse energy, and the pulse duration is kept low in this saturation regime.
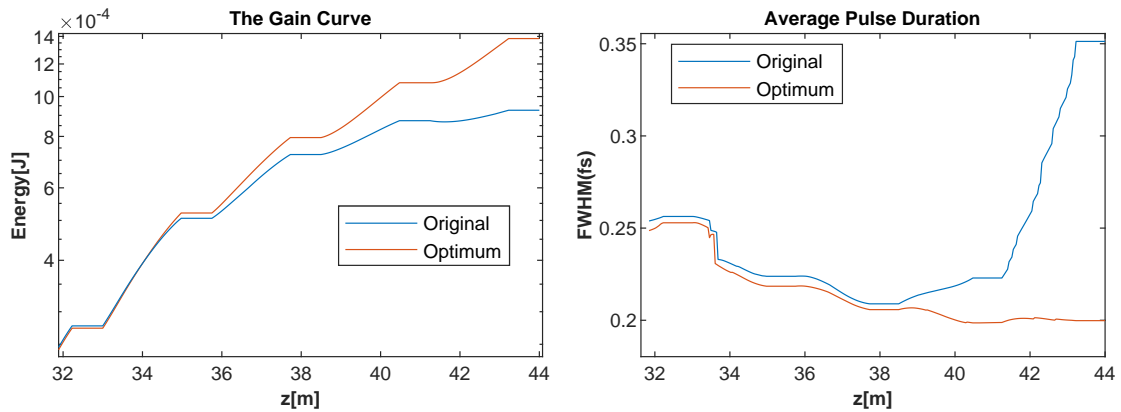
(a) FEL pulses energy with different taper.   (b) Average pulse duration with different taper.

Figure 5.16: After applying a strong taper, the statistical results show a significant increase in pulse energy. Moreover, the pulse duration no longer rebounds, as previously observed. The slight discrepancy at 32 m arises from the differing seed numbers in the two simulation cases.

In addition, we show the electron energy after each undulator module in figure 5.17. We ob-
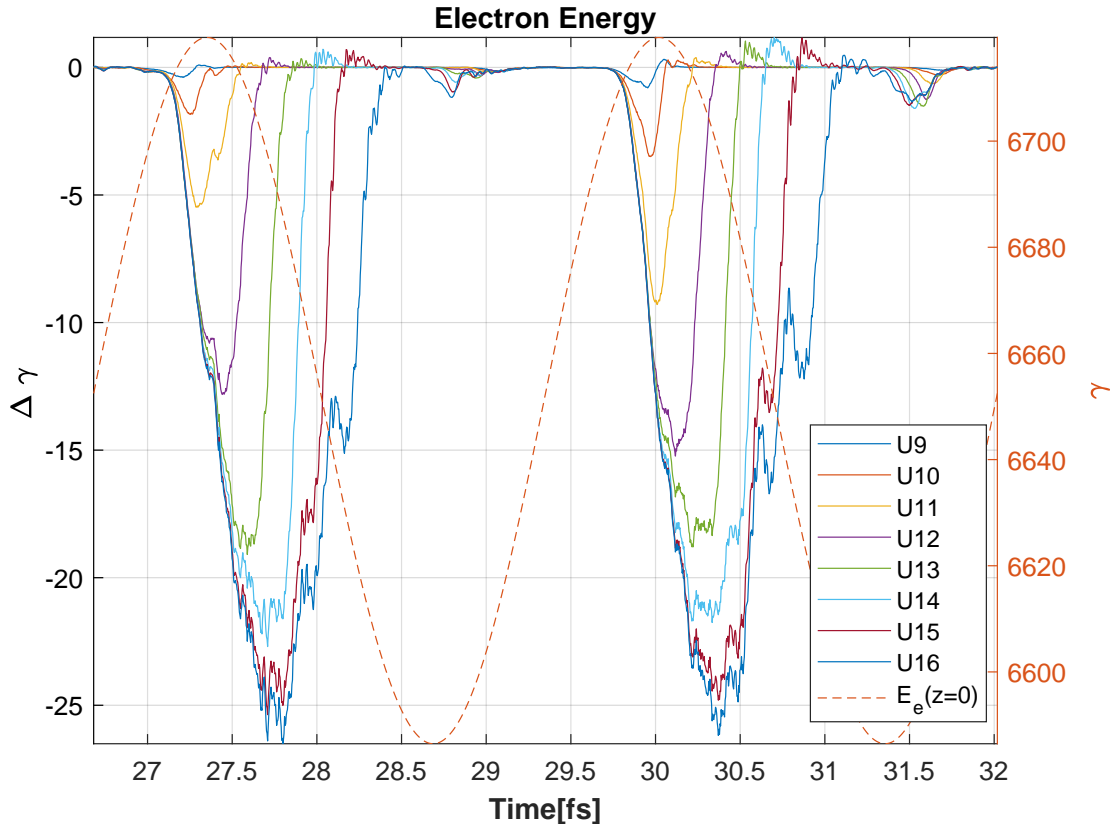
Figure 5.17: The change in electron energy is measured after each undulator when a stronger taper is applied. This can be compared to Figure 5.11b in terms of energy loss for FEL pulses in U15 and U16.

served that the FEL pulse can continue to gain energy during the sliding process by interacting with the fresh electron bunch. This explains why the FEL pulse energy increases. However, it is also observed that after passing the center of beam energy modulation, the value of $\delta\gamma/\gamma$ becomes relatively small, leading it gradually back to a situation of SASE, which broadens the pulse duration. The choice of 980 nm as the taper period was strategic, allowing the optimal positioning of the most suitable slicing to culminate precisely at the centre of the modulation. Furthermore, the spectrum offers insights into which beam segment is lasing during the FEL process, as depicted in Figure 5.18:

Although there have been notable adjustments to the undulator parameter (see figure 5.15), the changes in radiation wavelength are insignificant. We have the resonance equation:

$$\lambda_r = \frac{\lambda_u}{2\gamma^2(z)} \left(1 + \frac{K^2(z)}{2} \right) \tag{5.12}$$

The resonance equation alone can not explain the constant frequency despite significant changes in the undulator parameter. The most likely reason is that the FEL pulses and electrons

(a) Original spectrum.   (b) Spectrum with a strong taper.
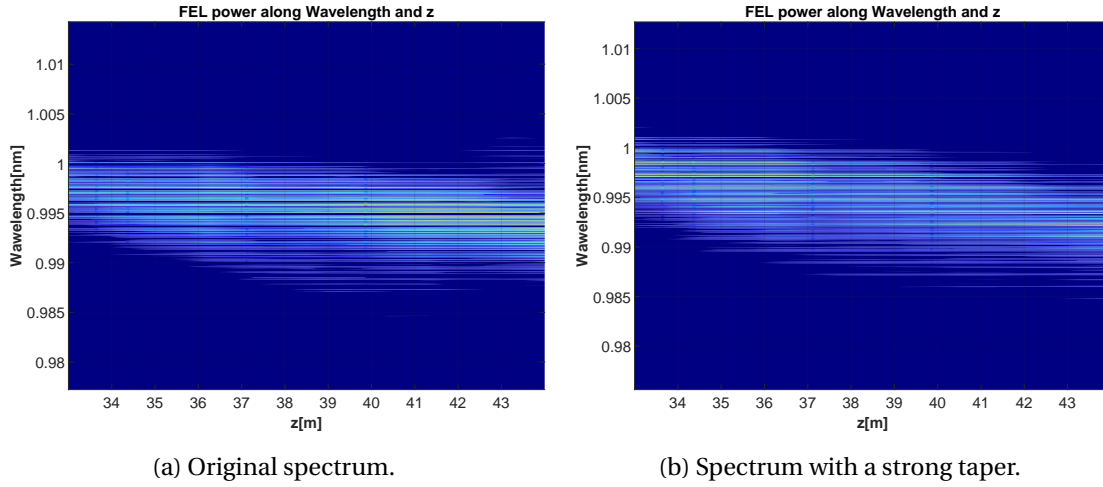
Figure 5.18: Comparison of spectrum. The only difference is a small shift in the radiation frequency, which does not correspond to the large change in the undulator parameter.

are in superradiance dynamics. To provide an explanation, we first plot the bunching and normalised FEL power after each undulator module.

As shown in figure 5.19, powerful FEL pulses slip into the unbunched slices. According to the superradiance dynamics, this leads to radiation emission at the synchrotron frequency defined by the frequencies of the FEL pulses. Meanwhile, the sliding FEL pulses cause the electron bunching peak to move with them, the power of the pulses is increased while their duration is reduced. Further discussion can be found in the Appendix B, where we have derived the superradiance dynamics, and where we conclude that all the optimisations presented in this chapter could be seen as strategies to generate superradiance spikes.

5.6   Conclusion

Starting with the initial assumption that FEL pulses slide along the beam and subsequently designing the undulator taper profile, we conducted a thorough analysis of the simulation data. Nevertheless, we soon noticed that our setup strategies, typically used in references, could explain only some of the phenomena observed in the linear regime.

We examined the dynamics by performing numerous simulations and presented the results of the best simulations in this chapter. The dynamics are categorised into four regimes: the lethargy regime, the intermediate regime, the linear regime, and the saturation regime. The discussion of the intermediate regime reveals distinct dynamic behavior, where the FEL power growth is insignificant, but the bunching spike is prepared for the linear regime. The model's non-linear nature had led to the previous neglect of its dynamics, which are now being explored for the first time in this thesis. However, the cause of the two bunching spikes at the rising edge of the beam energy modulation can not be determined within the context of the
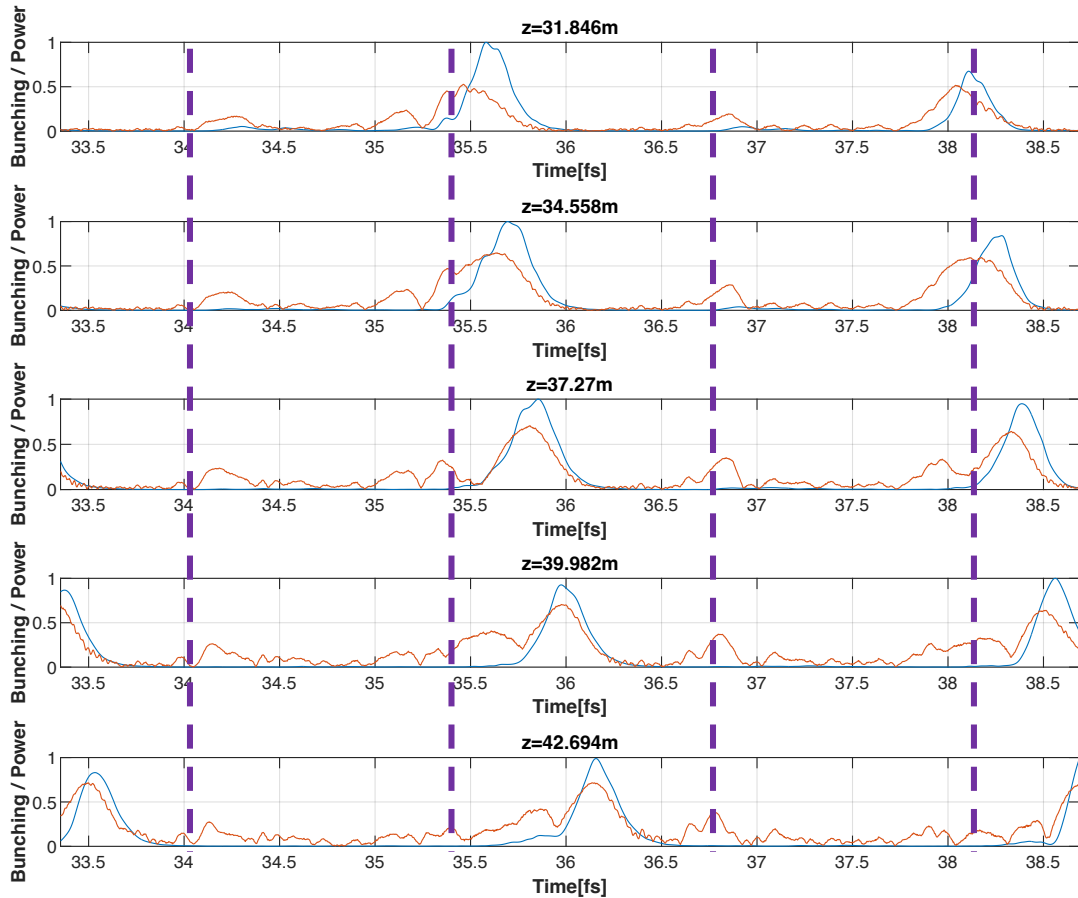
Figure 5.19: FEL power and bunching factor for two modulation periods (1600 nm) after applying a strong taper. Blue curves are the normalised FEL power, and reds are the corresponding bunching factor. The data start at the end of the 12th undulator until the end of the 16th undulator.

current discussion.

Alongside a detailed analysis of the simulation results, we have optimised the reduction in pulse duration in the saturation regime, which is suppressed under a larger taper, leading to a 50% increase in pulse energy. Despite the complexity of the simulation model, our designed profile yielded an outstanding result: extremely short pulses with an average duration of around **200 attoseconds**, with typical saturation power of 100 GW. The coherence time for the SASE model is 170 attoseconds. The simulation results using the slicing method for the actual simulation setting have not been shorter than this value. In the next chapter, we will discuss how we can break the coherence time limit using mode-locking.

6 Mode-Locking: Optimising Magnetic Chicanes for Shorter Pulse Generation Beyond Cooperation Length Limits

In this chapter, another approach to reduce pulse duration is introduced, specifically the use of magnetic chicanes for delay control in our model. This advancement, combined with energy modulation, facilitates mode-locking by aligning the total delay (including slippage and chicane-induced delay) in one module with the seeding laser wavelength. This alignment enables the generation of shorter pulses, thereby overcoming cooperation length limits. This methodology builds on established research [77]. Numerical studies have shown that mode-locking can produce pulses with an average duration of approximately 100 attoseconds, which is a significant improvement compared to the duration achieved with the slicing method.

6.1 Mode-Locking and Short Pulses

The concept of mode-locking in laser oscillators is widely recognised for its ability to generate short optical pulses by maintaining a fixed phase relationship between all laser longitudinal modes [78]. The process involves the gain medium determining the envelope bandwidth of the mode-locked laser oscillator, while the cavity round-trip time dictates the mode spacing. In turn, the round-trip time of the cavity determines the duration of the pulse train [71].

In FELs, mode-locking of X-ray pulses is achieved by overlapping longitudinal-mode comb structures using a series of magnetic chicanes between the co-propagating radiation and the electron beam. It is required that the electron beam energy be modulated at the mode spacing frequency. This method is illustrated in Figure 6.1 [77]. To create the desired slippage between the radiation and the electron beam, as well as to generate the radiation modes, chicane magnets are placed between each undulator module. This is illustrated in parts b) and c) of Figure 6.1.
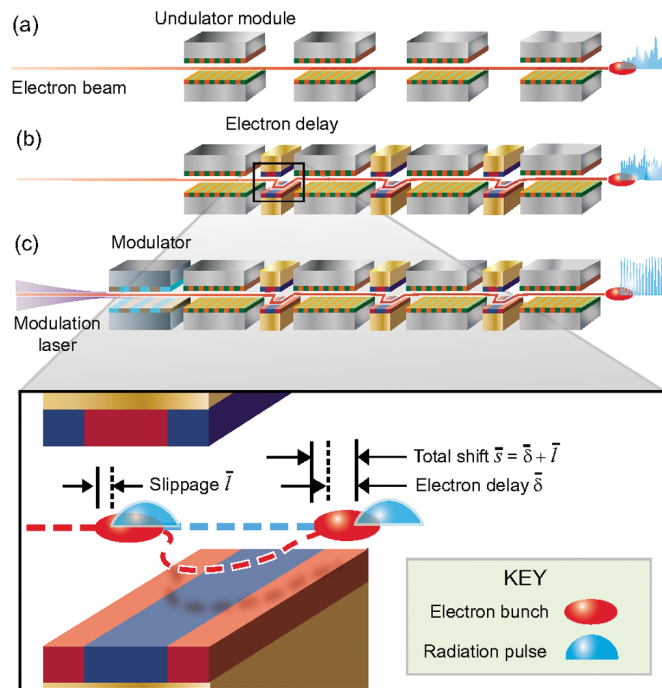
Figure 6.1: Subfigure a) depicts a typical SASE mode, while subfigure b) illustrates the mode-coupling by magnetic chicane in a modular undulator, and subfigure c) shows the mode-locking, where the electron beam has been modulated before entering the undulator. In the lower part of the figure, there is an explanation of how slippage is introduced in the chicane. The total slippage is enhanced, which causes the mode-coupling in b). When total slippage is equal to seeding laser wavelength, we will have c).

In the slicing method, as discussed in Chapter 5, the undulator taper's effect on energy modulation allows for selective frequency filtering. This is achieved by carefully tuning the undulator parameters to yield short pulses. However, mode-locking does not occur, as the localized noise source evolves independently in different regions along the beam, resulting in no phase correlation. The wavefront propagating through the electron beam determines a lower bound for the pulse duration, associated with the FEL cooperation length l_c [14, 79]. The cooperation length is defined by the equation $l_c = L_g \lambda_r / \lambda_u$, where L_g is the gain length, λ_r is the radiation wavelength, and λ_u is the undulator period. It represents the slippage distance over one gain length. In the Athos undulator, the cooperation length for a radiation wavelength of 1 nm is approximately 170 attoseconds. The results achieved using the slicing method have not been shorter than this value.

In this chapter, the investigation focuses on generating shorter pulses using the mode-lock method at the SwissFEL Athos beamline. The results will demonstrate that this method can successfully generate pulses shorter than those achieved by slicing.

6.2 Effects of Delaying Chicanes

Delaying chicanes are important components for achieving mode-locking. The direct effect of delaying chicanes is the introduction of phase shifts, exemplified by $\bar{s} = \bar{l} + \bar{\delta}$, where $\bar{s}$ represents the total phase shift, $\bar{l}$ the slippage, and $\bar{\delta}$ the delay introduced by the chicane. Due to the chicanes, the emitted radiation experiences increased interference with more electrons, resulting in improved coherence across the beam and increasing both the cooperation and coherence lengths of the FEL radiation.

A solution can be obtained by applying the Fourier transform time shift relation to a series of N undulator modules and chicanes [77]:

$$\tilde{E}(L,\omega) = \tilde{b}_0 \, l \, \mathrm{sinc}\left(\frac{\omega l}{2}\right) \frac{e^{iN\omega s} - 1}{e^{i\omega s} - 1} e^{-i\omega l/2} \tag{6.1}$$

The sinc function's envelope undergoes modulation through a 'frequency comb' (wherein the exponential term $e^{-i\omega l/2}$ is present), leading to the existence of sidebands within the spectrum.

In addition, the optical klystron effect [80, 81, 82] substantially impacts the dynamics of mode-locking [77]. The optical klystron effect involves implementing two undulators separated by a dispersive section. The initial undulator generates density modulation (bunching) in the electron beam, and the subsequent undulator amplifies the radiation by utilising these bunched electrons. The introduction of delay chicanes can lead to longitudinal energy dispersion, which in turn can enhance the FEL amplification process, reducing both amplification and cooperation lengths. The combination of increased slippage and reduced amplification length results in a modified cooperation length. However, since the seed laser wavelength is much larger than the slippage in one module ($\bar{s}$ =800 nm compared to $\bar{\delta} \approx$ 50 nm), the cooperation length primarily increases.

6.3 Delay Control Through Magnetic Chicanes in Athos

In this section, we discuss applying mode-locking to the Athos undulator. The Athos undulator is configured with magnetic chicanes between each undulator module. To achieve mode-locking, the first step is establishing the periodicity of the beam. This is accomplished by using a seeding laser with a Rayleigh length that is notably longer than the wavelength. As the electron beam interacts with the laser, it undergoes modulation to reproduce the inherent 800 nm periodicity of the seeded laser. We introduce a precisely calculated delay into the electron beam, allowing the FEL pulses to advance an entire cycle after each module, as shown in Figure 6.2. This approach anticipates mode-locking.
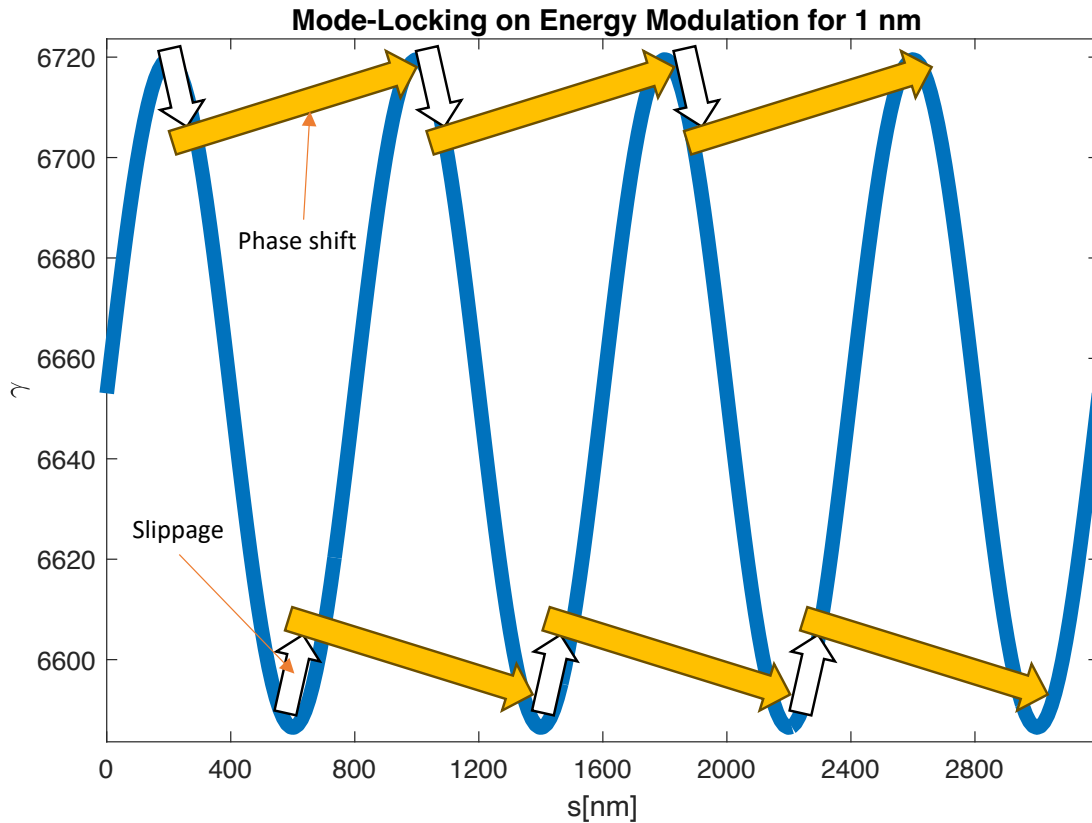
Figure 6.2: Mode-locking mechanics in the Athos Undulator. The blue curve represents beam modulation. After each module, the electron beam is delayed by a magnetic chicane, resulting in FEL pulses shifting forward to align with the beam in the next cycle. This spatio-temporal shift is indicated by the yellow arrows.

6.4   Simulation Setup

6.4.1   Beam Definition

In keeping with the settings outlined in the previous chapter on the slicing method, the electron beam features an energy modulation with a wavelength of 800 nm. The beam operates at a current of 3 kA and has a center energy denoted by $\gamma = 6653$. It experiences a modulation amplitude of 1%, equating to a maximum energy deviation of $\Delta\gamma_{max/min} = \pm66.53$. As the beam enters the undulator, its density is uniformly distributed. Moreover, the energy spread of the beam is 501 keV, accounting for a negligible 0.017% of the total beam energy.

6.4.2   Undulator and Chicanes Setup

The setup process involves not only the configuration of the undulator parameters, but also the setting of the magnetic chicanes that follow each undulator module. We take the radiation

wavelength as 1 nm. Since we have $K(z) = \sqrt{2\left(\frac{2\lambda_r\gamma^2(z)}{\lambda_u} - 1\right)}$, for $\gamma = 6653 * 0.99 = 6586.47$, the corresponding K = 1.602. The next step is to set the total slippage equal to the seeding laser wavelength of 800 nm. This method has the advantage of simplifying the setup process, as a single value can be used for all modules.

6.5 Simulation Result and Analysis

I directly measured the slippage distance in one module and found that the FEL pulse velocity is almost identical to that of the electrons. Thus, each Athos undulator module has 52 periods, each equating to 1 nm, totaling 52 nm. The connection point has a 1 nm deviation, necessitating a total delay of 53 nm after each module. For an 800 nm period, the cumulative necessary delay across all modules sums to a total of 747 nm. For all 16 undulator modules, a consistent K value of 1.602 and a cumulative delay of 747 nm are applied.

6.5.1 Simulation Results

Based on the previously mentioned settings, the simulation results are presented in the following figures:

1. Gain curve (Figure 6.3a)

In Figure 6.3a, saturation occurs after eight undulator modules, around z = 22 m. The saturation energy is significantly reduced to 10^{-5} J, considerably lower than the performance for the standard SASE.

2. Normalised FEL power (Figure 6.3b)

The total delay after eight modules amounts to 6400 nm, with each module contributing 800 nm of delay. To avoid the impact of the beam tail, we start the analysis at 10000 nm. Figure 6.3b shows the FEL power between 10000 nm to 20000 nm, equivalent to 33.3 fs to 66.7 fs on the time axis. It is observed that the FEL pulses preserve their time locations after each module, indicating the total delay in a module is equal to the wavelength of the seeding laser.

3. FEL power at different z-positions (Figure 6.3c)

In Figure 6.3c, a pulse sequence featuring 400 nm spacing between successive spikes is generated. The pulse spacing is 400 nm as both the bottom and top of the modulation meet the resonance condition while keeping constant K. From z = 9.124 m onwards, well-separated pulses with marginal background noise are displayed. The saturation power can reach 1 GW. Notably, some pulses exhibit significantly higher intensities, indicating variability in the shot noise within each modulation period. The current methodology appears inadequate in mitigating shot noise. It is postulated that the intensity distribution of an individual pulse follows a gamma distribution, similar to SASE.

(a) FEL pulse energy along the z-axis.   (b) FEL power along the z-axis and time axes.

(c) FEL power at different z positions.
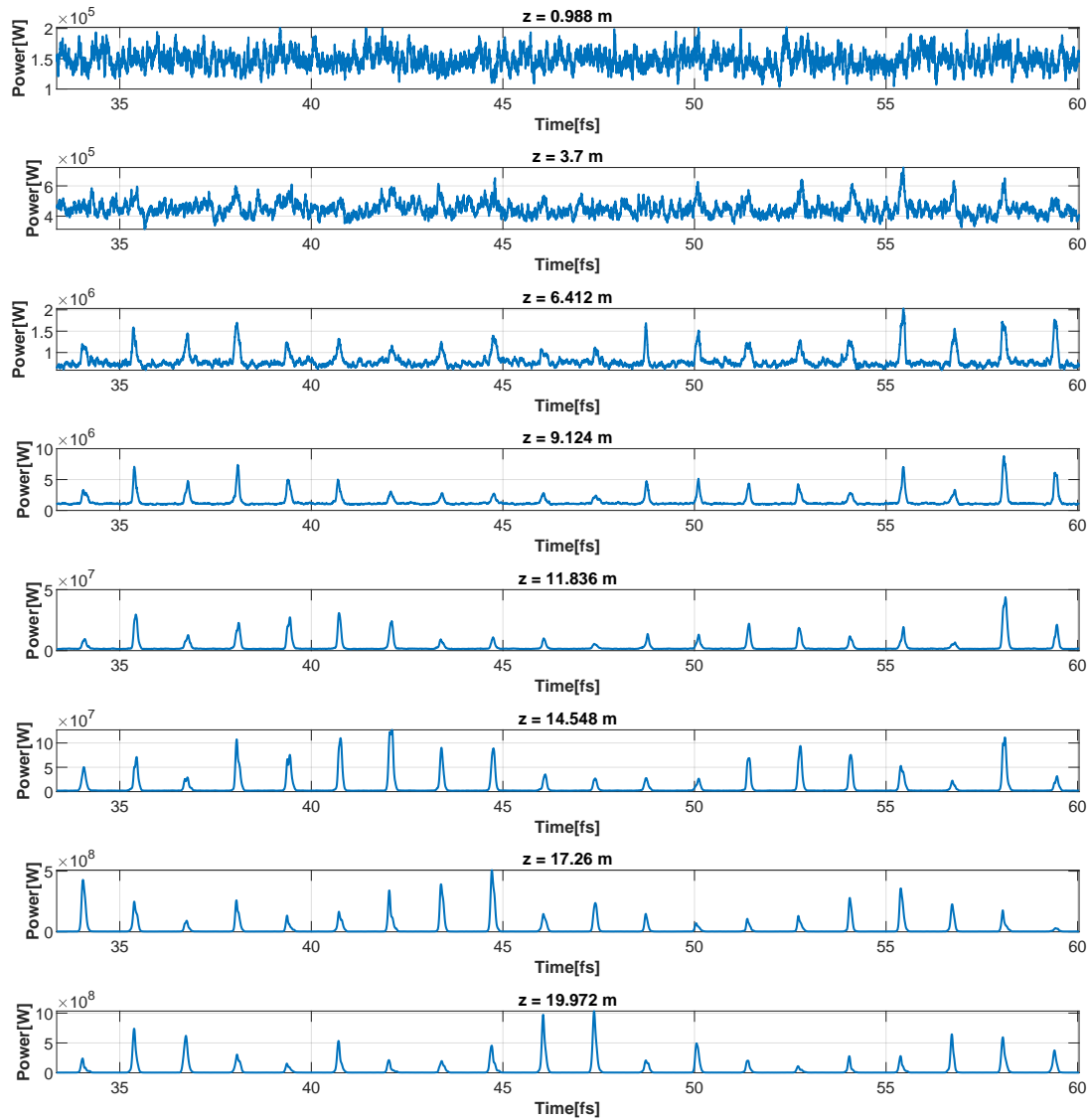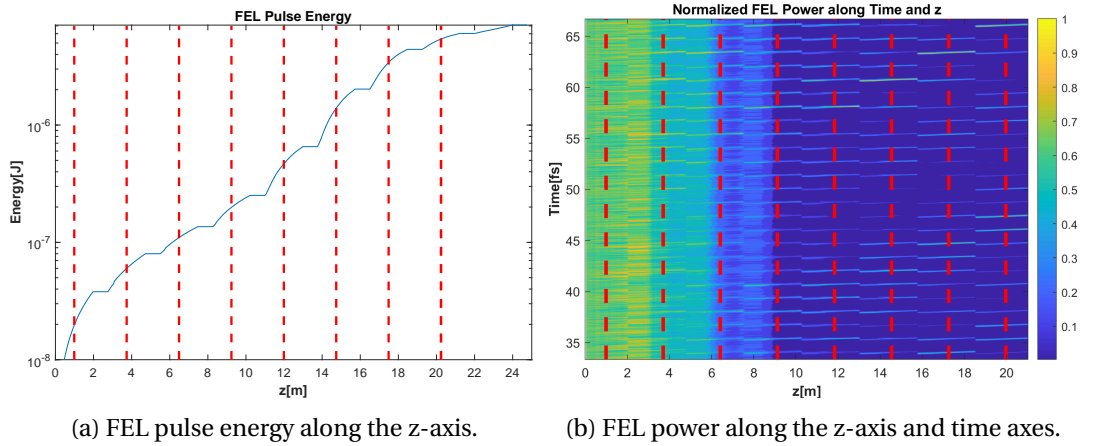
Figure 6.3: Mode-locking simulation results for $\lambda_r = 1$ nm.

4. Average pulse duration along the z-axis with error bars.
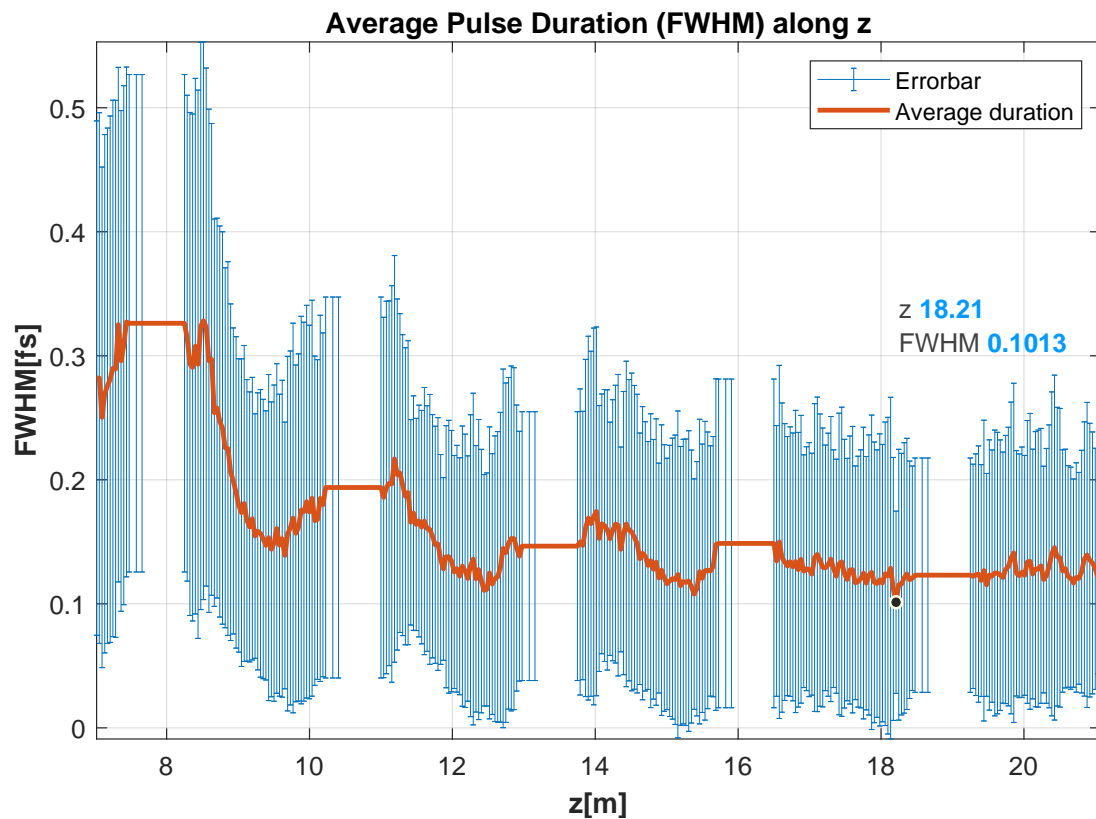
Figure 6.4: Mean pulse duration along the z-axis. The shortest average duration is observed at z = 18.21m, with an average FWHM of 101.3 as.

The measurement begins at z = 7 m. Initially, the average pulse duration is only 300 attoseconds. It gradually decreases as the FEL process unfolds, reaching a minimum of around 100 attoseconds in the seventh undulator. Once saturation is achieved, the duration stabilizes at approximately 120 attoseconds. At the end of each module, a slight increase in pulse duration suggests that the beam may have slipped out of resonance. This could be attributed to the optical klystron effect, which shortens the gain length. However, this increase in duration is not particularly significant.

5. FEL power along wavelength and z.
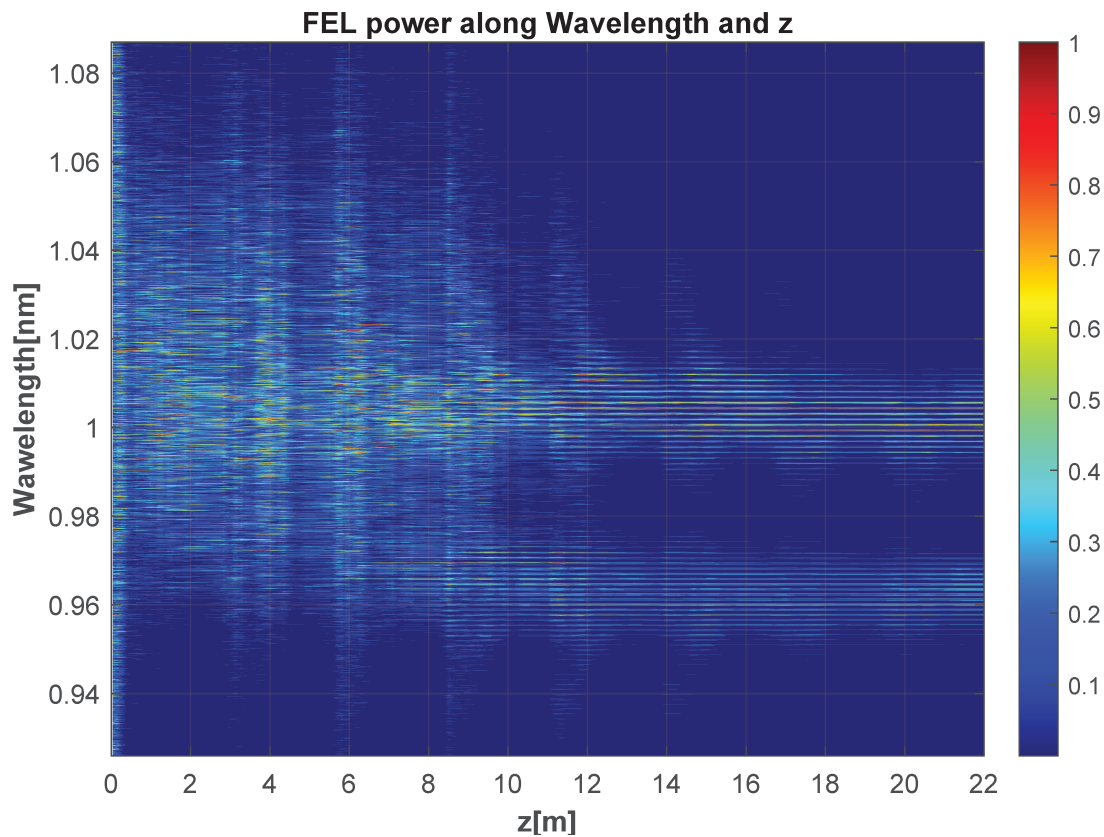
Figure 6.5: FEL power along wavelength and z-axis[I].

The spectrum reveals two distinct wavelengths: one centered around 1 nm and another around 0.96 nm, aligning with a 1% modulation amplitude condition. They correspond to the bottom and the top of the energy modulation. Since the undulator parameter K is constant, the same resonance condition applies to both the top and bottom of the modulation. Mode-locking becomes evident from z = 10 m onward, as indicated by the appearance of sidebands. The sidebands at z = 21.406 m are depicted in Figure 6.6.

Additionally, the spectral bandwidth in each undulator module starts out broad in the initial stages but gradually narrows as the module progresses. This result aligns with the impact of the optical klystron effect, where beam compression enhances longitudinal coherence, initially resulting in a broader bandwidth.

[I]For a clearer illustration, the reader is referred to the PDF version, which is clearer than the printed version.
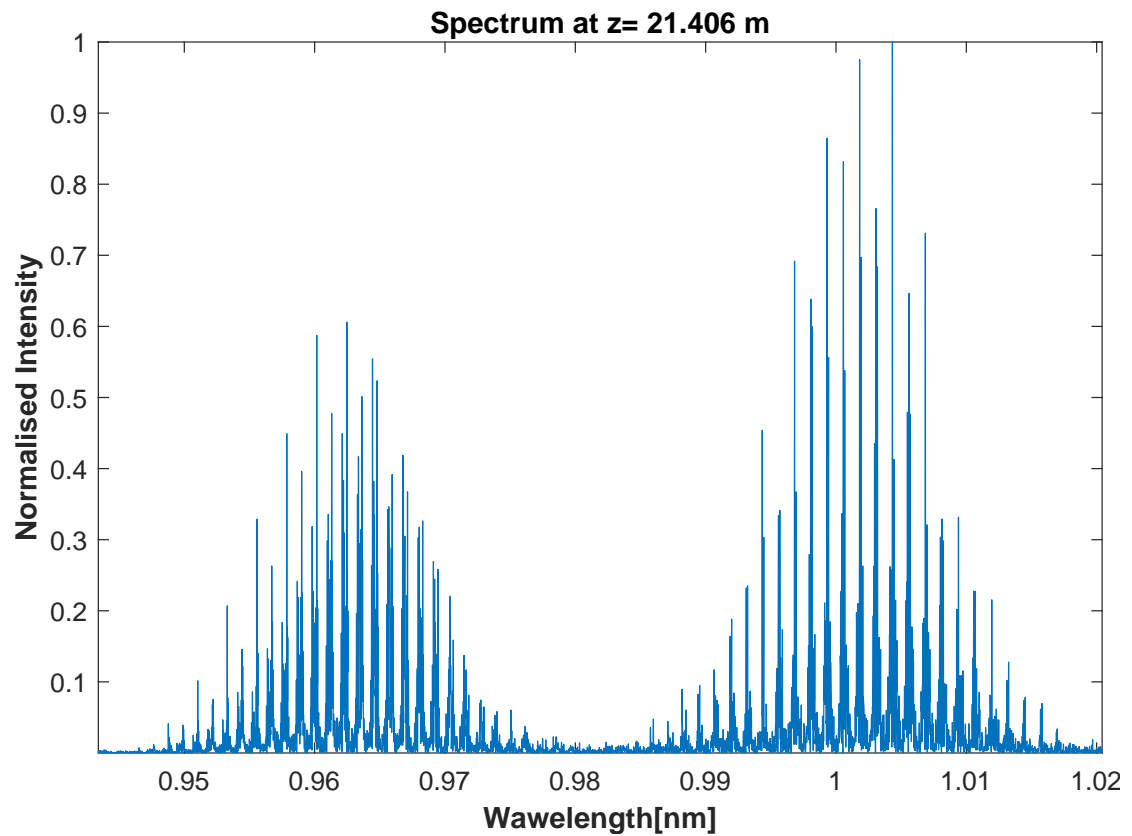
Figure 6.6: Spectrum at z = 21.406 m. There are two wavelengths: one is centered around 1 nm and another around 0.96 nm, which correspond to the bottom and the top of the energy modulation. Using a beam with a smaller modulation amplitude may result in the mixing of modes from two frequencies. It would be interesting to observe the resulting pulse duration. It is unclear what effect mode-locking would have. However, based on experience with slicing, reducing the amplitude tends to increase the pulse duration.

6. Bunching and energy spread at different z positions

At z =19.972 m in figure 6.7, although the bunching factor, denoted by $B \approx 0.1$, and the energy spread, represented by $\sigma \approx 2$, have not reached the typical threshold for saturation, the energy of the FEL pulses have reached its saturation.
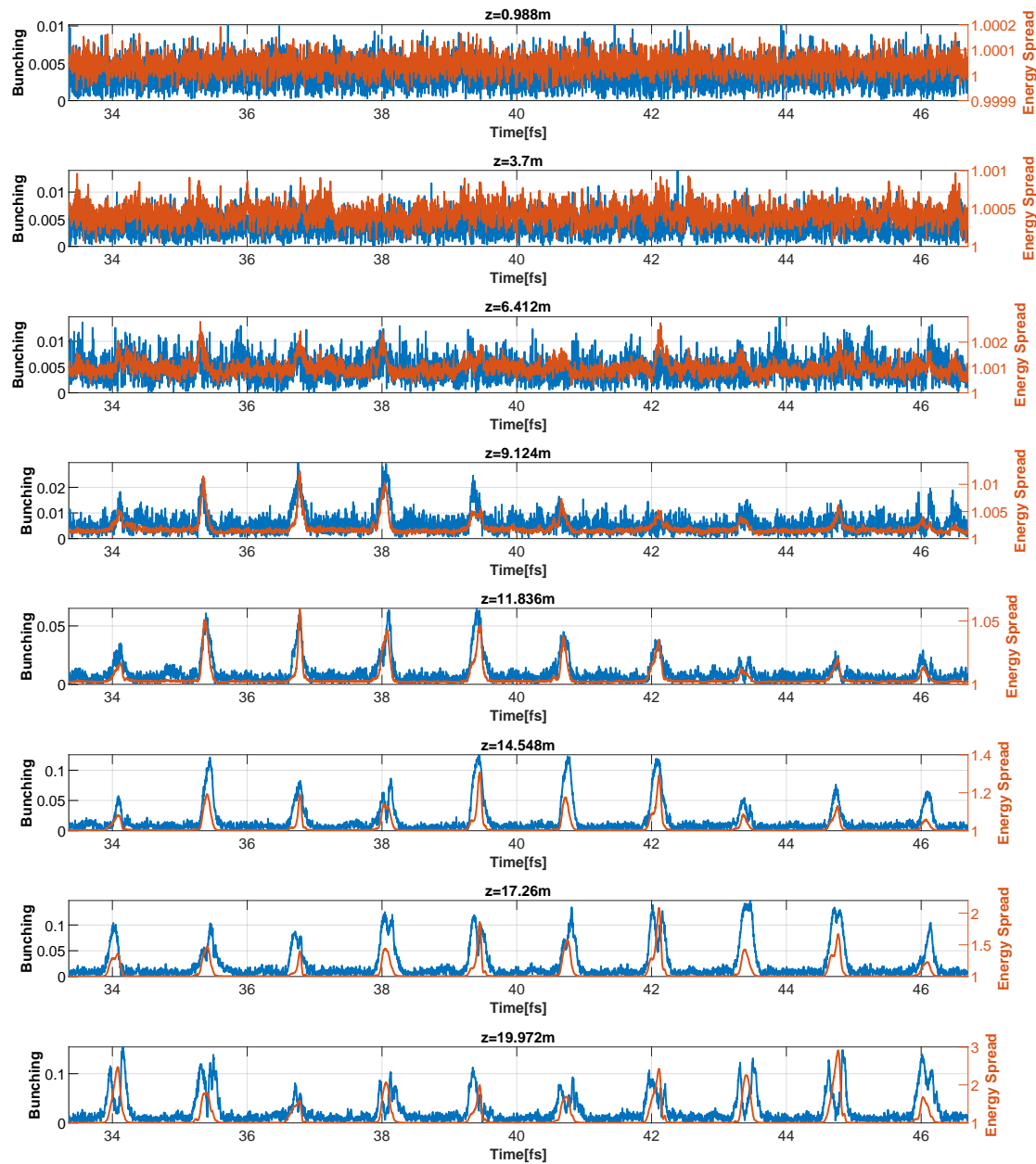
Figure 6.7: Bunching (in blue) and Energy spread (in red) at different z-positions.

6.5.2   Simulation Results Analysis

Possible reason for reduced saturation power.

To discuss the reason for the reduced saturation power in mode-locking, we compared the locations of FEL power, bunching, and energy spread, as shown in Figure 6.8. This figure presents data at different z positions, corresponding to the start of each undulator module. We focused on their longitudinal positions. First, the locations of the energy spread spikes (yellow)
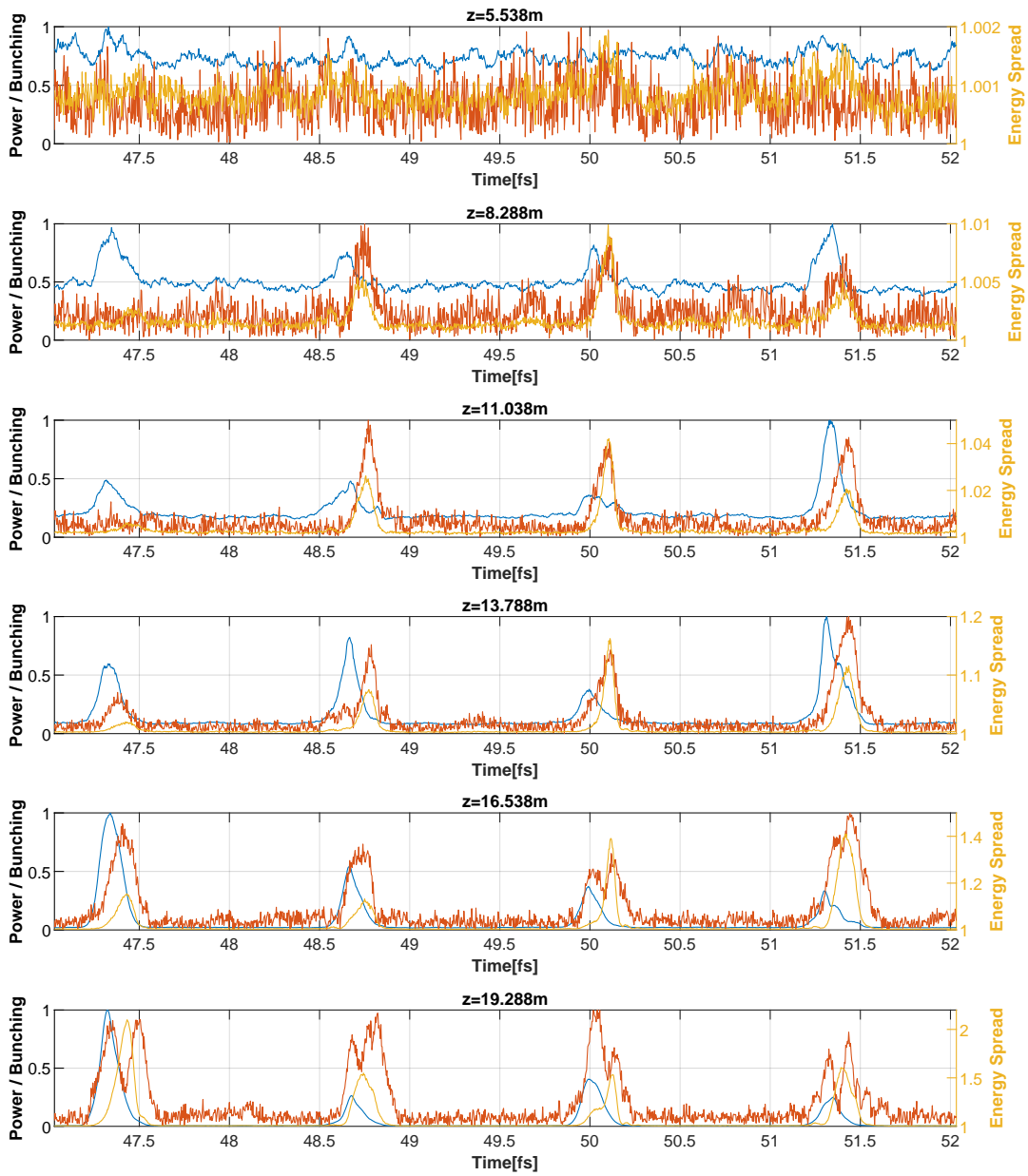
Figure 6.8: Phase comparison of FEL pulses, bunching factor and energy spread. For FEL power and bunching factor, it is normalised data. The energy spread is raw data.

are observed to be generally constant across different modules. Besides, the FEL power spikes (blue) are synchronized in phase across the modules.

Significant changes are noted in the bunching factor (red) peaks at different z positions. Initially, they become more pronounced up to z = 16.538 m. Subsequently, at z = 19.288 m and around certain time positions (e.g., around time = 47 fs), the bunching splits into two, each separated by an energy spread peak.

We conclude that the reason for this early saturation is as follows: the FEL power peaks first undergo delay control after the completion of one module, causing them to slip into energy spread peaks and thus cannot be further amplified in the subsequent module. Consequently, saturation is reached prematurely. The combined influence of FEL power, energy spread, and bunching is likely the cause for the significantly reduced saturation power.

To address the issue, several potential strategies could be considered. These include using a seeding laser with a shorter wavelength, implementing mode-locking every two or three modules, or introducing density modulation in the entering beam. Each of these approaches would require further numerical studies to fully assess their effectiveness.

Another possibility is implementing a strong taper across the modules before the bunching spikes have the opportunity to split into two. I have conducted simulations for this approach, which demonstrated the feasibility of obtaining large radiation power on the scale of 100 gigawatts, comparable to the slicing method. However, achieving a clean power spike proved challenging due to the disruption of the mode-locking condition. As a result, this approach is not presented in this chapter.

6.6 Conclusion

In this chapter, we have explore the application of mode-locking method in Athos undulator. Based on our simulation results, the mode-locking method delivers promising results, resulting in a 50% reduction in pulse duration compared to the slicing method, with an average value of 100 attoseconds, beyond the cooperation length limit. We observe very clean and well-separated pulses.

The importance of mode-locking will be further explored in the next chapter, where we will combine it with all the other configurations to produce shorter pulses of 100 attosecond scale at $\lambda_r = 4$ nm.

7 TGU Configuration: Attosecond Pulse Generation over Extended Radiation Wavelengths

At a wavelength of λ_r = 4 nm, the mode-locking method alone is insufficient to produce short pulses throughout the entire module in the Athos undulator. This chapter introduces the concept of an inner module linear undulator taper, which is based on a rotated transverse gradient undulator. A positive taper, featuring a 16 % difference in each module, is proposed in combination with mode-locking to achieve an average pulse duration of approximately 110 attoseconds. This short duration is attributed to the large bandwidth provided by the strong undulator taper, which effectively shortens the pulse duration during mode-locking.

7.1 Slippage in Extended Radiation Wavelengths

In previous chapters, the case of λ_r = 1 nm was discussed, where the module's length does not significantly limit the pulse duration performance, as the pulse duration continually decreases within the module. However, at λ_r = 4 nm, slippage becomes more significant for longer wavelengths, resulting in the pulse duration increasing again within the module. The average pulse duration with mode-locking at this frequency is shown in Figure 7.1. Initially, the pulse duration within the module decreases but subsequently increases, indicating that the module is excessively long. Figure 7.2a displays the pulse duration along the z-axis in the 4th module (z = 8.25 m to 10.25 m, as shown in Figure 7.1). The shortest duration is 144.6 attoseconds at z = 8.896 m (period number N_p = 18), while at z = 10.19 m (N_p = 52), it is approximately 600 attoseconds. This result represents a significant improvement over the ESASE simulation results in Chapter 4, where a short pulse structure could not be achieved due to strong slippage.
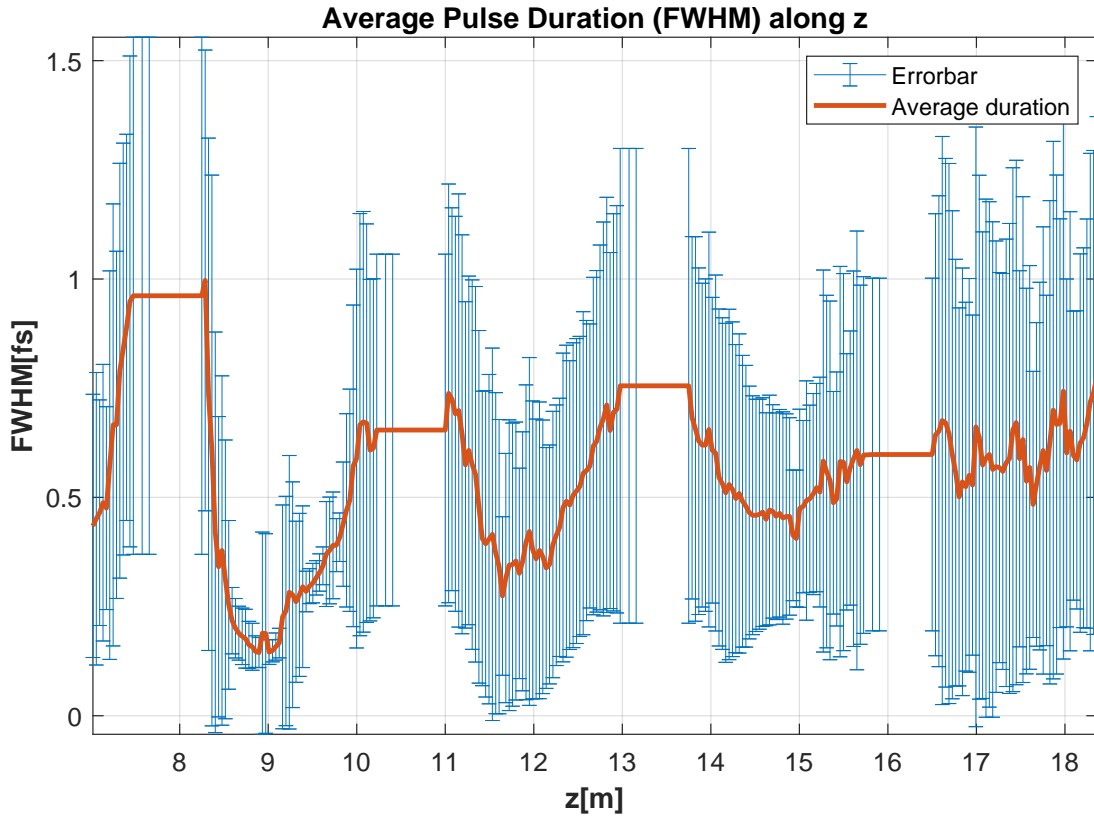
Figure 7.1: Average pulse duration along z with mode-locking for λ_r = 4 nm. The undulator setting is with the mode-locking. The measurement starts at z = 7 m, which in the third undulator module. We see that in most modules the pulse duration first decreases and then increases within the module, indicating that the module is too long for the target wavelength.

Figure 7.2b shows that the pulses consistently grow and narrow from N_p = 1 to N_p = 25. Figure 7.2c indicates that the main pulses no longer grow from N_p = 25 to N_p = 49, and pulse duration increases in this remaining part of the undulator. From this result, it is concluded that mode-locking alone cannot generate short pulses throughout the entire module, as the module length is too long relative to the gain length for a 4 nm radiation wavelength. One potential solution could be reducing the number of undulator periods. However, physically shortening the module itself is not feasible.
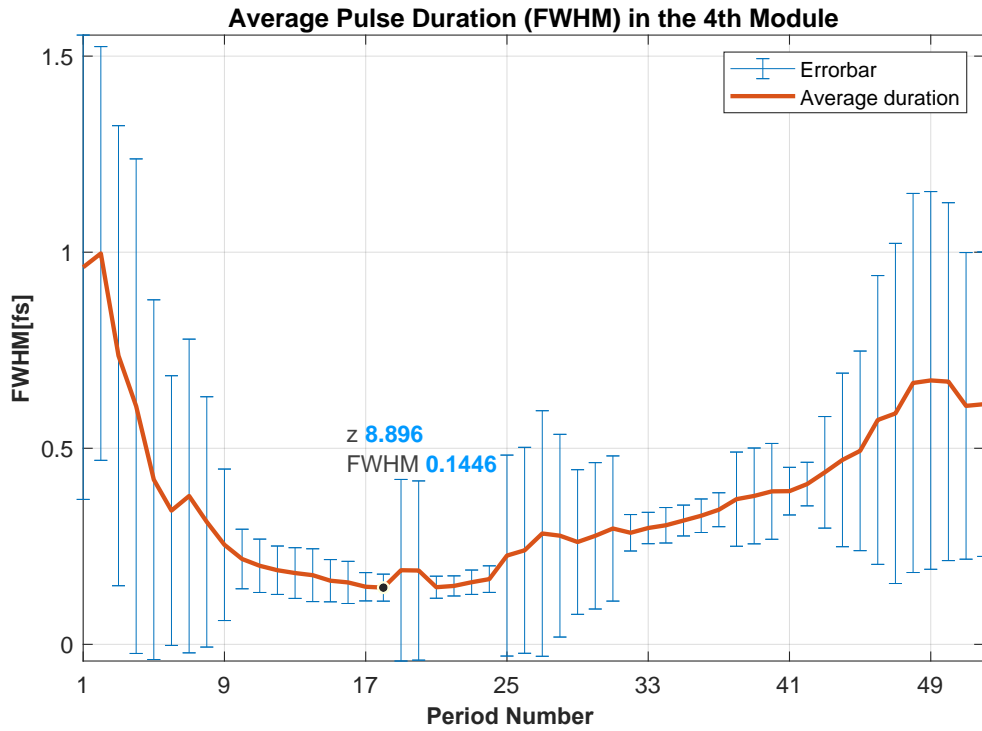
(a) Average pulse duration in the 4th module.
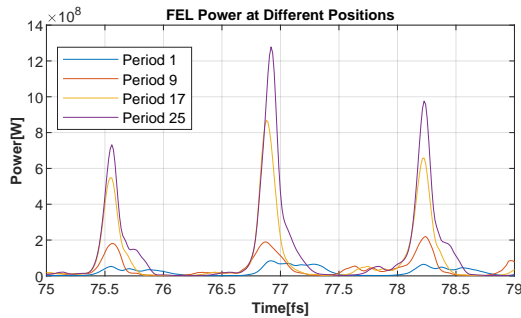
(b) FEL pulses at N_p = 1, 9, 17, 25.
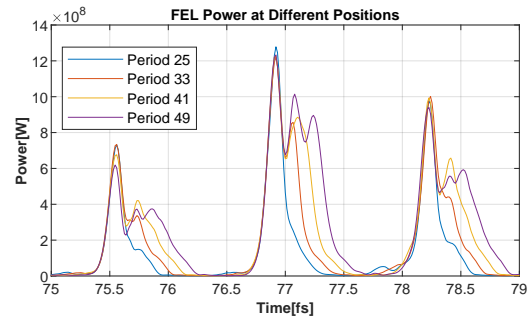
(c) FEL pulses at N_p = 25, 33, 41, 49.

Figure 7.2: Average pulse duration in the 4th module (z = 8.25 m to z = 11 m) (a) and FEL pulses at selected positions (b) and (c).The axis has been replaced by the number of undualtor periods, with a total of 52 in one module. In the 4th module the shortest result is only 150 attoseconds, in figure 7.2b we have plotted the periods 1, 9, 17, 25, where the main pulses are constantly growing. However, after period 25, the duration starts to increase, with the main pulses stopping to grow and broadening, as shown in figure 7.2c.

7.2 Continuous Linear Taper within Undulator Module

In this section, it will be demonstrated that a positive taper of 16 % within the module can prevent an increase in pulse duration. This approach keeps the pulse duration short until

the end of the module. The FEL process may become substantially less efficient if a taper is so large that it completely exceeds the SASE bandwidth. Reference [61] proposed a strong reverse taper to mitigate the slippage effect, and in some conditions, bunching can survive [83]. The outcome is that the segment of the beam where the FEL pulse is present may still be amplified despite reduced efficiency. This approach is also discussed in [84]. Additionally, a strong taper results in a slower FEL process and a longer saturation length, which provides more opportunities for chicanes to control the delay, thereby contributing to achieving mode-locking.

7.2.1   Method: Rotated Transverse Gradient Undulator

The linear taper within the module is achieved using a rotated transverse gradient undulator, which projects the gradient from the transverse to the longitudinal direction.

The transverse gradient undulator [85] is an undulator that varies the amplitude or phase of the magnetic field across the electron beam's transverse profile. It is utilised in applications such as Laser Plasma Accelerators [86, 87], electron synchrotrons [88], and FEL oscillators [89]. The primary objective of this technology is to maintain significant FEL gain even with a large energy spread in the electron beam. Figure 7.3 illustrates the TGU's operational principle. The magnet on the left slope has a narrower spacing and higher undulator strength, while the magnet on the right side has broader spacing and reduced strength. By positioning the higher energy portion of the electron beam on the left and the lower energy portion on the right, a consistent radiation frequency is achieved across the beam, thereby reducing the impact of energy spread.
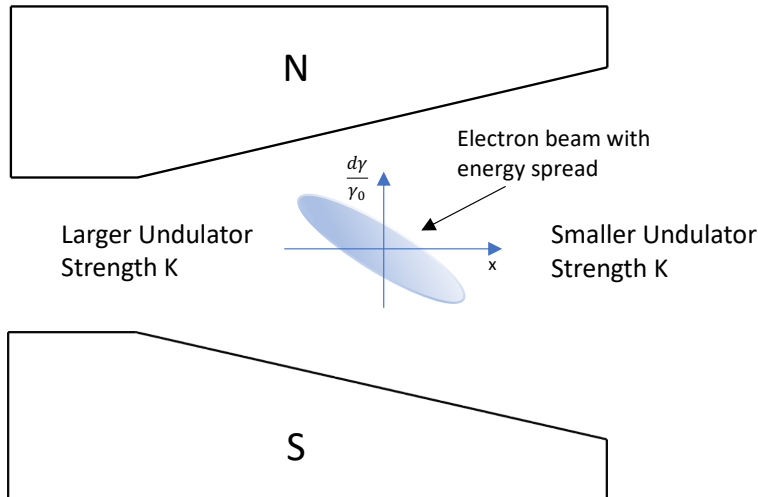

Figure 7.3: The operational principle of a TGU.

The Athos undulator features an Apple X design [90], comprising four identical magnetic arrays positioned at 45, 135, 225, and 315 degrees, respectively (see Figure 7.4a). Each array can be independently moved both longitudinally and radially, thus enabling a transverse gradient

profile [66]. Additionally, the Athos undulator's configuration allows for a slight rotation (less than 0.5 mrad) relative to the electron travel direction. This design enables the projection of the transverse gradient K into the longitudinal direction, as demonstrated in Figure 7.4b. As a result, a continuous linear undulator taper in the longitudinal direction is achieved in each module.

(a) Apple X undulator [5].

(b) A Rotated TGU[I].
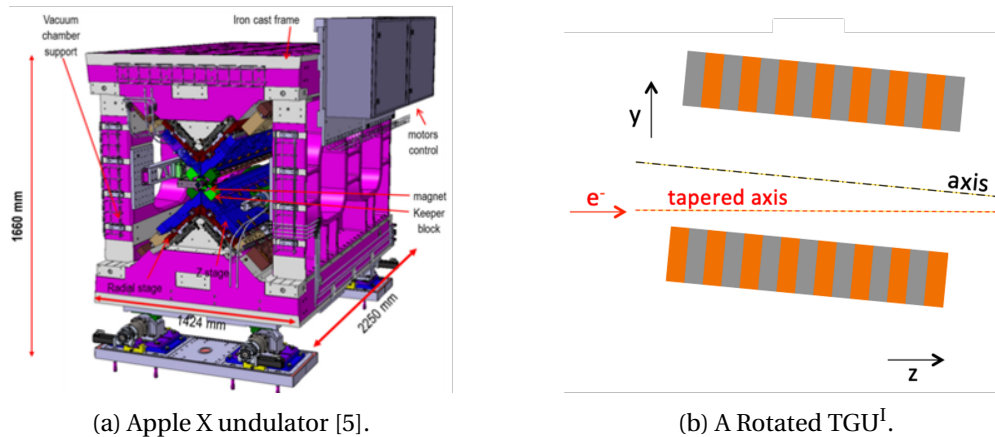
Figure 7.4: Method to achieve linear taper within the undulator module: Rotating the Apple X undulator to obtain a linear undulator taper within the module. It should be noted that the electron beam will be deflected to one side, resulting in a 'banana' shaped trajectory, however, this effect has not been taken into account in the thesis model.

7.2.2 Evaluation of the Linear Taper within Module

This subsection examines the effects of the inner module linear taper on pulse duration. In the simulations, the taper shows improvements for both $\lambda_r = 1$ nm and $\lambda_r = 4$ nm. To conclude this subsection, a 16 % positive taper at $\lambda_r = 4$ nm is chosen for subsequent simulations in the following section.

The initial trial work involved mode-locking at a radiation wavelength of 1 nm, combined with an inner module taper. An undulator module was divided into four parts, each with different parameters: $K_1 = 1.6020$, $K_2 = 1.6021$, $K_3 = 1.6026$, and $K_4 = 1.6033$. This taper range, less than 1 % is easily achievable in Athos. All modules have the same undulator parameters, and the delays were maintained at 745 nm. The output is excellent, with the shortest average pulse duration being about **85 attoseconds**, as shown in Figure 7.5a. Better results can be achieved by further optimising the chicane delay between modules and the undulator taper within them.

As discussed in the first section, at $\lambda_r = 4$ nm, the pulse duration tends to increase within the module. It will be demonstrated that a positive taper of 16 % within the module can prevent an increase in pulse duration, thereby maintaining its brevity until the end of the module.

[I]Figure 7.4b is a courtesy of Marco Calvi.

Average Pulse Duration (FWHM) along z
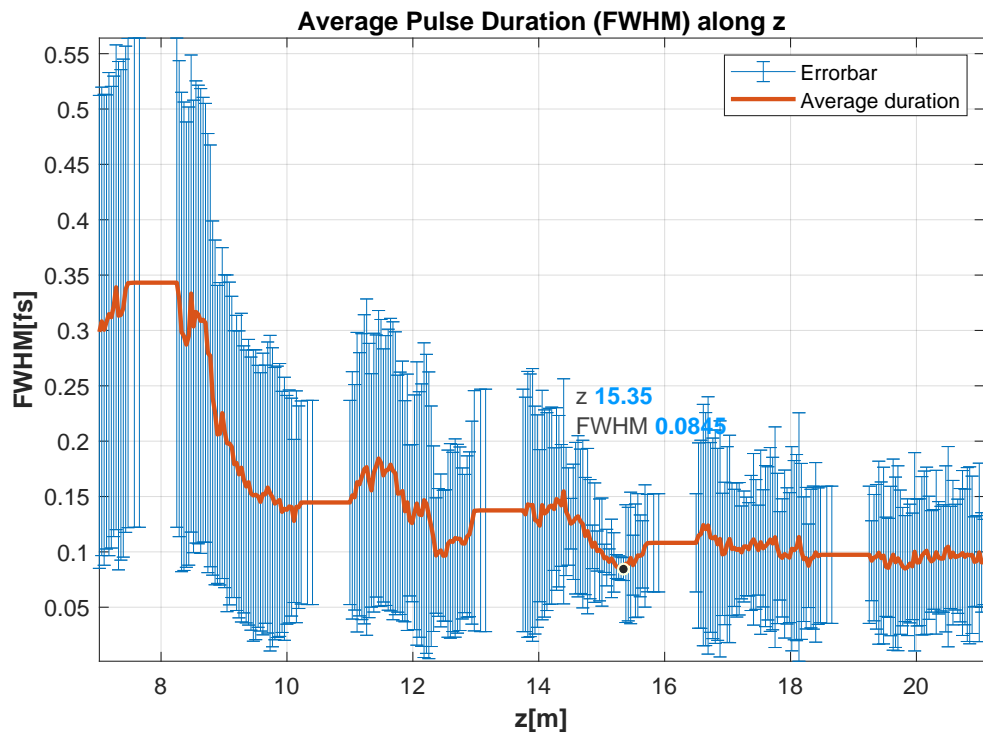
(a) Average pulse duration for $\lambda_r = 1$ nm.

FEL power at z = 15.35 m
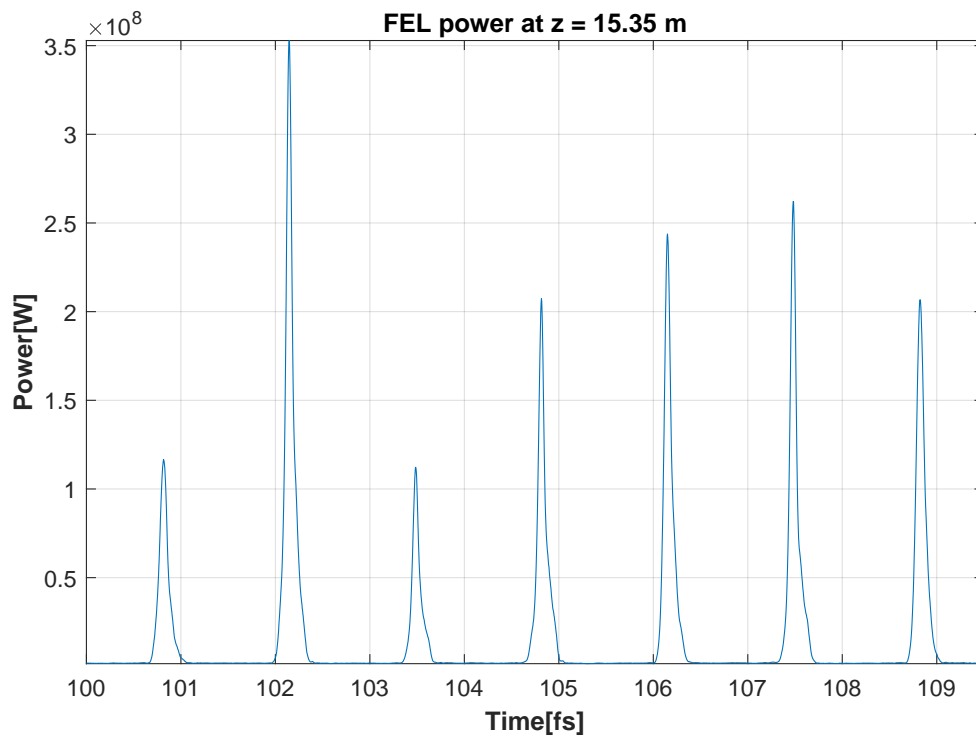
(b) Pulses at 15.35 m, with peak power of several hundred megawatts.

Figure 7.5: Average pulse duration for 1 nm with linear taper within the module. The average duration at z = 15.35 m is 85 as.

The demonstration simulation includes five undulator modules, as illustrated in Figure 7.6. The first four modules are configured with a constant K value of 2.884[II], meaning no taper is applied. This approach ensures the conclusion of the lethargy regime and facilitates observation of the direct effect of the strong taper in the fifth module.
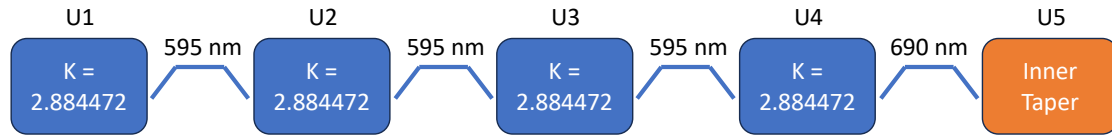
Figure 7.6: Simulation setup for demonstrating the effect of inner taper on pulse duration.

For the delay configuration, the first three delays are set to 595 nanometers, in line with the delay compensation within a module. This compensation was determined by a prior scanning study that identified the maximum pulse energy achievable at the end of the module. The delay in the fourth chicane was also scanned, revealing that the optimal value for maximum pulse energy in subsequent modules is 690 nanometers.

To simulate a linear taper within the fifth module, the undulator module, comprising 52 periods, was divided into 52 segments. The undulator parameters for each segment were individually set to follow a linear distribution. To identify an appropriate gradient for the linear taper, various gradients will be demonstrated, including:

- K = 2.9487 to K = 2.8195, corresponding to 4% electron energy difference.

- K = 3.0452 to K = 2.7221, corresponding to 10% electron energy difference. It is approximately the largest range Athos can provide at λ_r = 4nm.

- K = 3.1415 to K = 2.6243, corresponding to 16% electron energy difference.

The undulator parameter of 2.8845 represents the midpoint of the above gradients. The simulation comprises six sets, as each of the three slopes can be either positive or negative.

The results are presented in Figure 7.7, where taper ranges of 4 %, 10 %, and 16 % were tested. The positive 4 % taper had some effect, but the pulse duration still increased within the module. The positive 10 % taper is able to shorten the pulse duration further. Further investigation of the 16 % positive taper range (see Figure 7.7c) reveals that it can fully prevent the pulse duration from increasing again within the module.

[II]The constant K value is used in this simulation solely for demonstration purposes.
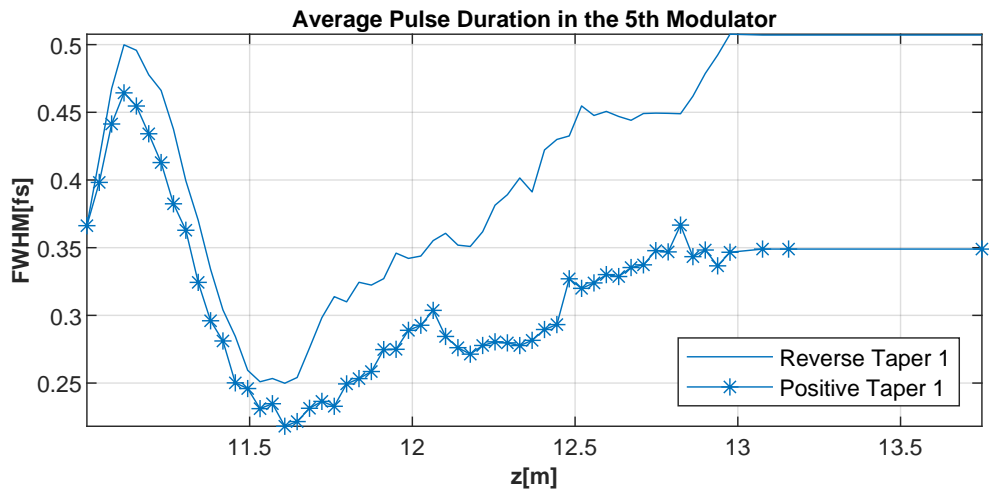
(a) 4% taper.
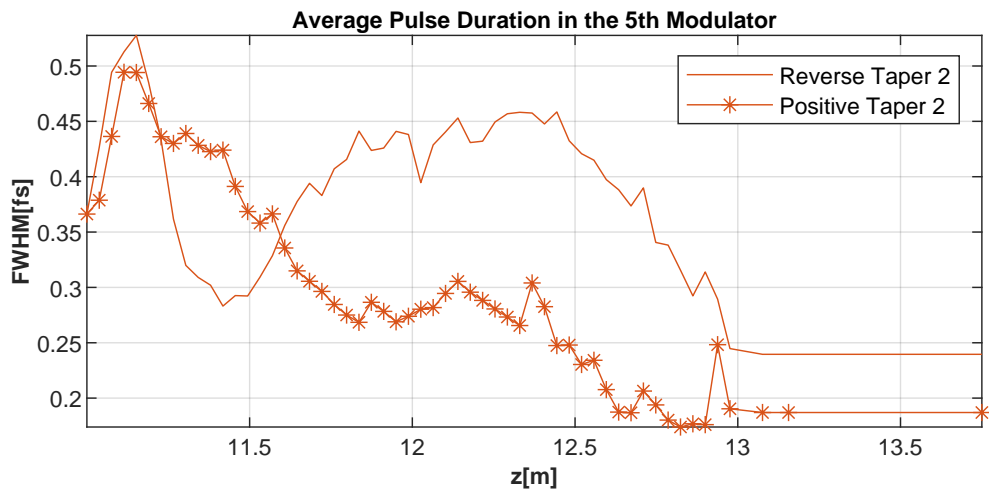
(b) 10% taper.
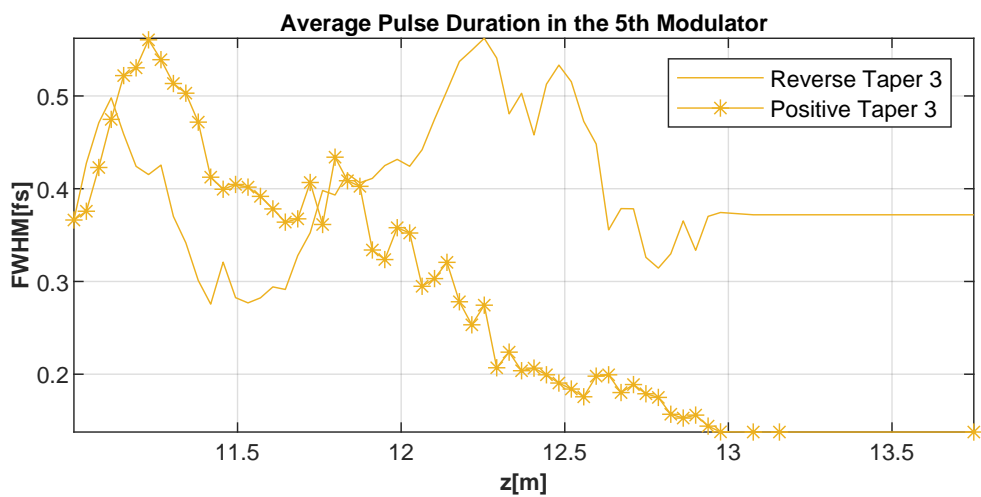
(c) 16% taper.

Figure 7.7: Comparison of average FWHM duration for different tapers. (More caption is available on the next page.)

Figure 7.7: The measured pulse duration in the 5th undulator module shows the strong taper's effect. Figure 7.7a shows the positive taper performs slightly better. However, due to the small taper range, both tapers can't stop the pulse duration from increasing within the module. In Figure 7.7b, with a larger taper range, the final duration improves compared to Figure 7.7a. Again, the positive taper performs better. In Figure 7.7c, the even larger taper range further improves the positive taper's result. However, the negative taper's result does not improve.

7.3   Simulation Setup

7.3.1   Beam Definition

The beam settings are aligned with those detailed in Chapter 4 for the ESASE simulation. The electron beam undergoes energy modulation at a wavelength of 800 nanometers, with a central energy denoted by $\gamma = 6653$. This modulation amplitude is set at 1%, resulting in a maximum energy variation of $\Delta\gamma_{max/min} = \pm66.53$. The energy spread of the beam is maintained at 501 keV, constituting a minimal 0.017% of the total beam energy. Furthermore, the beam is compressed to achieve a peak current of 8 kA. The advantages of using a current spike to facilitate mode-locking have been discussed in [91].

7.3.2   Undulator Setup

A significant positive taper is applied in each module of the undulator, with the undulator parameter K increasing from 2.6243 to 3.1415. Additionally, the delays are set to 595 nanometers. Figure 7.8 illustrates the dynamics of mode-locking with a strong taper.
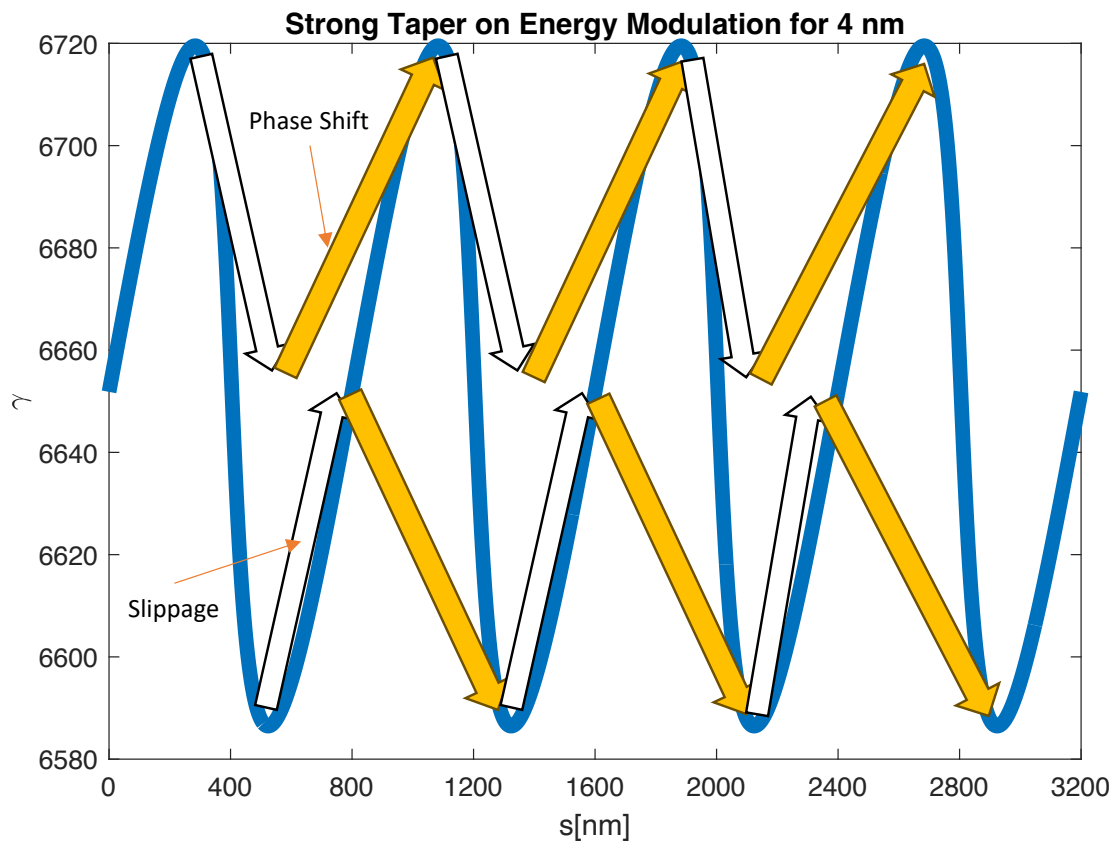
Figure 7.8: Mode-locking is employed in conjunction with a strong taper. The radiations, initiated at the top or bottom of the modulation, slide over the beam following the white arrows. Upon completion of a module, the delaying magnetic chicanes introduce an extra delay, as indicated by the yellow arrows. The total delay amounts to 800 nanometers in a single module.

7.4   Simulation Results and Analysis

7.4.1   Simulation Results

We will show the following simulation results:

1. Gain curve.

The FEL process reaches its saturation point after approximately nine modules, equating to a total length of about 25 meters. The saturation energy is around 10^{-4} joules. The FEL pulse energy increases rapidly between z = 15 m and z = 25 m, corresponding to modules 6-8. Within these modules, the energy rises quickly in the first half, then stabilises as it travels through the second half of each module.
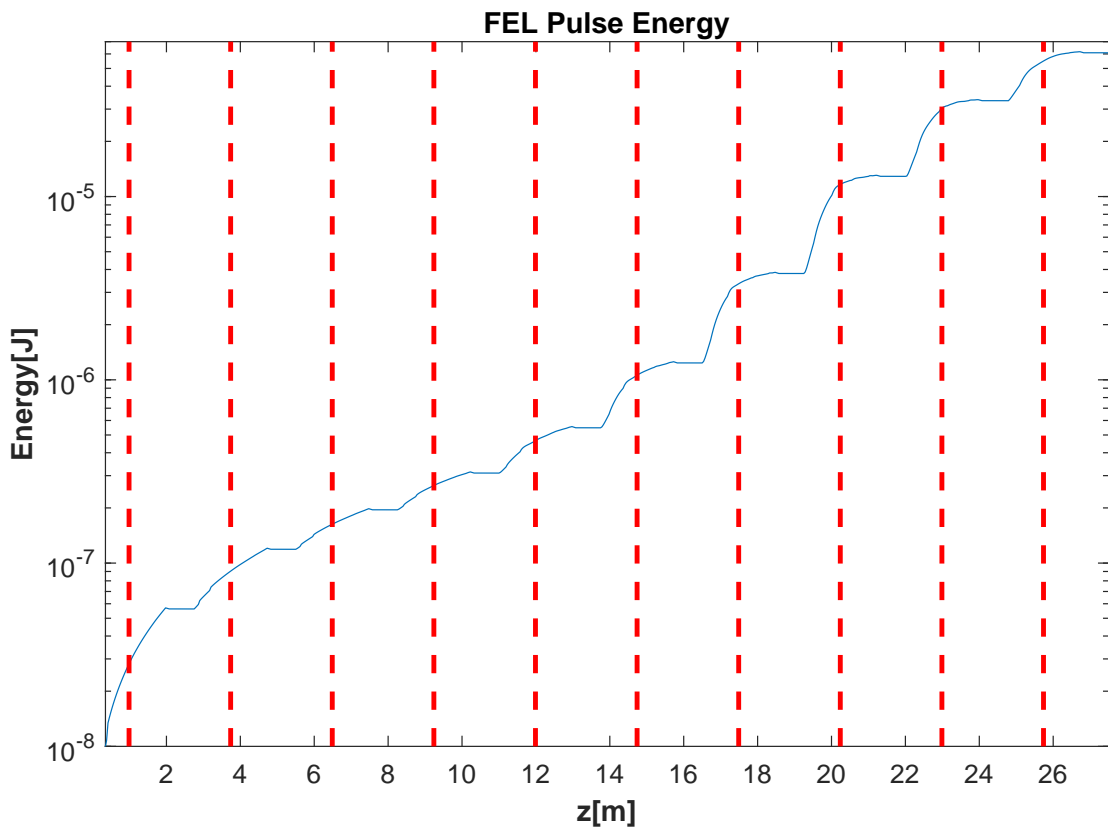
Figure 7.9: The gain curve is represented by the blue line, while the red lines mark the selected z positions, at which the FEL power is displayed in figures 7.11 (modules 1-5) and 7.12 (modules 6-10).

2. FEL power along wavelength and z-axis.

Figure 7.10 indicates that the first five modules exhibit a lower signal-to-noise ratio in a lethargic regime. Starting from the sixth module (at z = 13.75 m), the FEL spike becomes evident in every cycle. The spike consistently starts at a fixed position in each module, indicating that the delay is appropriately set for achieving mode-locking.
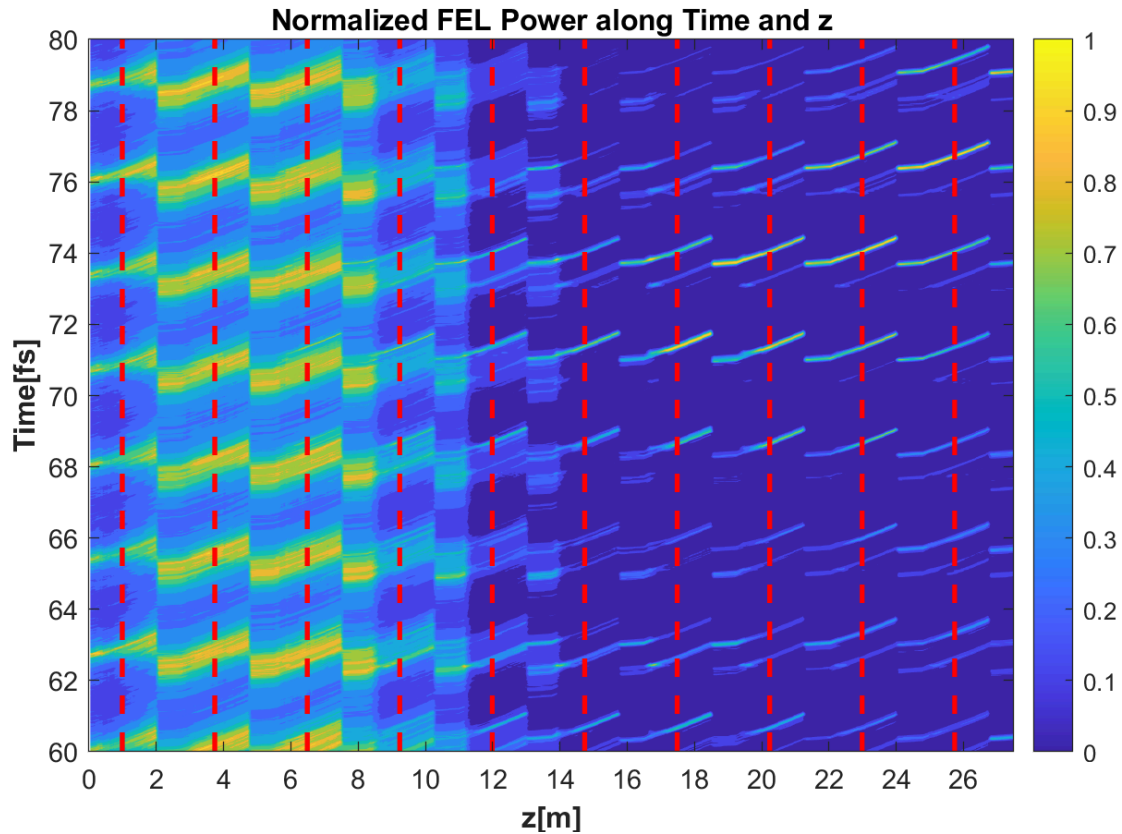
Figure 7.10: Normalized FEL power. The red lines mark the selected z positions, at which the FEL power is displayed in Figures 7.11 (modules 1-5) and 7.12 (modules 6-10).

3. FEL power at different z-positions

The positions selected are situated in the middle of each module. From the fifth module onwards, distinct and well-defined FEL pulses can be observed in some cycles. In modules 6 to 10, these pulses are fully amplified throughout each module, resulting in short and intense pulses that maintain their brevity until the end of each module.

Tuning the compression strength in the beam before sending it into the undulator could suppress the secondary pulses. However, further investigation is required.
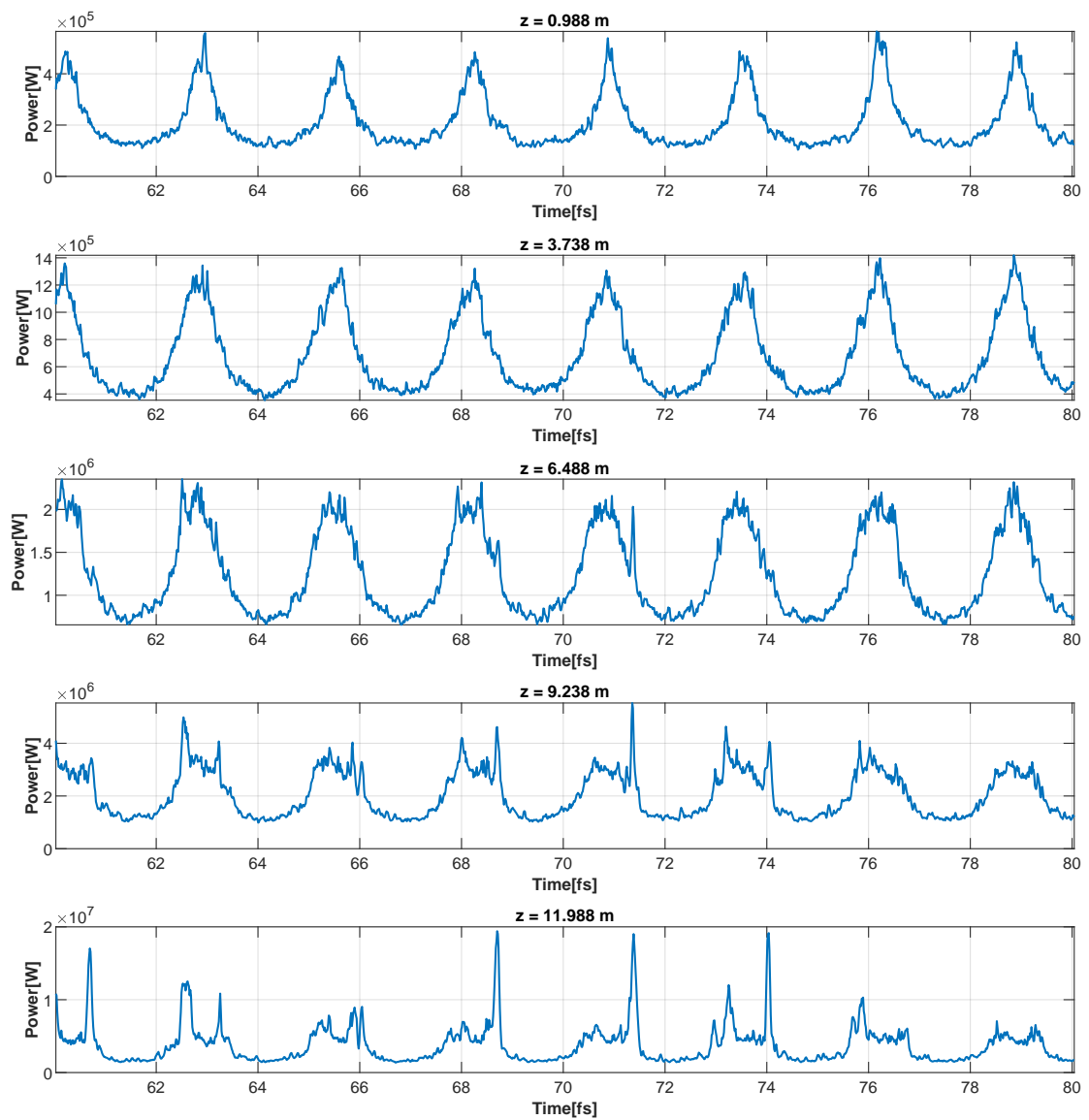
Figure 7.11: FEL power in modules 1-5. A short and intense spike appears to the right of the ESASE spike and is amplified along z.
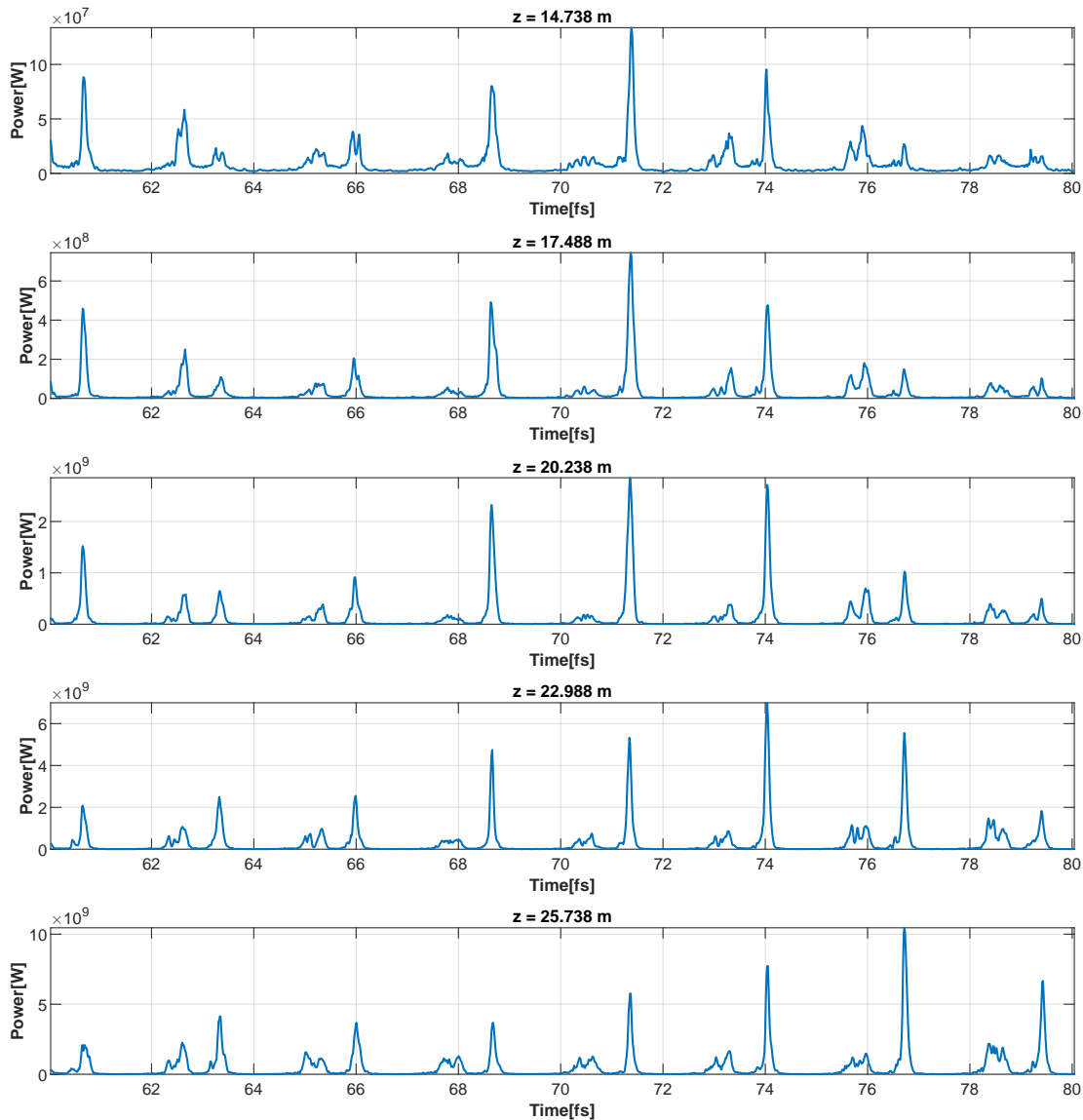
Figure 7.12: FEL power in modules 6-10. The spike is constantly amplified until saturation. Despite the delay control, the most intense spikes are not shifted across the modules between the module 6 and the module 8, suggesting that FEL pulse intensity is not the dominant factor, while bunching may be a more important factor in this dynamic.

4. Average pulse duration along the z-axis and the pulse structure at z = 23.62 m.

Pulse duration measurement starts at z = 7 m in module 3. The duration exceeds 1 fs in modules 3 and 4 and continuously decreases to 200 attoseconds in modules 5 and 6. The pulse duration does not decrease in module 7 but drops again in modules 8 and 9. In modules 8 and 9, the spikes on the right side of the current spikes become fully amplified and exceed the noise signal. At z = 23.62 m, the average duration is only **112.3 attoseconds**, a remarkable achievement considering the frequency of this radiation wavelength. The measurement
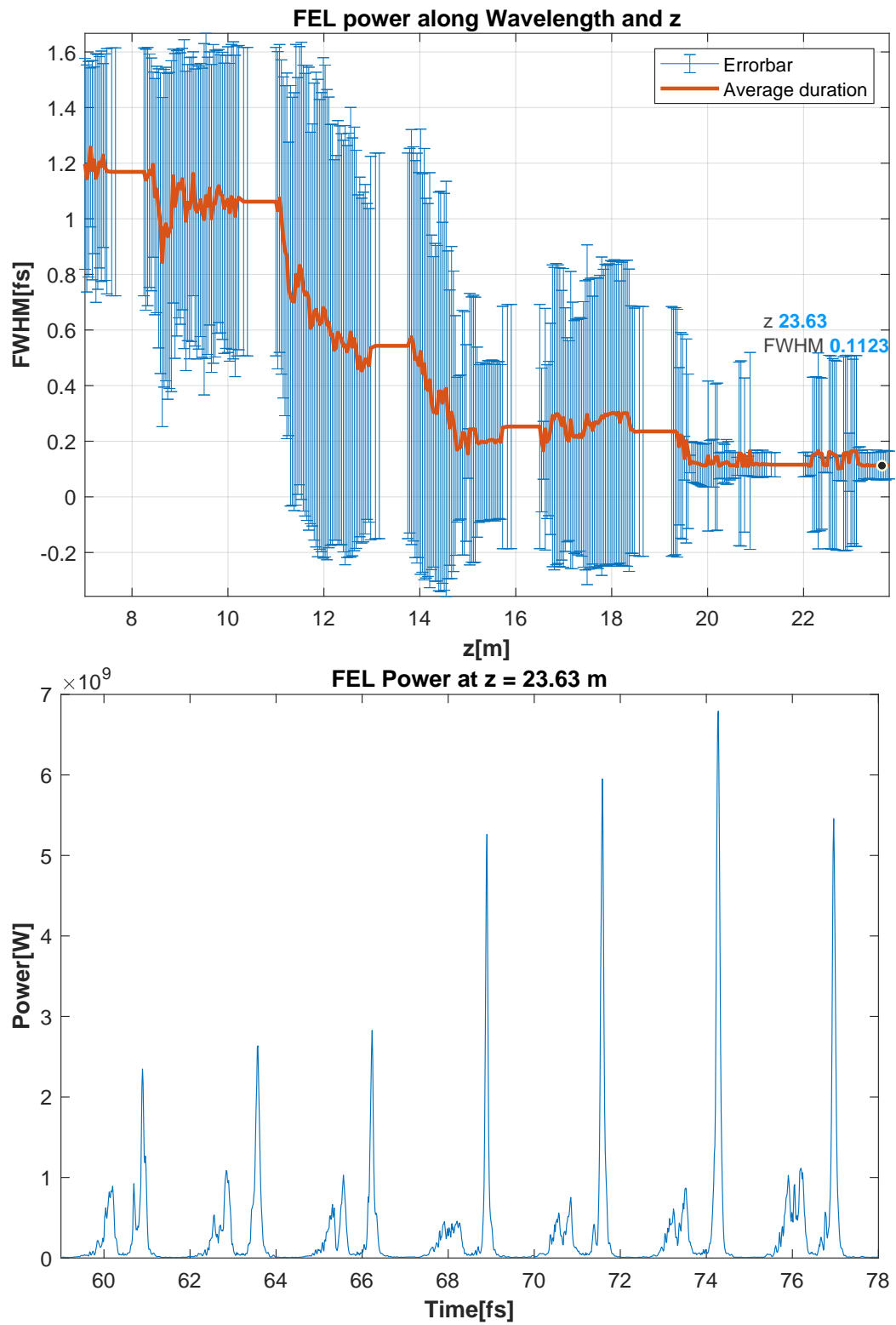
Figure 7.13: Average pulse duration (top) and pulse structure at z = 23.63 m (bottom). The errorbar in pulse duration measurement is derived from the MATLAB function 'errorbar'.

focuses on the primary pulse in each cycle of modulation, while the concurrent noise signal is neglected.

5. FEL power along wavelength and z-axis.
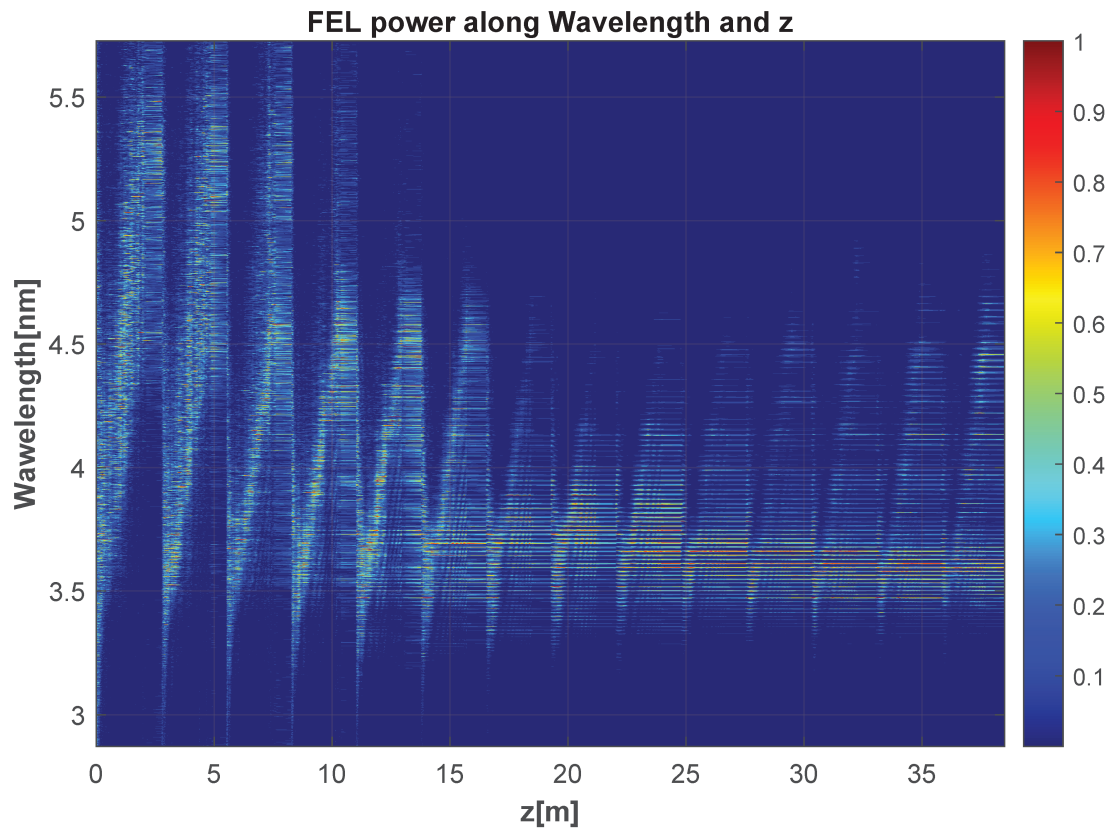
Figure 7.14: Normalised power along z and wavelength axis. The narrowest bandwidth is in the 8-th module (z = 19.25 m - 22 m).

A wide bandwidth is observed in modules 1-5. A frequency shift occurs in each module due to the large taper. Starting from the sixth module, the spectrum displays distinct and regular sidebands. As shown in Figure 7.12, the short pulses become clearly distinguishable starting from the sixth module. It can be concluded that the short pulses of 100 attosecond scale are a result of mode-locking with a large bandwidth. Towards the end of the ninth module (z = 24 m), the bandwidth is estimated to be around 20%, which is close to the taper range.

7.4.2 Simulation Result Analysis

The most significant conclusion from the simulation result is that the short pulse, averaging only 110 attoseconds at $\lambda_r = 4$ nm, is attributable to mode-locking with a large bandwidth spectrum. The large bandwidth is provided by the significant undulator taper. A notable

advantage of this method is the elimination of the need to consider any detuning parameters, as the SASE process is suppressed by the extremely large taper. The simulation results suggest that the dynamic of the section of the beam where FEL spikes are present corresponds to superradiance, as discussed in Appendix B. In superradiance, electrons are seeded by intense FEL pulses and lase at spontaneous frequencies. The radiation field is intensified and pulse duration is shortened.

In this analysis section, we further investigate two aspects: first, the spectrum of the 8th module, where the spectrum bandwidth is at its minimum, and second, the bunching factor and the energy spread.

1. **The spectrum with FEL pulse energy in the eighth undulator module (z = 19.25 m - 22 m).**

Figure 7.15 presents the spectrum alongside the FEL pulse energy in the 8th module. The pulse energy is plotted to observe the energy change during the lasing process, which helps us to better understand the spectrum. A key finding from Figure 7.15a is that energy exchange occurs throughout the undulator, despite the presence of a strong taper. The number of undulator periods has not been reduced, since energy exchange between electrons and radiation fields continues to occur.

(a) Spectrum with the pulse energy (red line).   (b) Spectrum with the energy change (red line).
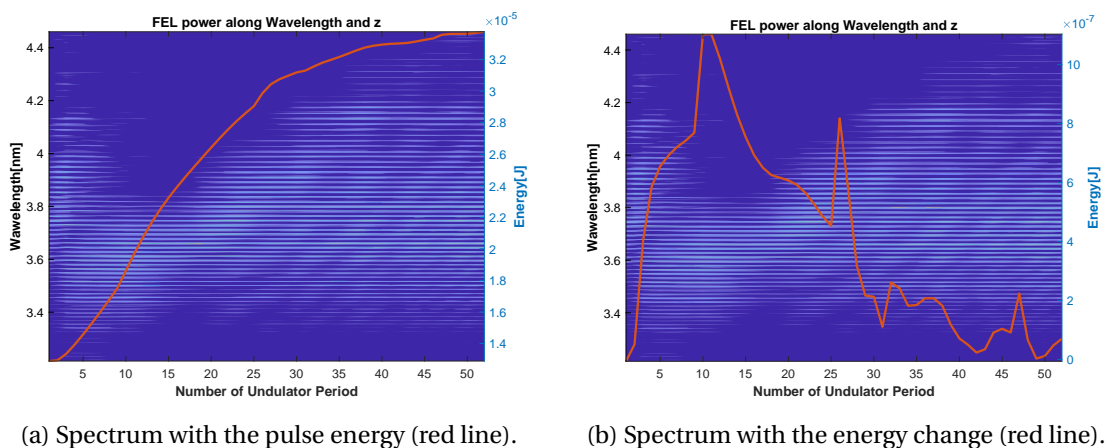
Figure 7.15: Spectrum in the 8th undulator module together with the FEL pulse energy (a), FEL pulse energy difference (b). The undulator number replaces the z-axis.

From $N_p = 0$ to $N_p = 10$, the initial energy change is minimal due to the effect of delay control, which allows FEL pulses to interact with new slices possessing distinct initial shot noise, and it takes several periods to recover the gain. From $N_p = 10$ to $N_p = 30$, the frequency shifts, with the FEL energy gain gradually decreasing. At $N_p = 26$, a sudden increase in energy change is observed in figure 7.15 (b). This increase is also observed in undulator 7 (not plotted), indicating that it is most likely not a noise signal. From $N_p = 30$ until the end of the module, the FEL gain remains at low levels, but not zero. A clear and distinctive sequence of dark lines is observable in the spectrum. It would be worth exploring potential connections between the lines and Figure 19 in Bonifacio's [92].

109

From N_p = 15 until the end of the module, the intensity of the various sidebands appears uniform despite a large taper. This may suggest that the FEL is lasing at its spontaneous frequency (mode with s = 0) as explained in Section B.3 in Appendix B.

2. **Bunching and energy spread**

Figure 7.16 shows that the FEL process is significantly inhibited in areas with spikes in energy spread. This is likely due to the significant energy gradient resulting from the density modulation in the beam. It has been observed that there is almost no bunching at the positions of the red spikes.

Due to the significant energy gradient, the bunching spikes (blue) to the left of the red spikes will slip into the area and experience attenuated gain. Meanwhile, the FEL spikes located to the right of the energy spread spikes (red) will not interact. Therefore, this part of the beam is more intense. We compressed the beam to enhance the suppression effect in this large energy gradient beam, which makes the spikes on the right side more intense than those on the left.

7.5   Conclusion

In this chapter, we begin by addressing the issue of FEL pulse duration for longer wavelengths than 1 nm, where the duration initially decreases and then increases within a module when mode-locking is present. Towards the end of the module, pulse durations of approximately 600 attoseconds are obtained, which are significantly longer than the minimum of 150 attoseconds. To tackle this challenge, the introduction of a substantial undulator taper within the module is proposed as a solution. The linear taper within the undulator module is achieved by rotating a transverse gradient undulator. Based on demonstration simulations, using a taper range of 16% is expected to prevent an increase in pulse duration within the module. Ultimately, we achieve an exceptionally short pulse duration, averaging around 110 attoseconds.

Due to the wide range of K and the varying resonant beam energy, the model falls outside the scope of steady-state analysis. As a result, it becomes challenging to explain the phenomenon within conventional theoretical models. To further study this model, from a dynamic perspective, it is necessary to first understand the underlying cause of the short pulse generation. Full comprehension of the spectrum in figure 7.15 is necessary, including the significant increase in energy change at N_p = 26 and the broad spectrum bandwidth after N_p = 26. Furthermore, optimization of the density modulation profile could potentially reduce the size of the secondary spikes.

Upon conducting a comprehensive analysis of the simulation results, we attribute the generation of these short pulses to the broad spectrum produced by the significant taper when combining the mode-locking. The final pulse power reaches several gigawatts, maintaining a high level. Optimisation at this radiation wavelength has largely enhance the FEL performance, thus open up new opportunities for related experiments.
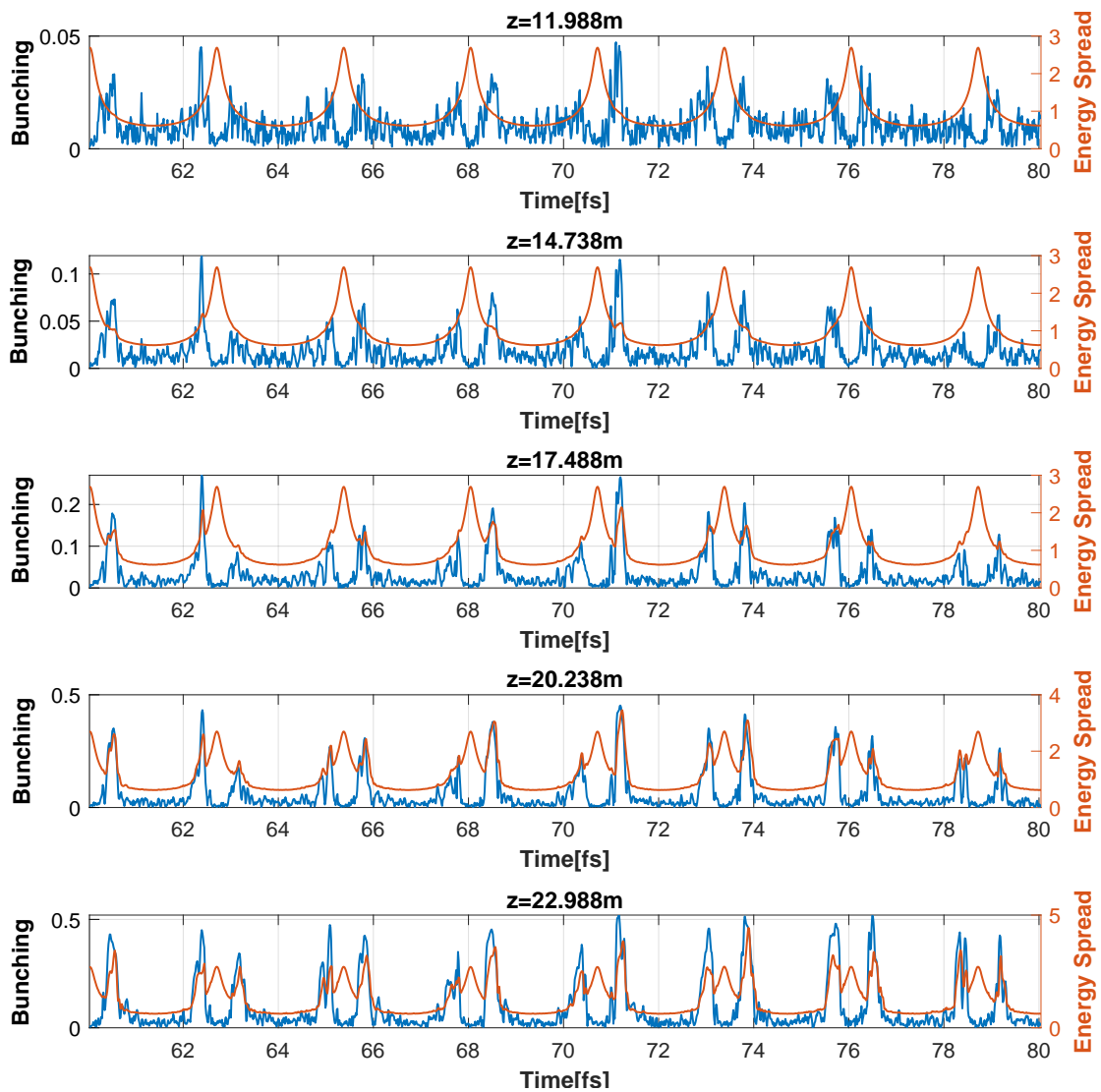
Figure 7.16: Bunching (blue) and Energy Spread (red) at different z-positions. In most cycles, the energy spread is more intense on the right side of the current spike than on the left. This could be because spikes on the right side do not slide into the current spikes, where the energy change is significant.

To validate this technique in experiments, it is important to consider that the trajectory of the electron beam inside the module is not a straight line. This presents several engineering challenges, such as the fluctuation in the undulator parameter and calibration of the beam.

8 Summary and Conclusion

The numerical studies in this thesis have successfully demonstrated the generation of the attosecond pulses at the Athos beamline of the SwissFEL facility. The simulation results confirm that certain configurations on the Athos undulator are beneficial for generating pulses of 100 attosecond scale, covering a radiation frequency range from λ_r = 1 nm to 4 nm. The combination of high intensity, high photon energy and short pulse duration allows the study of electron dynamics with nonlinear X-ray spectroscopy and single particle imaging [22].

We note that isolated intense pulses are more widely used in experiments than those in the train form. The isolated pulses can be achieved by applying unequal delays to the beam with unequal-spaced peak currents. Such beams can be generated using chirped seeding lasers. It is important to note that the two techniques are not separate. The PhD project focuses on the fundamental question of the dynamics of generating short pulses and their duration, the discussion in this study is helpful for generating both pulse trains and single pulses.

As a review of the thesis. First, we briefly introduce the FEL theory, providing a basis for understanding the simulation results. Then, we explore the temporal nature of SASE, where slippage and its negative effects on generating short pulses are discussed. Since the slippage effect is particularly evident in the soft X-ray range, several methods have been proposed, namely Enhanced SASE (Chapter 4), slicing (Chapter 5), mode locking (Chapter 6), and a linear taper within the undulator module (Chapter 7).

In Chapter 4, the Enhanced SASE method aims to use a density-modulated electron beam, such as one with a current spike, to generate short pulses. For λ_r = 1 nm, we have generated a train of pulses with a typical duration of 500 attoseconds. Then, Chapter 5 describes the slicing method, which maintains resonance in the beam section where FEL pulses are present, by applying an undulator taper. The slicing method's simulation results yield an average pulse duration of **200 attoseconds**, forming distinct and clean train spikes. Ultimately, in the saturation regime, where we implemented a strong taper to enhance FEL energy, it was discovered that the radiation frequency remains constant. In Chapter 6, the mode-locking technique was demonstrated through the application of delay control using magnetic chicanes in the

intermodular sections of the undulator. By integrating this delay control with the modulated energy beam, the resultant pulses exhibited mode-locking, consistent with the clearly observable sidebands in the spectrum. The simulation findings illustrate an average pulse duration of about **100 attoseconds** at a radiation wavelength of 1 nm, exceeding the cooperation length threshold. We conducted a study to investigate the reasons for the reduced saturation energy. One important consideration is the optical klystron effect, which causes a noticeable gap to occur between FEL pulses and bunching spikes, leading to a significant reduction in lasing performance during the late linear regime. In Chapter 7, the rotated Transverse Gradient Undulator (TGU) was included, which creates a linear taper within the undulator module. The initial optimisation was based on the mode-locking mode at a radiation wavelength of 1 nm, resulting in a pulse duration of approximately **85 attoseconds**. Subsequently, we applied this model at 4 nm radiation wavelengths. This simulation optimisation presented a major challenge due to a cooperation length of approximately 600 attoseconds, causing the pulse duration to increase again within the module. Nonetheless, the integration of an undulator module with a substantial taper allowed us to accomplish shorter pulses, averaging just **110 attoseconds** until the end of the module.

Comparing the three methods in Chapters 5, 6, 7

The slicing method offers short pulses, up to 100 GW saturation power and relatively low shot noise effects in the beam. However, it has the disadvantage of requiring precise adjustment of each undulator parameter, which can be very difficult in experiments. Mode-locking in the FEL has the advantage of producing cleaner and shorter pulses compared to the slicing method, with pulse duration below the cooperation length limit. It requires only one undulator parameter and delay adjustment, which makes it easier to implement. However, it has the disadvantage of very low saturation power. The addition of the rotated TGU configuration has the effect of reducing the pulse duration for both 1 nm and 4 nm radiation wavelengths, although the underlying mechanism is not the same. A disadvantage is that the realisation of the TGU on the instrument is subject to many uncertainties, such as undulator errors and the deflected trajectory of the electron beam.

Consideration of the implementation of methods in the machine

We give a very brief summary of the factors that could influence the final results in real experiments, such as the residual energy chirp in the beam, the uncalibrated phase shifters, the tolerance error in the delay calibration of the CHIC chicanes, the phase shifter errors, the phase error in the seeding laser, the space charge effect, etc. Experimentally, the most appropriate method is determined on a case-by-case basis. The simulation results presented in this thesis are very useful for instrumental experiments due to the detailed discussion of the pulse generation mechanism.

A Laplace Techniques for Integro-Differential Equation Solutions

The Laplace transform is a powerful tool for solving many mathematical problems. This chapter in the appendix aims to exemplify the utilisation of the Laplace methodology in addressing a specific form of integrodifferential equation. We will consider Equation 2.82.

A.1 Normalization of the Equation

We have the equation from 2.82

$$\frac{d\tilde{E}_x}{dz} = -\frac{e^2 n_0 \mu_0 K[JJ]}{4\gamma_0^2 m_e} \int \frac{dF(\eta)}{d\eta} d\eta \int_0^z \left[\frac{K[JJ]\tilde{E}_x(z)}{2\gamma_0} - \frac{i4\gamma_0 c}{\omega_0 K[JJ]} \frac{d\tilde{E}_x(z)}{dz} \right] e^{i2k_u(\eta+\Delta)(z'-z)} dz'$$

(A.1)

To solve the given equation using Laplace techniques, we first rewrite the equation in a more compact form for ease of readability. In the theory chapter, we define two parameters:

$$G = \left[\frac{\mu_0 K^2 [JJ]^2 j_0 k_u e}{4\gamma_0^3 m_e c} \right]^{\frac{1}{3}}, \quad k_p^2 = \frac{2\mu_0 j_0 k_u e}{\omega_0 \gamma_0 m_e}$$

(A.2)

Substituting both parameters into Equation A.1, and noting that $j_0 \simeq ecn_0$, Equation A.1 becomes

$$\frac{d\tilde{E}_x}{dz} = \int \frac{dF(\eta)}{d\eta} d\eta \int_0^z \left[-\frac{G^3}{2k_u} \tilde{E}_x(z) + i\frac{k_p^2}{2k_u} \frac{d\tilde{E}_x(z)}{dz} \right] e^{i2k_u(\eta+\Delta)(z'-z)} dz'$$

(A.3)

Another important step involves normalising the variables.

$$\hat{\eta} = \frac{2k_u}{G}\eta = \frac{1}{\rho}\eta, \qquad \hat{\Delta} = \frac{1}{\rho}\Delta, \qquad \hat{z} = Gz, \qquad \hat{P} = \frac{k_p^2}{G^2}$$

(A.4)

By incorporating A.4 into Equation A.3, we obtain the following expression:

$$\frac{d\tilde{E}_x}{d\hat{z}} = \int \frac{dF(\hat{\eta})}{d\hat{\eta}} d\hat{\eta} \int_0^{\hat{z}} \left[\tilde{E}_x(\hat{z}) + i\hat{P}\frac{d\tilde{E}_x(\hat{z})}{d\hat{z}} \right] e^{i(\hat{\eta}+\hat{\Delta})(\hat{z}'-\hat{z})} d\hat{z}' \tag{A.5}$$

Examining this equation clarifies why the Gain parameter is expressed as a cube during the normalisation process. The left side of the Equation A.5 indicates the electric field, signified by $d\tilde{E}_x/d\hat{z}$. Meanwhile, the right side of the equation contains two terms: $d\hat{\eta}$ signifies modulation, and the integration of $d\hat{z}'$ from 0 to $\hat{z}$ denotes the growth in the bunching factor up to the current position $\hat{z}$. Each of these terms cancels out one G. Therefore, the Gain parameter is generally presented in cubic form.

A.2 Laplace Transformation

The Laplace transform is a mathematical tool that assists in solving ordinary differential equations. It converts the provided equations, usually in the time domain, into an algebraic equation in the Laplace domain. By solving the transformed equation in the Laplace domain, we can determine a solution, which, afterwards, can be reconverted to the time domain using the inverse Laplace transform.

The Laplace transformation of the field $\tilde{E}_x(z)$ is

$$\mathscr{L}\left[\overline{E}(\hat{z})\right] = \int_0^\infty e^{-s\hat{z}} \tilde{E}(\hat{z}) d\hat{z} \tag{A.6}$$

When $\Re(s) > 0$, for left side of A.5,

$$\int_0^\infty e^{-s\hat{z}} \frac{d\tilde{E}(\hat{z})}{d\hat{z}} d\hat{z} = s\overline{E}(s) - \tilde{E}(0), \tag{A.7}$$

where $\tilde{E}(0)$ can be regarded as the field at the entrance. For the right side of A.5, applying Laplace transformation yields,

$$\int_0^\infty e^{-s\hat{z}} d\hat{z} \int \frac{dF(\hat{\eta})}{d\hat{\eta}} d\hat{\eta} \int_0^{\hat{z}} \left[\tilde{E}_x(\hat{z}) + i\hat{P}\frac{d\tilde{E}_x(\hat{z})}{d\hat{z}} \right] e^{i(\hat{\eta}+\hat{\Delta})(\hat{z}'-\hat{z})} d\hat{z}' \tag{A.8}$$

$$= \int \frac{dF(\hat{\eta})}{d\hat{\eta}} d\hat{\eta} \int_0^\infty \left[\tilde{E}_x(\hat{z}) + i\hat{P}\frac{d\tilde{E}_x(\hat{z})}{d\hat{z}} \right] e^{i(\hat{\eta}+\hat{\Delta})\hat{z}'} d\hat{z}' \int_{\hat{z}'}^\infty e^{-(s+i\hat{\eta}+i\hat{\Delta})\hat{z}} d\hat{z} \tag{A.9}$$

$$= \int \frac{dF(\hat{\eta})}{d\hat{\eta}} d\hat{\eta} \cdot \left[\overline{E}(s) + i\hat{P}\left(s\overline{E}(s) - \tilde{E}(0) \right) \right] \cdot \frac{1}{s+i\hat{\eta}+i\hat{\Delta}} \tag{A.10}$$

$$= \int \frac{dF(\hat{\eta})/d\hat{\eta}}{s+i\hat{\eta}+i\hat{\Delta}} d\hat{\eta} \left[\overline{E}(s) + i\hat{P}\left(s\overline{E}(s) - \tilde{E}(0) \right) \right] \tag{A.11}$$

Having used the linearity property of the Laplace transform to simplify the transformed

equation, we now bridge the left side and the right side into one equation, and it becomes

$$s\overline{E}(s) - \tilde{E}(0) = \hat{D}(s)\left[\overline{E}(s) + i\hat{P}\left(s\overline{E}(s) - \tilde{E}(0)\right)\right] \tag{A.12}$$

where

$$\hat{D}(s) = \int \frac{dF(\hat{\eta})/d\hat{\eta}}{s + i\hat{\eta} + i\hat{\Delta}} d\hat{\eta} \tag{A.13}$$

is dispersion parameter. If we assume the entrance field to be real and positive, i.e. $\tilde{E}(0) = E(0)$, then the solution $\overline{E}(s)$ to the equation A.12 is

$$\overline{E}(s) = E(0)\left[s - \frac{\hat{D}(s)}{1 - i\hat{P}\hat{D}(s)}\right]^{-1} \tag{A.14}$$

A.3   Inverse Laplace Transformation

The Laplace transform represents a system's behavior in the frequency domain. The inverse Laplace transform, on the other hand, converts this representation back into the time domain.

The inverse Laplace transform is calculated using the Bromwich integral,

$$f(t) = \frac{1}{2\pi i}\int_{\gamma - i\infty}^{\gamma + i\infty} f(s)e^{st}ds, \tag{A.15}$$

where $f(s)$ is the Laplace transform of the analysed system, t is the time variable, γ is a real constant such that the Laplace transform $f(s)$ is absolutely convergent for $\mathrm{Re}(s) > \gamma$, and j is the imaginary unit. The integration is performed along the Bromwich contour in the complex plane. The Bromwich integral is used to compute the inverse Laplace transform of the equation, which provides information about its response to inputs in the time domain.

Substituting the equation A.14 into A.15 gives

$$E(\hat{z}) = \frac{1}{2\pi i}\int_{\gamma - i\infty}^{\gamma + i\infty} E(0)\left[s - \frac{\hat{D}(s)}{1 - i\hat{P}\hat{D}(s)}\right]^{-1} e^{st}ds \tag{A.16}$$

The equation has a singularity if

$$s - \frac{\hat{D}(s)}{1 - i\hat{P}\hat{D}(s)} = 0 \tag{A.17}$$

Also, as $|s|$ approaches infinity, the coefficient before e^{st} tends to zero, so we can use Cauchy's residue theorem to solve the equation. The result can be expressed as a superposition of

Bromwich-Hankel Integration Path
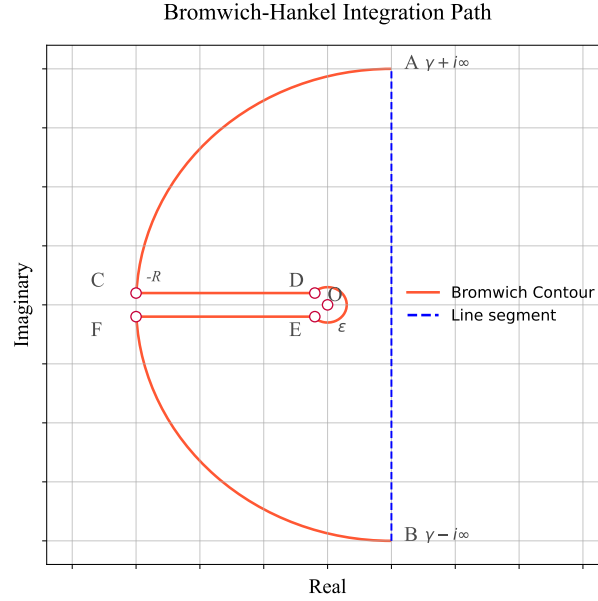
Figure A.1: The Bromwich-Hankel Integration Path illustrating the contour used for inverse Laplace transforms. The contour consists of line segments CD and EF, circular arcs A to C and F to B, and a small loop around the origin (O). The gamma line (dashed blue) represents the real part of the complex plane, with the integration path moving from $\gamma + i\infty$ to $\gamma - i\infty$. The line segments at the left end of the contour represent the limits of integration as R approaches infinity and ϵ approaches zero.

partial waves. The first-order differential of the left side in the equation A.17 is

$$\frac{d}{ds}\left[s - \frac{\hat{D}(s)}{1 - i\hat{P}\hat{D}(s)} \right] \tag{A.18}$$

$$= 1 - \left[\frac{1}{1 - i\hat{P}\hat{D}(s)} \frac{d\hat{D}(s)}{ds} + \frac{i\hat{P}\hat{D}(s)}{(1 - i\hat{P}\hat{D}(s))^2} \frac{d\hat{D}(s)}{ds} \right] \tag{A.19}$$

$$= 1 - \left[\frac{1 - i\hat{P}\hat{D}(s) + i\hat{P}\hat{D}(s)}{(1 - i\hat{P}\hat{D}(s))^2} \frac{d\hat{D}(s)}{ds} \right] \tag{A.20}$$

$$= 1 - \frac{1}{(1 - i\hat{P}\hat{D}(s))^2} \frac{d\hat{D}(s)}{ds} \tag{A.21}$$

The radiation amplitude is therefore

$$E(\hat{z}) = E(0) \sum_{k=1}^{n} e^{s_k \hat{z}} \left[1 - \frac{\hat{D}(s_k)'}{(1 - i\hat{P}\hat{D}(s_k))^2} \right]^{-1} \tag{A.22}$$

where s_k represents the k-th root of the equation, and the notation $\hat{D}(s_k)$ and $\hat{D}(s_k)'$ denote respectively $\hat{D}(s)$ and $\hat{D}(s)'$ for the k-th root.

A.4   Determination of Equation Roots s_k

To obtain a definite solution for E(z), it is necessary for us to determine all the roots of the equation, s_k. We assume that the energy spread of the electron beam is very small, i.e. $F(\hat{\eta}) = \delta(\hat{\eta})$, so that the function D becomes

$$\hat{D}(s) = i(s + i\hat{\Delta})^{-2} \tag{A.23}$$

Substituting equation A.23 into equation A.17 yields

$$s - \frac{i}{(s + i\hat{\Delta})^2 + \hat{P}} = 0, \tag{A.24}$$

simplifying it gives

$$s^3 + 2i\hat{\Delta}s^2 + (-\hat{\Delta}^2 + \hat{P})s - i = 0, \tag{A.25}$$

the left side of the equation A.24 is the coefficient of $e^{s\hat{z}}$, and it converges to 0 as $|s| \to \infty$. So, it satisfies for applying the Cauchy residue theorem, and then

$$\tilde{E}(\hat{z}) = E(0) \sum_{k=1}^{3} \frac{e^{s\hat{z}}}{1 - 2i(s_k + i\hat{\Delta})s_k^2} \tag{A.26}$$

The equation A.25 has three roots because it is a cubic equation. According to the fundamental theorem of Algebra, in the complex number system, every polynomial equation of degree n has precisely n roots, taking multiplicities into account. Likewise, every cubic polynomial can be factored into linear factors, indicating that it must possess three roots. These three roots follow to Vieta's formulas:

$$s_1 s_2 s_3 = i, \qquad s_1 s_2 + s_2 s_3 + s_1 s_3 = -\hat{\Delta}^2 + \hat{P}, \qquad s_1 + s_2 + s_3 = -2i\hat{\Delta} \tag{A.27}$$

and it gives the final solution of the equation A.26 as:

$$\tilde{E}(\hat{z}) = E(0) \left[\frac{s_2 s_3 e^{s_1 \hat{z}}}{(s_1 - s_2)(s_1 - s_3)} + \frac{s_1 s_3 e^{s_2 \hat{z}}}{(s_2 - s_1)(s_2 - s_3)} + \frac{s_1 s_2 e^{s_3 \hat{z}}}{(s_3 - s_1)(s_3 - s_2)} \right] \tag{A.28}$$

For the most simple case, where we suppose the electrons are all in resonance and ignore the space charge effect, e.g., $\hat{\Delta} = 0, \hat{P} = 0$, we obtain the roots as

$$s_1 = \frac{1}{2}(i + \sqrt{3}), \quad s_2 = \frac{1}{2}(i - \sqrt{3}), \quad s_3 = -i \tag{A.29}$$

the form of $\tilde{E}(\hat{z})$ is

$$\tilde{E}(\hat{z}) = \frac{E_0}{3} \left[e^{\frac{1}{2}(i + \sqrt{3}\hat{z})} + e^{\frac{1}{2}(i - \sqrt{3}\hat{z})} + e^{-i\hat{z}} \right] \tag{A.30}$$

which is the same as in 2.66.

B Dynamics of FEL Pulses Sliding into Fresh Slices

In this appendix chapter, we discuss the dynamics when an intense FEL pulse slips into a fresh slice of the beam, a phenomenon known as superradiance.

The appendix chapter serves to provide an explanation for the phenomenon observed in the slicing chapter (see Figure 5.18 in Chapter 5), where the radiation's frequency remains consistent despite the use of a larger taper. This cannot be explained by the resonance condition alone. The dynamics underlying this phenomenon are consistent with the descriptions found in [92], which provide a possible theoretical framework.

B.1   Separated Integral Variables

First, since there is evident slippage, it is necessary to separately consider the integration of the distances traveled by the FEL pulses and the electrons, using the integrating variables $\hat{z}$ and $\hat{z}_1$ as defined in [93].

$$\hat{z}_1 = \frac{1}{l_c}(\overline{z} - c\overline{\beta}_z t), \qquad \hat{z}_2 = \frac{1}{l_c}(c t - \overline{z}), \tag{B.1}$$

where l_c represents the cooperation length. The variable z denotes the position of the FEL pulse. The constant c is the speed of light, while $c\overline{\beta_z}$ is the average longitudinal velocity of the electron. $\hat{z}_1$ will be used as a scaled coordinate in the electron bunch. Note that the combined distance of $\hat{z}_1$ and $\hat{z}_2$ represents the difference between the electron's distance and the light path, so that

$$\hat{z} = \hat{z}_1 + \hat{z}_2 \tag{B.2}$$

B.2   Solving Differential Equations with the Separated Integral Variables

The dimensionless FEL equations can be found in [92, 24]:

$$\frac{\partial B}{\partial \hat{z}} = i\mathscr{P} \qquad \text{(B.3a)}$$

$$\frac{\partial \mathscr{P}}{\partial \hat{z}} = -E \qquad \text{(B.3b)}$$

$$\frac{\partial E}{\partial \hat{z}} + \frac{\partial E}{\partial \hat{z}_1} = B + i\Delta E \qquad \text{(B.3c)}$$

where $B = \sum_{i=1}^{N} \exp(-i\theta)$ is the bunching factor, and θ is the ponderomotive phase. $\mathscr{P}$ is the collective momentum, defined as $\mathscr{P} = \sum_{j=1}^{N} \frac{\gamma_j - \gamma_0}{\rho\gamma_0} \exp(-i\theta)$. To simplify the calculations, we ignore the space charge effect but retain the detuning parameter Δ, as it remains important in subsequent discussions.

We employ the Laplace transform to solve the partial differential equation B.3c, the method has been introduced in Appendix A. The outcome in the Laplace domain for the left side of equation B.3c can be written as

$$E(s, \hat{z}_1) = E_{\text{ss}}(s) + E_1(s, \hat{z}_1), \tag{B.4}$$

where the $E(s, \hat{z}_1)$ is the total electric field in the Laplace domain. $E_{\text{ss}}(s)$ represents the results over differential item $\frac{\partial E}{\partial \hat{z}}$ in the steady state, where we get from the integration over $\hat{z}$. $E_1(s, \hat{z}_1)$ is the result integrated over $\hat{z}_1$. The relation between the $E_{\text{ss}}(s)$ and $E_1(s, \hat{z}_1)$ is given in [92] as

$$E_1(s, \hat{z}_1) = \exp\left(-\frac{s^3 - \Delta s^2 + 1}{s^2}\hat{z}_1\right)E_{\text{ss}}(s) \tag{B.5}$$

The subsequent process involves transferring Laplace domain results to the time domain. Regarding the steady-state result $E_{\text{ss}}(\hat{z})$, we have the result as the sum of three exponential elements corresponding to the residues over three singularities (see Eq. A.26 in Appendix B). For $E_1(\hat{z}, \hat{z}_1)$, we perform an inverse Laplace transformation, and the result can be found in [92] as :

$$E_1(\hat{z}, \hat{z}_1) \propto \oint_C \frac{s}{s^3 - \Delta s^2 + 1} \exp\left[is(\hat{z} - \hat{z}_1) - i\frac{\hat{z}_1}{s^2}\right] ds \tag{B.6}$$

C is the integration contour.

The behavior of the electric field E can be categorized based on the relationship between $\hat{z}_1$
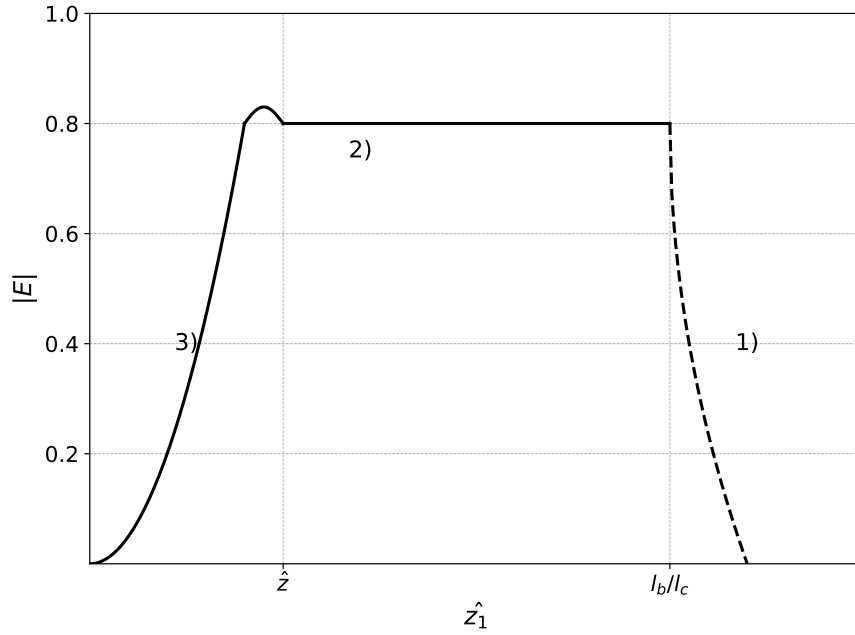
Figure B.1: Radiation field amplitude depending on $\hat{z}_1$ in the superradiance dynamics.

and the ratio l_b/l_c, corresponding to different regions in figure B.1[I]:

- Region 1 ($\hat{z}_1 > l_b/l_c$):

    When $\hat{z}_1$ is significantly large, such that it lies entirely outside the electron bunch, the FEL pulses can not continue to grow due to the absence of a source. Consequently, the electric field E stays constant.

- Region 2 ($\hat{z} < \hat{z}_1 < l_b/l_c$):

    In this scenario, the integration contour runs parallel to the real axis, with every singularity positioned outside of it. As all singularities are external to the integration path, the integral's result is null ($E_1 = 0$). Therefore, the outcome is equivalent to the steady-state result, leading to $E = E_{ss}$.

- Region 3 ($\hat{z}_1 < \hat{z}$) :

    A smaller $\hat{z}_1$ value suggests that the emitted FEL pulses stay close to the resonant electrons. Here, the singularities are within the integration contour C. The cubic equation's three singularity poles contribute to the integral's result. These poles are the same as those in the steady-state field and hence will cancel each other out. The only significant term is the essential singularity at $s = 0$. The electric field E in this case is

---

[I]We keep the method in [92], while an alternative discussion method can be found in [8] starting with equation 5.71, using stationary phase approximation.

determined by the contribution of this essential singularity.

$$E_{SR}(\hat{z}, \hat{z}_1) \propto \oint_{C_0} \frac{s}{s^3 - \Delta s^2 + 1} \exp\left[i s(\hat{z} - \hat{z}_1) - i \frac{\hat{z}_1}{s^2} \right] ds \tag{B.7}$$

It is important to note that C_0 differs from C as mentioned in equation B.6. The contour C_0 represents a counterclockwise trajectory that exclusively encompasses the singularity at $s = 0$. As a result of this specific path, the output electric field is given by $E = E_{SR}$. This resulting field E_{SR} corresponds to Superradiance as discussed in [92].

B.3   Evaluation of Integration

To investigate the dynamics in region 3, it is necessary to compute the integral B.7. A self-similar solution can be employed as an approximation for the nonlinear problem, as discussed in [92]. An important conclusion is the exponential growth of E_{SR} for large propagation distance:

$$E_{SR} \propto \exp(y^{3/2}), \tag{B.8}$$

where $y = \sqrt{\hat{z}_1} \hat{z}_2$ and $y > 1$.

Specifically, the growth rate of E_{SR} is independent of the detuning parameter Δ. This independence results in the emission occurring at the **spontaneous frequency**. This particular frequency aligns with the already existing FEL pulses, which will be utilised in bunching the fresh electron slices.

B.4   Discussion

In this appendix, we discuss the dynamics of superradiance, addressing the phenomenon of constant radiation frequency observed when applying a strong taper, as initially mentioned at the start of the chapter.

Upon further investigation, it becomes apparent that all the optimizations introduced in the Chapter 5 might be seen as strategies to generate superradiant spikes. This concept is rooted in the creation of a strong radiation spike, coupled with precise adjustments to the parameters for its continuous amplification during the FEL process. Consequently, the dynamics of superradiance are an inevitable outcome when these amplified FEL pulses interact with new slices of the beam.

Bibliography

[1] S. Reiche. "GENESIS 1.3: a fully 3D time-dependent FEL simulation code". In: *Nuclear Instruments and Methods in Physics Research Section A: Accelerators, Spectrometers, Detectors and Associated Equipment* 429 (1–3 1999), pp. 243–248.

[2] E. Prat, R. Abela, M. Aiba, et al. "A compact and cost-effective hard X-ray free-electron laser driven by a high-brightness and low-energy electron beam". In: *Nat. Photonics* 14 (2020), pp. 748–754.

[3] C.J. Milne et al. "SwissFEL: The Swiss X-ray Free Electron Laser". In: *Appl. Sci.* 7 (2017), p. 720.

[4] Eduard Prat et al. "An X-ray free-electron laser with a highly configurable undulator and integrated chicanes for tailored pulse properties". In: *Nature Communications* 14 (2023), p. 5069.

[5] R. Ganter. *Athos. Conceptual design report.* PSI Bericht 17-02. Villigen PSI, Switzerland: Paul Scherrer Institut, 2017, p. 98.

[6] J. Madey. "J. Appl. Phys. 42, 1906 (1971)". In: *Journal of Applied Physics* 42 (1971), p. 1906.

[7] D. A. G. Deacon et al. "Phys. Rev. Lett. 38, 892 (1977)". In: *Physical Review Letters* 38 (1977), p. 892.

[8] C. Pellegrini, A. Marinelli, and S. Reiche. "The Physics of X-ray Free-Electron Lasers". In: *Reviews of Modern Physics* 88.1 (2016), p. 015006.

[9] Z. Huang and K. Kim. *Synchrotron Radiation and Free-Electron Lasers: Principles of Coherent X-Ray Generation.* Cambridge University Press, 2017.

[10] E. L. Saldin, E. A. Schneidmiller, and M. V. Yurkov. *The Physics of Free Electron Lasers.* Berlin: Springer, 2000.

[11] H. P. Freund and Jr. Antonsen T. M. *Principles of Free Electron Lasers.* Springer, 2018.

[12] P. Schmüser et al. *Free-Electron Lasers in the Ultraviolet and X-Ray Regime: Physical Principles, Experimental Results, Technical Realization.* Cham: Springer, 2014.

[13] Brian W. J. McNeil and Neil R. Thompson. "X-ray free-electron lasers". In: *Nature Photonics* 4 (2010), pp. 814–821.

[14] R. Bonifacio, C. Pellegrini, and L. M. Narducci. "Collective instabilities and high-gain regime in a free electron laser". In: *Opt. Commun.* 50 (1984), pp. 373–378.

[15]   Shan Liu et al. "Cascaded hard X-ray self-seeded free-electron laser at megahertz repeti-
tion rate". In: *Nature Photonics* 17 (2023), pp. 984–991.

[16]   S. Schulz et al. "Femtosecond all-optical synchronization of an X-ray free-electron laser".
In: *Nature Communications* 6 (2015).

[17]   Z Huang and K Kim. "Review of x-ray free-electron laser theory". In: *Phys. Rev. ST Accel.
Beams* 10 (3 2007), p. 034801.

[18]   M. Hentschel et al. "Attosecond metrology". In: *Nature* 414 (2001), pp. 509–513.

[19]   P. B. Corkum and F. Krausz. "Attosecond science". In: *Nature Physics* 3 (2007), pp. 381–
387.

[20]   Z. Chang and P. Corkum. "Attosecond photon sources: the first decade and beyond
[invited]". In: *Journal of the Optical Society of America B* 27.B9 (2010), B9–B17.

[21]   M. F. Ciappina et al. "Attosecond physics at the nanoscale". In: *Reports on Progress in
Physics* 80 (2017), p. 054401.

[22]   Joseph Duris et al. "Tunable isolated attosecond X-ray pulses with gigawatt peak power
from a free-electron laser". In: *Nature Photonics* 14 (2020), pp. 30–36.

[23]   Joseph Duris et al. "Controllable X-Ray Pulse Trains from Enhanced Self-Amplified
Spontaneous Emission". In: *Physical Review Letters* 126 (2021), p. 104802.

[24]   R. Bonifacio, C. Maroli, and N. Piovella. "Slippage and superradiance in the high-gain
FEL: Linear theory". In: *Optics Communications* 68.5 (1988).

[25]   Eduard Prat et al. "Emittance measurements and minimization at the SwissFEL Injector
Test Facility". In: *Phys. Rev. ST Accel. Beams* 17 (2014), p. 104401.

[26]   Gerald T. Moore. "High-gain and large-diffraction regimes of the FEL". In: *Nucl. Instrum.
Methods Phys. Res. A* 250.1–2 (1986), pp. 381–388.

[27]   A He, L Yang, and L.-H. Yu. "High-Gain Free-Electron Laser Theory, Introduction". In:
Synchrotron Light Sources and Free-Electron Lasers. Cham: Springer, 2016.

[28]   Sven Reiche. *Pendulum Equations and Low Gain Regime*. Presentation at CERN Acceler-
ator School – FELs and ERLs. Paul Scherrer Institute.

[29]   J. R. Pierce. "Traveling-Wave Tubes". In: *Bell System Technical Journal* 29.4 (1950),
pp. 608–671.

[30]   E.L. Saldin, E.A. Schneidmiller, and M.V. Yurkov. "Statistical properties of radiation from
VUV and X-ray free electron laser". In: *Optics Communications* 148 (1998), pp. 383–403.

[31]   E.L. Saldin, E.A. Schneidmiller, and M.V. Yurkov. "Statistical and coherence properties
of radiation from x-ray free-electron lasers". In: *New Journal of Physics* 12 (2010).

[32]   S. Krinsky and R. L. Gluckstern. "Analysis of statistical correlations and intensity spiking
in the self-amplified spontaneous-emission free-electron laser". In: *Phys. Rev. ST Accel.
Beams* 6 (2003), p. 050701.

[33]   E.L. Saldin, E.A. Schneidmiller, and M.V. Yurkov. "Statistical properties of the radiation from SASE FEL operating in the linear regime". In: *Nucl. Instrum. Methods Phys. Res. A* 407.1–3 (1998), pp. 291–295.

[34]   Joseph W. Goodman. *Statistical Optics, 2nd Edition.* Wiley, 2015.

[35]   Sven Reiche. "Numerical studies for a single pass high gain free electron laser". 177 pages. PhD. Hamburg University, Mar. 2000.

[36]   Sven Reiche. *Genesis 1.3 Version 4.* https://github.com/svenreiche/Genesis-1.3-Version4. (Accessed: February 2024). 2023.

[37]   https://www.psi.ch/en/swissfel/accelerator. (Accessed: October 2023).

[38]   R. Ganter et al. *SwissFEL. Conceptual Design Report.* Tech. rep. Villigen PSI, Switzerland, 2010.

[39]   C. Bostedt et al. "Linac Coherent Light Source: The first five years". In: *Rev. Mod. Phys.* 88 (1 2016), p. 015007.

[40]   P. Emma et al. "First lasing and operation of an ångstrom-wavelength free-electron laser". In: *Nature Photonics* 4 (2010), pp. 641–647.

[41]   Tetsuya Ishikawa et al. "A compact X-ray free-electron laser emitting in the sub-ångström region". In: *Nature Photonics* 6 (2012), pp. 540–544.

[42]   B. Liu et al. "The SXFEL Upgrade: From Test Facility to User Facility". In: *Appl. Sci.* 12 (2022), p. 176.

[43]   E. Allaria et al. "Two-stage seeded soft-x-ray free-electron laser". In: *Nat. Photonics* 7 (2013), pp. 913–918.

[44]   W. Ackermann et al. "Operation of a free-electron laser from the extreme ultraviolet to the water window". In: *Nat. Photonics* 1 (2007), pp. 336–342.

[45]   W. Decking et al. "A MHz-repetition-rate hard X-ray free-electron laser driven by a superconducting linear accelerator". In: *Nature Photonics* 14.6 (2020), pp. 391–397.

[46]   Heung-Sik Kang et al. "Hard X-ray free-electron laser with femtosecond-scale timing jitter". In: *Nature Photonics* 11 (2017), pp. 708–713.

[47]   J. S. Fraser et al. "High-Brightness Photoemitier Injector for Electron Accelerators". In: *IEEE Transactions on Nuclear Science* 32.5 (1985), pp. 1791–1793.

[48]   J.-Y. Raguin et al. "The Swiss FEL RF gun: RF design and thermal analysis". In: *Proceedings of the 26th Linear Accelerator Conference (LINAC 2012)*. Tel Aviv, Israel, 2012, pp. 442–444.

[49]   https://www.psi.ch/en/media/our-research/swissfel-in-the-home-stretch-the-first-electrons-are-here. (Accessed: October 2023).

[50]   J.-Y. Raguin. "The Swiss FEL S-Band Accelerating Structure: RF Design". In: *Proceedings of the 26th Linear Accelerator Conference (LINAC 2012)*. Tel Aviv, Israel, 2012, pp. 498–500.

[51] M. Paraliev et al. "High stability resonant kicker development for the SwissFEL switch yard". In: *Proceedings of the 36th International Free Electron Laser Conference (FEL 2014)*. Basel, Switzerland, 2014, pp. 103–106.

[52] Martin Paraliev et al. "SwissFEL double bunch operation". In: *Physical Review Accelerators and Beams* 25 (2022), p. 120701.

[53] Luc Patthey et al. *SwissFEL ARAMIS Beamline Conceptual Design Report*. Tech. rep. 2013.

[54] T. Schmidt and S. Reiche. "Undulators for the SwissFEL". In: *Proceedings of FEL2009*. Liverpool, UK, 2009.

[55] M. Calvi et al. "Magnetic assessment and modelling of the Aramis undulator beamline". In: *Journal of Synchrotron Radiation* 25.3 (2018), pp. 686–705.

[56] Eduard Prat et al. "Demonstration of Large Bandwidth Hard X-Ray Free-Electron Laser Pulses at SwissFEL". In: *Physical Review Letters* 124 (2020), p. 074801.

[57] R. Abela et al. "The SwissFEL soft X-ray free-electron laser beamline: Athos". In: *Journal of Synchrotron Radiation* 26.4, SI (2019), pp. 1073–1084.

[58] S. Reiche et al. "OPERATION MODES OF THE SwissFEL SOFT X-RAY BEAMLINE ATHOS". In: *39th Free Electron Laser Conf. FEL2019*. Paul Scherrer Institut. Hamburg, Germany, 2019.

[59] https://www.psi.ch/en/insertion-devices. (Accessed: October 2023).

[60] S. Bettoni et al. "Overview of SwissFEL dual-photocathode laser capabilities and perspectives for exotic FEL modes". In: *High Power Laser Science and Engineering* 9 (2021), e51.

[61] E. L. Saldin, E. A. Schneidmiller, and M. V. Yurkov. "Self-amplified spontaneous emission FEL with energy-chirped electron beam and its application for generation of attosecond x-ray pulses". In: *Phys. Rev. ST Accel. Beams* 9 (2006), p. 050702.

[62] Alexander A. Zholents. "Method of an enhanced self-amplified spontaneous emission for x-ray free electron lasers". In: *Phys. Rev. ST Accel. Beams* 8 (2005), p. 040701.

[63] Gabriel Aeppli et al. "Hidden, entangled and resonating order". In: *Nature Reviews Materials* 5 (June 2020). Accessed: 2007 times. Citations: 17. Altmetric score: 10, pp. 477–479.

[64] Marco Calvi et al. "Versatile modulators for laser-based FEL seeding at SwissFEL". In: *J. Synchrotron Rad.* 30 (2023), pp. 276–283.

[65] Guanglei Wang et al. "Millijoule Femtosecond X-Ray Pulses from an Efficient Fresh-Slice Multistage Free-Electron Laser". In: *Physical Review Letters* 132 (2024), p. 035002.

[66] M. Calvi et al. "Transverse gradient in Apple-type undulators". In: *Journal of Synchrotron Radiation* 24.3 (2017), pp. 600–608.

[67] https://www.psi.ch/en/lsx/aramis-swissfel. (Accessed: October 2023).

[68] https://www.psi.ch/en/swissfel/cristallina. (Accessed: October 2023).

[69]   https://www.psi.ch/de/swissfel/furka. (Accessed: October 2023).

[70]   https://www.psi.ch/de/swissfel/maloja. (Accessed: October 2023).

[71]   Erik Hemsing et al. "Beam by design: Laser manipulation of electrons in modern accel-
       erators". In: *Rev. Mod. Phys.* 86 (2014), p. 897.

[72]   P. Sprangle, Cha-Mei Tang, and W. M. Manheimer. "Nonlinear Formulation and Effi-
       ciency Enhancement of Free-Electron Lasers". In: *Physical Review Letters* 43 (1979),
       p. 1932.

[73]   N. Kroll, P. Morton, and M. Rosenbluth. "Free-electron lasers with variable parameter
       wigglers". In: *IEEE Journal of Quantum Electronics* 17.8 (1981), pp. 1436–1468.

[74]   William M. Fawley et al. "Tapered Undulators for SASE FELs". In: *Nucl. Instrum. Methods
       Phys. Res. A* 483.1-2 (2002), pp. 537–541.

[75]   S. Krinsky and Z. Huang. "Frequency chirped self-amplified spontaneous-emission
       free-electron lasers". In: *Phys. Rev. ST Accel. Beams* 6 (2003), p. 050702.

[76]   Z. Huang and G. Stupakov. "Free electron lasers with slowly varying beam and undulator
       parameters". In: *Phys. Rev. ST Accel. Beams* 8 (2005), p. 040702.

[77]   N. R. Thompson and B. W. J. McNeil. "Mode Locking in a Free-Electron Laser Amplifier".
       In: *Physical Review Letters* 100 (2008), p. 203901.

[78]   Anthony E. Siegman. *Lasers.* University Science Books, 1986.

[79]   R. Bonifacio et al. "Spectrum, temporal structure, and fluctuations in a high-gain free-
       electron laser starting from noise". In: *Physical Review Letters* 73 (1994), p. 70.

[80]   R. Prazeres et al. "Optical klystron experiments at Orsay on Super-Aco and prospects in
       the VUV (invited)". In: *Review of Scientific Instruments* 60 (1989), pp. 1429–1434.

[81]   R. Bonifacio, R. Corsini, and P. Pierini. "Theory of the high-gain optical klystron". In:
       Physical Review A 45.5 (1992), p. 4091.

[82]   Gianluca Geloni et al. "Revision of optical klystron enhancement effects in self-amplified
       spontaneous emission free electron lasers". In: *Physical Review Accelerators and Beams*
       24.9 (2021), p. 090702.

[83]   E. A. Schneidmiller and M. V. Yurkov. "Obtaining High Degree of Circular Polarization at
       X-ray Free Electron Lasers via a Reverse Undulator Taper". In: *Phys. Rev. ST Accel. Beams*
       16 (2013), p. 110702.

[84]   E. A. Schneidmiller. "Application of a modified chirp-taper scheme for generation of
       attosecond pulses in extreme ultraviolet and soft x-ray free electron lasers". In: *Phys.
       Rev. Accel. Beams* 25 (2022), p. 010701.

[85]   T. I. Smith et al. "Reducing the sensitivity of a free-electron laser to electron energy". In:
       J. Appl. Phys. 50 (1979), pp. 4580–4583.

[86]   E. Esarey, C. B. Schroeder, and W. P. Leemans. "Physics of laser-driven plasma-based
       electron accelerators". In: *Reviews of Modern Physics* 81 (2009), p. 1229.

[87]   Zhirong Huang, Yuantao Ding, and Carl B. Schroeder. "Compact X-ray Free-Electron Laser from a Laser-Plasma Accelerator Using a Transverse-Gradient Undulator". In: *Phys. Rev. Lett.* 109 (2012), p. 204801.

[88]   Panagiotis Baxevanis et al. "3D theory of a high-gain free-electron laser based on a transverse gradient undulator". In: *Phys. Rev. ST Accel. Beams* 17 (2014), p. 020701.

[89]   Yuanshen Li, Ryan Lindberg, and Kwang-Je Kim. "Transverse gradient undulator in a storage ring x-ray free electron laser oscillator". In: *Phys. Rev. Accel. Beams* 26 (2023), p. 030702.

[90]   T. Schmidt and M. Calvi. "APPLE X Undulator for the SwissFEL Soft X-ray Beamline Athos". In: *Synchrotron Radiation News* 31.3 (2018).

[91]   E. Kur et al. "A wide bandwidth free-electron laser with mode locking using current modulation". In: *New Journal of Physics* 13 (2011).

[92]   R. Bonifacio, L. De Salvo, and P. Pierini. "Physics of the high-gain FEL and superradiance". In: *La Rivista del Nuovo Cimento* 13.4 (1990), pp. 1–80.

[93]   R. Bonifacio, B. W. J. McNeil, and P. Pierini. "Superradiance in the high-gain free-electron laser". In: *Phys. Rev. A* 40 (1989), p. 4467.

Acknowledgements

Here, I wish to extend my gratitude to everyone who supported me throughout the journey of completing my Ph.D. Although this journey was filled with challenges, it was also rich with valuable experiences and lessons learned. I would like to give special thanks to my family, whose love and support have been the pillar of my perseverance. I am also grateful to the friends and colleagues who have provided me with encouragement and inspiration. Finally, I thank all those who have been a part of this journey, whether our interactions were brief or long-lasting, as they have all contributed in some way to this chapter of my life.

Baden, 19 February 2024

L. Zhu

Short Curriculum Vitae

Longdi Zhu
Longdi.zhu@outlook.com

Education

2020-02 - 2024-01

Ph.D.: Particle Accelerator Physics
EPFL - Lausanne, Switzerland

2016-09 - 2019-09

Diplôme D'Ingénieur: Photoniques Et Systèmes Optroniques
Polytech Paris Saclay - Orsay, France

2018-09 - 2019-09

Master 2: Grand Instruments
Université Paris Saclay - Orsay, France

2013-05 - 2017-05

Bachelor of Science: Electronic Science And Technology
Xidian University - Xi'an, China

Experience

2019-04 - 2019-08

Trainee
Paul Scherrer Institute, Villigen

2018-05 - 2018-08

Research Intern
École Normale Supérieure de Paris, Paris